

Development and Characterization of Mechanically Robust, 3D-Printable

Photopolymers

by

Dalton George Sycks

Department of Mechanical Engineering and Materials Science
Duke University

Date: _____

Approved:

Kenneth Gall, Supervisor

Stefan Zauscher

Lou DeFrate

Stephen Craig

Dissertation submitted in partial
fulfillment of the requirements for the degree
of Doctor of Philosophy, in the Department of
Mechanical Engineering and Materials Science in the Graduate School of
Duke University

2017

ABSTRACT

Development and Characterization of Mechanically Robust, 3D-Printable

Photopolymers

by

Dalton George

Department of Mechanical Engineering and Materials Science
Duke University

Date: _____

Approved:

Kenneth Gall, Supervisor

Stefan Zauscher

Lou DeFrate

Stephen Craig

An abstract of a dissertation submitted in partial
fulfillment of the requirements for the degree
of Doctor of Philosophy in the Department of
Mechanical Engineering and Materials Science in the Graduate School of
Duke University

2017

Copyright by
Dalton George Sycks
2017

Abstract

3D printing has seen an explosion of interest and growth in recent years, especially within the biomedical space. Prized for its efficiency, ability to produce complex geometries, and facile material processing, additive manufacturing is rapidly being used to create medical devices ranging from orthopedic implants to tissue scaffolds. However, 3D printing is currently limited to a select few material choices, especially when one considers soft tissue replacement or augmentation. To this end, my research focuses on developing material systems that are simultaneously 1) 3D printable, 2) biocompatible, and 3) mechanically robust with properties appropriate for soft-tissue replacement or augmentation applications. Two systems were developed toward this goal: an interpenetrating network (IPN) hydrogel consisting of covalently crosslinked poly (ethylene glycol) diacrylate (PEGDA) and ionically crosslinked brown sodium alginate, and semi-crystalline thiol-ene photopolymers containing spiroacetal molecules in the polymer main-chain backbone. In addition to successfully being incorporated into existing 3D printing systems (extrusion-deposition for the PEGDA-alginate hydrogel and digital light processing for the thiol-ene polymers) both systems exhibited biocompatibility and superior thermomechanical properties such as tensile modulus, failure strain, and toughness. This work offers two fully-developed, novel

polymer platforms with outstanding performance; further, structure-property relationships are highlighted and discussed on a molecular and morphological level to provide material insights that are useful to researchers and engineers in the design of highly tuned and mechanically robust polymers.

Contents

Abstract	iv
List of Tables	x
List of Figures	xii
List of Schemes	16
Chapter 1. Introduction.....	1
1.1 Motivation	1
1.2 Overview	2
1.2.1 Chapter 2.....	2
1.2.2 Chapter 3.....	2
1.2.3 Chapter 4.....	2
1.2.4 Chapter 5.....	3
1.2.5 Chapter 6.....	3
Chapter 2. Mechanically Robust, Biocompatible Polymers Literature Review	5
2.1 Employing Structure-Property Relationships to Tune Mechanical Performance of Biocompatible Polymers.....	5
2.1.1 Design of Robust Hydrogels.....	7
2.1.1.1 Interpenetrating Polymer Network Hydrogels	7
2.1.1.2 IPN Hydrogels Incorporating Reversible Crosslinking	10
2.2 Evaluating the Mechanical Integrity of Hydrogels via Fracture Energy.....	12
2.3 Thiol-ene Click Chemistry.....	16

2.3.1. Spiroacetal Molecules	19
Chapter 3. Three-Dimensional Printing of Highly Stretchable and Tough Hydrogels into Complex, Cellularized Structures.....	21
3.1 Aims and Summary of Completed Research on Robust, PEGDA-BSA Hydrogels	21
3.2 Results of PEGDA-BSA Investigations.....	22
3.3 Conclusion and Discussion.....	36
3.4 Methods and Materials.....	40
3.4.1 PEGDA-BSA hydrogel fabrication.....	40
3.4.2 Digital Image Correlation.....	41
3.4.3 Details of Cell Culture	42
3.4.4 Encapsulated Cell Viability Testing.....	43
3.4.5 Collagen gel preparation for cell encapsulation	43
3.4.6 Cell staining for stretch testing.....	43
3.4.7 3D Printing PEG-alginate-nanoclay hydrogel.....	44
Chapter 4. Thermomechanical Properties of Spiroacetal-based Thiol-ene Polymers	45
4.1 Introduction.....	45
4.2 Materials and Methods.....	47
4.2.1 Materials	47
4.2.2 Methods	48
4.3 Results	54

4.3.1 Functional Group Conversion	54
4.3.2 Crystallinity and Thermal Transitions	57
4.3.3 Thermo-mechanical Behavior	66
4.3.4 Tensile Deformation Behavior	74
4.4 Conclusion	84
Chapter 5. A Tough, Stable Spiroacetal Thiol-ene Resin for 3D Printing	85
5.1 Introduction	85
5.2 Experimental Details	89
5.2.1 Materials	89
5.2.2 Polymer Synthesis	91
5.2.3 DSC and Photo-DSC	91
5.2.4 Rheology	92
5.2.5 Stress-Strain Behavior	93
5.2.6 3D Printing	94
5.3 Results and Discussion	94
5.3.1 Resin Stability	94
5.3.2 Kinetics of Photopolymerization	96
5.3.3 Heat Treatment	101
5.3.3.1 Thermal Behavior	101
5.3.3.2 Mechanical Behavior	106
5.3.4 3D Printing	114

5.4 Conclusions	119
Chapter 6. Conclusions	121
6.1 Future Studies and Initial Findings	122
6.1.1 Biocompatibility Assays	122
6.2 Polymer Crystallinity	126
6.4 Environmental Effects and Long Term Material Performance	130
Appendix A: Synthesis of 3,9-divinyl-2,4,8,10-tetraoxaspiro [5.5] undecane (DVTU)....	135
Appendix B: Structures and Names of Select Thiols, Alkenes, and (Meth)Acrylate Monomers	138
Appendix C: Various Tabulated Data.....	140
Appendix D: Supplemental Thermal Data for HTD7 Annealed at Various Temperatures	151
References	157
Biography	177
Publications	177
Awards.....	177

List of Tables

Table 1: Resin viscosity over time shows stability	96
Table 2: Photo-DSC parameters for various resin formulations.	100
Table 3: Thermal data from 3D printed annealed and non-annealed parts.	119
Table 4: Tensile data from 3D printed annealed and non-annealed parts.....	119
Table 5: Thiol and Alkene Conversion via ATR-FTIR.....	140
Table 6: Enthalpy of fusion, crystalline melting temperatures, and glass transition temperatures of various compositions of PDT- and HDT-TMPTMP-DVTU.....	141
Table 7: DMA and gel fraction data for HDT-TMPTMP-DVTUs.	142
Table 8: Toughness and mechanical properties as a function of crosslink density in HDT-TMPTMP-DVTUs and PDT-TMPTMP-DVTUs at 22°C.	143
Table 9: Conversion of functional groups in HDT-TMPTMP-DVTU-7.5.	144
Table 10: Glass Transition and Crystalline Melting Data for HTD7 annealed at -20 °C through three weeks.	144
Table 11: Glass Transition and Crystalline Melting Data for HTD7 annealed at 22 °C through three weeks.	145
Table 12: Glass Transition and Crystalline Melting Data for HTD7 annealed at 30 °C through three weeks.	145
Table 13: Glass Transition and Crystalline Melting Data for HTD7 annealed at 40 °C through three weeks.	146
Table 14: Glass Transition and Crystalline Melting Data for HTD7 annealed at 50 °C through three weeks.	146
Table 15: Glass Transition and Crystalline Melting Data for HTD7 annealed at 60 °C through three weeks.	147

Table 16: Room Temperature Tensile Data for HTD7 annealed at -20 °C through three weeks.	147
Table 17: Room Temperature Tensile Data for HTD7 annealed at 22 °C through three weeks.	148
Table 18: Room Temperature Tensile Data for HTD7 annealed at 30 °C through three weeks.	148
Table 19: Room Temperature Tensile Data for HTD7 annealed at 40 °C through three weeks.	149
Table 20: Room Temperature Tensile Data for HTD7 annealed at 50 °C through three weeks.	149
Table 21: Room Temperature Tensile Data for HTD7 annealed at 60 °C through three weeks.	150

List of Figures

Figure 1: Formation of an IPN Hydrogel.....	8
Figure 2: Hydrogel fracture behavior..	9
Figure 3: Illustration of Fracture Energy via Intrinsic, Dissipation from Bridge Zone, and Dissipation from Process Zone Contributions.....	15
Figure 4: Biocompatible and tough hydrogel..	23
Figure 5: Pure Shear Test Schematic to Determine Fracture Toughness..	24
Figure 6: Effect of Ca ²⁺ Concentration and PEGDA Molecular Weight on Various Mechanical Properties..	25
Figure 7: Fracture Toughness as a Function of PEGDA Concentration.	26
Figure 8: Fracture toughness of PEGDA-BSA as a Function of I-2959 Concentration.	27
Figure 9: Mechanical Properties of Optimized PEGDA-BSA Hydrogel.....	28
Figure 10: Biocompatibility of PEGDA-BSA and its capability to stretch encapsulated cells.....	31
Figure 11: PEGDA-BSA Viscosity as a Function of Shear Rate and Nanoclay Concentration.	33
Figure 12: Illustration of Collagen/PEGDA-BSA Composite Gel.....	35
Figure 13: 3D Printed Constructs of PEGDA-BSA..	36
Figure 14: Two Alginate Chains in Proximity via Ca ²⁺ ions.....	38
Figure 15: Digital Imaging Correlation Technique for Spatial Distribution of Strain.....	42
Figure 16: Select thiol and alkene monomers.....	48

Figure 17: DSC heating curves of samples with varying crosslink density immediately after photopolymerization.....	50
Figure 18: Optical characterization of semicrystalline morphology in HDT-TMPTMP-DVTUs.....	51
Figure 19: Representative IR spectrum for HDT-TMPTMP-DVTU-7.5.....	56
Figure 20: Crystallization behavior of HDT-TMPTMP-DVTUs over time.....	58
Figure 21: Polarized images of HDT-TMPTMP-DVTUs reveal characteristic Maltese cross patterns of spherulite crystals.....	60
Figure 22: DSC curves and data for various HDT-TMPTMP-DVTU compositions.....	64
Figure 23: DMA scans of HDT-TMPTMP-DVTUs.....	68
Figure 24: Tan δ curves of HDT-TMPTMP-DVTUs.....	70
Figure 25: A comparison of T _g s as a function of crosslinker density in HDT-TMPTMP-DVTUs between DSC and DMA techniques.....	73
Figure 26: Stress-strain curves for HDT-TMPTMP-DVTUs.....	76
Figure 27: Several relationships between crosslinker content and mechanical properties.....	80
Figure 28: HDT-TMPTMP-DVTU-7.5 stress-strain behavior from video- and grip strain measurement techniques.....	83
Figure 29: Ideal thiol-ene reaction proceeds only via step-growth to produce a tailored polymer backbone.....	87
Figure 30: Materials used in this investigation.....	90
Figure 31: Heat flow of resins under light from DLP positioned above DSC cell at operating distance.....	99
Figure 32: DSC heating curves at various annealing temperatures over time.....	103

Figure 33: Temperature difference between low- and high-temperature melting endotherms as a function of annealing temperature over time.	104
Figure 34: Effect of heat treatment at various temperatures on the mechanical behavior of cast dogbones made from base composition.	107
Figure 35: Yield behavior HTD7.	110
Figure 36: Mechanical behavior of HTD7 through 21 days of annealing.	113
Figure 37: Printed HTD7 parts.	116
Figure 38: Characterization of printed parts and comparison to their non-printed analogues.	117
Figure 39: 3T3 Viability.	124
Figure 40: Spherulite Presence in HDT-TMPTMP-DVTU (200X Magnification).....	126
Figure 41: DVTU Monomer X-ray Diffraction	127
Figure 42: HDT-DVTU X-ray Diffraction Spectrum.....	128
Figure 43: HDT-TMPTMP-DVTU-50 X-ray Diffraction Spectrum	129
Figure 44: HDT-TMPTMP-DVTU-10 Swelling Behavior.	132
Figure 45: Stress-Strain Behavior After PBS Immersion.....	133
Figure 46: Thiol and Alkene Monomers Screened	138
Figure 47: (Meth)Acrylate Monomers and Oligomers Screened.....	139
Figure 48: Thermal data over time during -20 °C exposure.....	151
Figure 49: Thermal data over time during 22 °C anneal.....	152
Figure 50: Thermal data over time during 30 °C anneal.....	153
Figure 51: Thermal data over time during 40 °C anneal.....	154

Figure 52: Thermal data over time during 50 °C anneal..... 155

Figure 53: Thermal data over time during 60 °C anneal..... 156

List of Schemes

Scheme 1: Mixed Kinetics of Thiol-ene polymerization.	18
Scheme 2: Synthesis of DVTU molecule, Part 1.	136
Scheme 3: Synthesis of DVTU molecule, Part 2.	137

Chapter 1. Introduction

1.1 Motivation

Impressive progress has been made in the development of biomaterials in recent years, and simultaneously the 3D printing industry has exploded from a niche market of curiosities into a fast growing industry serving nearly every market sector. The increasing sophistication and precision of the technique are opening more opportunities with every passing day; this rings especially true for biomedical applications such as patient-specific dental and hearing implants, as well as offering enormous promise for the creation of mechanically and chemically heterogeneous implants with controlled porosity at a cellular or sub-cell length scale. Yet truly robust soft biomaterials continue to present a challenge to researchers; it is telling that there are few long term, load-bearing soft material implants available at this time.^[1] Therefore, a powerful opportunity exists and the intersection of soft biomaterials, materials with high mechanical integrity, and materials that can harness the increasing power of 3D printing. This thesis aims to investigate the fundamental structure-property relations of robust materials, incorporate them into soft biocompatible materials, and examine how processing these materials via 3D printing affects their short and long term thermomechanical performance.

¹ Early efforts around silicones and polyolefins have failed repeatedly in long term load-bearing applications. Polycarbonate urethane materials have seen some use in load-bearing applications, but long term data is limited and show the materials are still subject to some degradation *in vivo*.

1.2 Overview

The remainder of the document is organized in the following manner:

1.2.1 Chapter 2

Literature review of major research pertaining to biomaterials, strengthening mechanisms employed to bolster the mechanical properties of these materials, and 3D printing applications of (bio)materials. Specific focus is applied to tough hydrogels composed of interpenetrating polymer networks (IPNs), thiol-ene polymer systems, and methods of 3D printing such as extrusion-deposition and stereolithography.

1.2.2 Chapter 3

This chapter covers my research on printed poly (ethylene glycol) diacrylate - brown sodium alginate (PEGDA-BSA) IPN hydrogels and summarizes key findings and feasibility of 3D printing constructs for tissue engineering composed of PEGDA-BSA. As a co-first author of the manuscript serving as the basis for this chapter, I was heavily involved in all aspects of this research, including experimental planning, writing, figure preparation, and editing in collaboration with my co-authors Sungmin Hong, Hon Fai Chan, Shaoting Lin, Xuanhe Zhao, and Kam Leong.

1.2.3 Chapter 4

This section marks the transition to my current research covering more promising thiol-ene materials, and especially looking to understand the thermomechanical behavior of binary and ternary thiol-ene networks and thermoplastics containing spiroacetal alkene

moieties in the polymer backbone and relating properties to the interplay of crosslinking and (semi-)crystallinity. As the first author of the manuscript serving as the basis for this chapter, I oversaw and was involved in all aspects of this research, including experimental planning, writing, figure preparation, and editing in conjunction with my co-authors Neel Reddy, Dave Safranski, Eric Sun, and Ken Gall.

1.2.4 Chapter 5

Building from the work of Chapter 4, I focus on understanding and optimizing the thermomechanical properties of the tough spiroacetal thiol-ene platform. Specifically, the effect of various heat treatment regimens is studied to optimize tensile deformation behavior, with emphasis placed on describing the structure-property relationships driving them. Finally, the resin is incorporated into a DLP 3D printing platform and its mechanical performance assessed. As the first author of the manuscript serving as the basis for this chapter, I oversaw and was involved in all aspects of this research, including experimental planning, writing, figure preparation, and editing in conjunction with my co-authors Tiffany Wu, Hyun Sang Park, and Ken Gall.

1.2.5 Chapter 6

The ultimate chapter synthesizes potential future directions by drawing upon the inspirations of the literature review as well as preliminary data from unpublished experiments such as X-ray diffraction, biocompatibility, shape memory behavior, and

long term environmental exposure testing. All data and figures presented in this chapter are solely of my own creation.

Chapter 2. Mechanically Robust, Biocompatible Polymers Literature Review

The proceeding brief literature review and discussion is focused on recent efforts to bolster the mechanical properties of various polymeric biomaterials through intelligent control of structure-property relationships. In the context of this discussion, the term polymeric biomaterial refers to any material that is composed of many repeating chemical compounds (i.e. polymers) and either has shown biocompatibility (by one or more of the widely accepted measures of biocompatibility) or has the potential to be proven biocompatible. However, due to the exhaustive nature of the phrase “polymeric biomaterial”, this literature review will restrict itself to two classes of biocompatible polymers: thiol-ene networks and hydrogels.² In light of Chapters 3-5 each containing a focused discussion on literature relevant to their specific aims, particular emphasis in this chapter is placed on derivation and interpretation of hydrogel fracture toughness to better describe the complex phenomena.

2.1 Employing Structure-Property Relationships to Tune Mechanical Performance of Biocompatible Polymers

Many living tissues display remarkable mechanical properties; that they do so while often containing over 50% water content by weight is nothing short of incredible.

² Note that a material may be both a thiol-ene and a hydrogel; however, for ease of discussion, thiol-ene will refer to bulk polymers formed by polymerization of thiol-containing monomers and unsaturated carbon-carbon containing monomers such as alkenes, (meth)acrylates, norbornenes, etc., and hydrogel shall refer to any polymer material designed to operate while swollen with water.

As researchers, one of the challenges we face is to replicate or outperform these benchmarks using synthetic materials that are more readily available and easier to process. However, nature has proven to be an excellent architect and uses a sophisticated array of tricks to reinforce her creations; examples such as the anisotropy of the epidermis and the hierarchical bundling of collagen fibers show how natural polymers make economic use of their materials to maximize mechanical benefits.^[2, 3] Contrarily, many synthetic polymeric materials are traditionally simplistic in their design, often following the motif of carbon-carbon linkages in the backbone, with optional pendant or branch molecules and/or crosslinking between chains to prevent plastic flow above the glass transition temperature. Today, materials with the most promise for impressive mechanical performance under a variety of environmental conditions imposed by physiological systems display unique synergy in their composition, architecture across several length scales (for example at the nanometer, micrometer, and centimeter scale), or both. In particular, tough polymers are often designed to incorporate interpenetrating networks, thermomechanical damping, (semi-)crystallinity, composite composition, or intermolecular forces such as hydrogen bonding or ionic bonding in solution. These mechanisms are discussed in more detail to elucidate current strategies in making robust hydrogels and bulk polymers, with a focus on using biocompatible materials.

2.1.1 Design of Robust Hydrogels

As has been alluded, hydrogels are comprised of hydrophilic polymer networks which swell upon contact with water or aqueous solutions such as saline. Because of their high water content, hydrogels present a natural choice to replace or augment damaged soft tissues due to mechanical similarity. Biological hydrogels such as tendons and muscles are simultaneously highly swollen, highly extensible, tough, and have a relatively low modulus (one example being heart muscle's modulus of approximately 10-500kPa).^[4, 5] However, synthetic hydrogels are often brittle and have low toughness³ due to the stress of swelling on the network, as well as the low density of load-bearing structures (i.e. polymer chains) relative to the total volume of the material. Much of the recent research involving hydrogels, especially concerning those designed for tissue engineering or other biomedical purposes, focuses on enhancing the mechanical properties to more closely match living tissues. Several of these strategies are discussed below.

2.1.1.1 Interpenetrating Polymer Network Hydrogels

One of the most successful methodologies for producing tough hydrogels has been the development of the interpenetrating polymer network, or IPN, hydrogel. An IPN hydrogel consists of two or more polymer networks that are entangled such that

³ A typical synthetic hydrogel will have a fracture toughness of approximately 10 Jm⁻² or less. Articular cartilage has a fracture toughness of roughly 1,000 J m⁻².^[6]

they cannot be separated unless chemical bonds are broken. This does not mandate they be covalently bonded to one another (though they may be), however; instead it is helpful to view the construct as multiple interlacing mesh networks. An example of how an IPN hydrogel may be formed is shown below. Initially, a primary gel network is formed in solution. Next, monomers of a secondary network are soaked into the gel and polymerized *in situ* to form a secondary network cohabitating with the first.

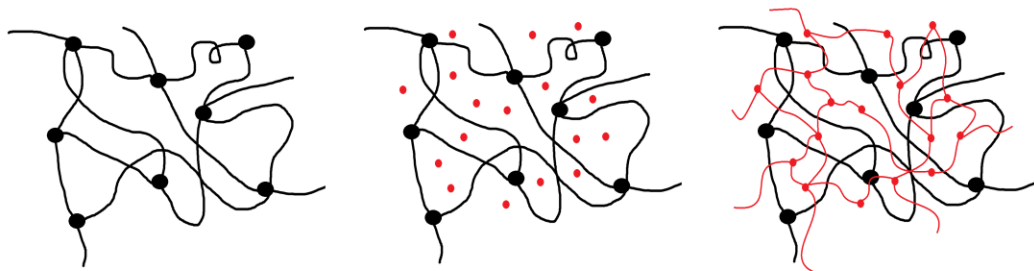


Figure 1: Formation of an IPN Hydrogel.

The most effective IPN hydrogels have been those in which one network is much more loosely crosslinked than the other, and this effect is compounded when the looser network is much more prevalent (10-50X) than the more tightly crosslinked network [7]. The reasoning for this is simple; as a crack grows and begins to propagate through the material, the more tightly crosslinked network will be fully stretched at the crack tip. These chains begin to break as the crack advances and in doing so they dissipate energy and retard further crack propagation. In their wake, the second and more loosely crosslinked network continues to bridge the void and further absorb energy as these chains extend further.^[5] The result is an enhanced “damage zone” surrounding the crack

whose thickness has a linear relation with a material's fracture toughness.^[8] An example of the damage zone and its relation with fracture toughness is shown in Figure 2.

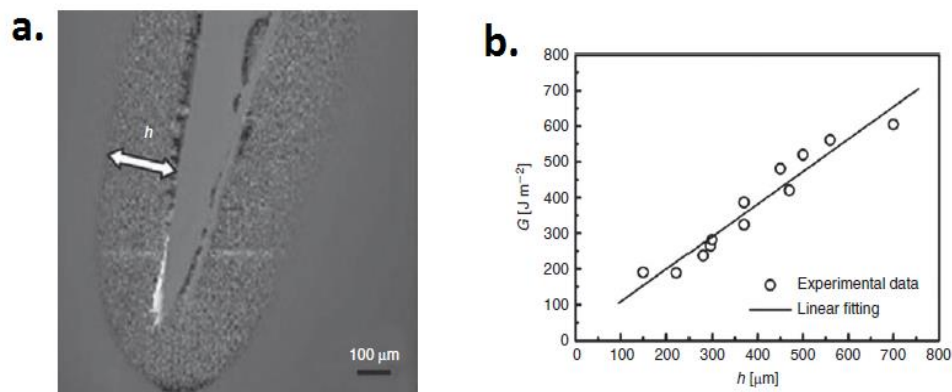


Figure 2: Hydrogel fracture behavior. A. Damage zone of an IPN hydrogel. B. Relation of thickness, h , to fracture toughness. Reprinted with permission from [8]. Copyright 2009 American Chemical Society.

IPN hydrogels subjected to multiple load-unload cycles demonstrate significant hysteresis within their first load-unload cycle but not during subsequent cycles.^[9] Furthermore, the proceeding load-unload cycles reveal a smaller modulus than the first cycle. What this says about the material is that the shorter chains of the more highly crosslinked network stretch and break at the crack tip during the first load-unload waveform, resulting in an immediate depreciation of mechanical integrity and an inability to recover from damage.

2.1.1.2 IPN Hydrogels Incorporating Reversible Crosslinking

The irreversible damage inflicted upon dual network hydrogels composed of two covalently-bonded polymer networks has led researchers in recent years to turn to systems with mixed crosslinking mechanisms.^[10] Chief among these are strategies incorporating a blend of reversible and irreversible linkages. Examples of reversible linkages are physical crosslinks, ionic-bridge crosslinks in aqueous solution, ligand-receptor crosslinks in natural polymers such as proteins, and domain transformation such as protein folding or crystalline domains. One particularly exciting strategy has been to blend a covalently crosslinked, hydrophilic polymer network (often PEGDA or polyacrylamide, PAAm) with brown sodium alginate (BSA), a polysaccharide derived from seaweed.^[11, 12] In these materials, negatively charged regions along the backbone of BSA⁴ are crosslinked across divalent cations such as Ca²⁺. Swollen with water, these IPN hydrogels are commonly also referred to as dual network (DN) hydrogels to indicate two polymer networks held together by different crosslinking mechanisms.

These systems are attractive in large part because the aqueous environment of the hydrogel dissipates applied mechanical energy through the breaking and reforming of the ionic bonds in the BSA network, while the PEGDA or PAAm network maintains the overall shape and elasticity of the network. Once the external load is removed, the covalent network acts as a restorative force and the BSA chains recruit Ca²⁺ back to

⁴ This is discussed in more detail in Chapter 3.

reform the broken linkages. It has been shown that the mechanical properties of DN hydrogels are tunable through controlling the molar ratio of the two networks as well as their respective crosslinking densities; a more larger (referring to the molecular weight of the constituent chains), more loosely crosslinked covalent network synergizes best with a shorter, more highly crosslinked ionic network to achieve the most robust hydrogels.^[8, 13, 14]

While PAAm-BSA networks have demonstrated superior mechanical properties over PEGDA-BSA, poor cell-encapsulation of the network and cytotoxicity of acrylamide monomers restrict the usage of this material for tissue engineering applications.^[15] In contrast, PEGDA hydrogels are omnipresent in cell encapsulation studies, and the photopolymerization of the PEGDA network lends itself much more readily to 3D printing than the chemically-induced polymerization of PAAm.^[12, 16, 17] Furthermore, prepolymerized PEGDA oligomers of various molecular weights ranging from 500 to 35,000 Da are readily available from commercial sources, which offer a convenient and facile avenue of control over one of the crosslink density of one of the networks.⁵ Given the state of the field, PEGDA-BSA was the DN hydrogel selected for the research described in Chapter 3.

⁵ BSA molecular weight was not controlled in the work in Chapter 3, but varies between 80 and 120 kDa.

2.2 Evaluating the Mechanical Integrity of Hydrogels via Fracture Energy

Because hydrogels often display nonlinear deformation behavior, a commonly used metric to evaluate their integrity is fracture energy, which measures the energy required to absorb a propagating defect such as a void or crack one unit area; it is measured in J/m^2 .^[10] To accurately determine fracture energy, two hydrogels of identical thickness t , width w , and height h should be created such that $w \gg h \gg t$. This is to ensure that the stress field of a propagating void is primarily located at the crack tip, and area behind the advancing crack tip is smooth gradient from fully loaded to fully relaxed. One sample shall have a notch cut of approximately $0.5w$ in length and located at $0.5h$ (halfway between tensile grips on the sample). It is then subjected to controlled tensile strain, and a critical strain parameter, s_c , is measured as the strain at which the notch begins to propagate through the material. The second, unnotched sample of identical dimensions is then subjected to the same tensile regimen as the stress-strain response is measured. The fracture energy is then calculated by:

$$E_f = h * \int_1^{s_c} \sigma ds \quad (2.2.1)$$

Here, E_f denotes fracture energy, σ is the stress measured from the unnotched sample, h is the initial gauge length (height) of the unnotched sample, and s_c is the critical strain determined from the notched sample.

Furthermore, fracture energy may be broken down into two constituent parts, intrinsic energy and mechanical dissipation energy. Therefore

$$12 \quad (2.2.2)$$

$$E_f = E_I + E_D$$

with fracture energy, E_f , is equal to intrinsic energy, E_I , plus dissipation energy, E_D .

Intrinsic energy is derived from the Lake-Thomas rubber theory,^[18] and is a measure of the energy required to break polymer chains lying in the plane of the propagating crack.

Thus

$$E_I = E_p * n \quad (2.2.3)$$

in which intrinsic energy, E_I , is equal to the energy required to break a single polymer chain, E_p , multiplied by the number of chains in the crack plane, n . Common elastomers described by this equation have an intrinsic energy of roughly 50Jm^{-2} , and for a hydrogel of approximately 80% water, this would equate to 10Jm^{-2} .

The second portion of fracture energy, mechanical dissipation energy, is concisely explained by Zhao,^[10] whose work is summarized briefly here. Several less relevant, finer points of toughening such as domain transformations are outside the scope of this review and thus left for the reader to pursue at his or her desire. While most hydrogels get their mechanical dissipation from deformation and relaxation in the process zone, the shell of material running along the side of a propagating crack, fiber reinforced or filled hydrogels also benefit from contribution of dissipation at the bridging zone (tip of the crack) as these reinforcing agents are disrupted from their matrix. In the bridge zone, dissipation energy can be understood as:

$$E_{D_B} = 2 * A * \int_0^{u^*} T du \quad (2.2.4)$$

Here, $2u$ represents the crack opening, $2u^*$ is the opening at the edge of the bridging zone (shown in the figure below), T is normal stress on the fibers or reinforcing fillers, and A is the area fraction of the filling agents.

The process zone also contributes a substantial portion of the mechanical dissipation energy. This contribution takes the form

$$E_{D_P} = 2V * \int_0^h w_D dy \quad (2.2.5)$$

where E_{D_P} , the dissipation energy of the process zone, is a function of V , the volume fraction of the hydrogel in the process zone, the width of the process zone in the reference (undeformed) state, w_D is the volume-normalized dissipation energy, and y is the vertical coordinate of the hydrogel element. Furthermore, w_D is calculated as the summation of the path integrals around the hysteresis loop in all three principle directions. That is to say

$$w_D = \sum_{i=1}^3 \oint s_i d\lambda_i \quad (2.2.6)$$

s_i represents the principle stress and λ_i is the strain in the three principle directions. The above two equations rely on knowledge of all hydrogel elements, and thus are often solved using numerical methods such as finite element methods or phase field analysis.^[19-22] Putting it all together gives the complete expression for fracture energy of a hydrogel which incorporates intrinsic energy, dissipation energy at the bridge site, and dissipation energy in the process zone:

$$E_f = E_l + E_{D_B} + E_{D_P} = \quad (2.2.7)$$

$$(E_p * n) + \left(2 * A * \int_0^{u^*} T du \right) + \left[2V * \int_0^h \left(\sum_{i=1}^3 \oint s_i d\lambda_i \right) dy \right]$$

The above equation is more easily visualized in the figure below.

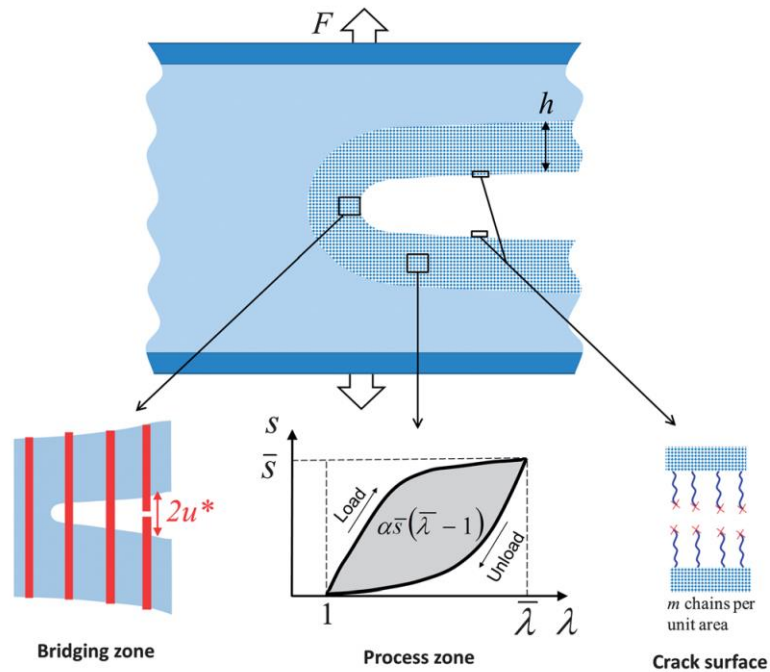


Figure 3: Illustration of Fracture Energy via Intrinsic, Dissipation from Bridge Zone, and Dissipation from Process Zone Contributions. Reproduced with permission from [10]. Copyright 2013 Royal Society of Chemistry.

Here it is easy to see the individual contributions of both polymer chains and macroscopic fibers in the bridging zone, the loading and unloading hysteretic dissipation of the hydrogel in the process zone, and any potential surface interactions of the dangling or broken chains at the crack surface. Note that the hysteresis loop may be present at only the first load-unload cycle (indicating a fatigue-prone material), or it may display recovery behavior between successive load-unloading cycles, as is the case with

fatigue-resistant materials that incorporate recoverable bonding into their structure as detailed in Section 2.1.1.2.

2.3 Thiol-ene Click Chemistry

Thiol-ene reactions are not a new discovery; on the contrary, first understood over 100 years ago with investigations of the reactions occurring as early as the 1930's.^[23] Under the definition given by Sharpless in 2001, the polymerization of thiols with alkenes may be characterized as a “click” reaction.^[24] Briefly, a click reaction is one which displays the following characteristics:

- Facile reaction conditions (mild or no solvents involved)
- Quantitative or near quantitative yields
- Few byproducts (if any) which are easily removable and inoffensive
- Robust reaction that can be carried out in atmospheric conditions (e.g. in the presence of moisture and oxygen)

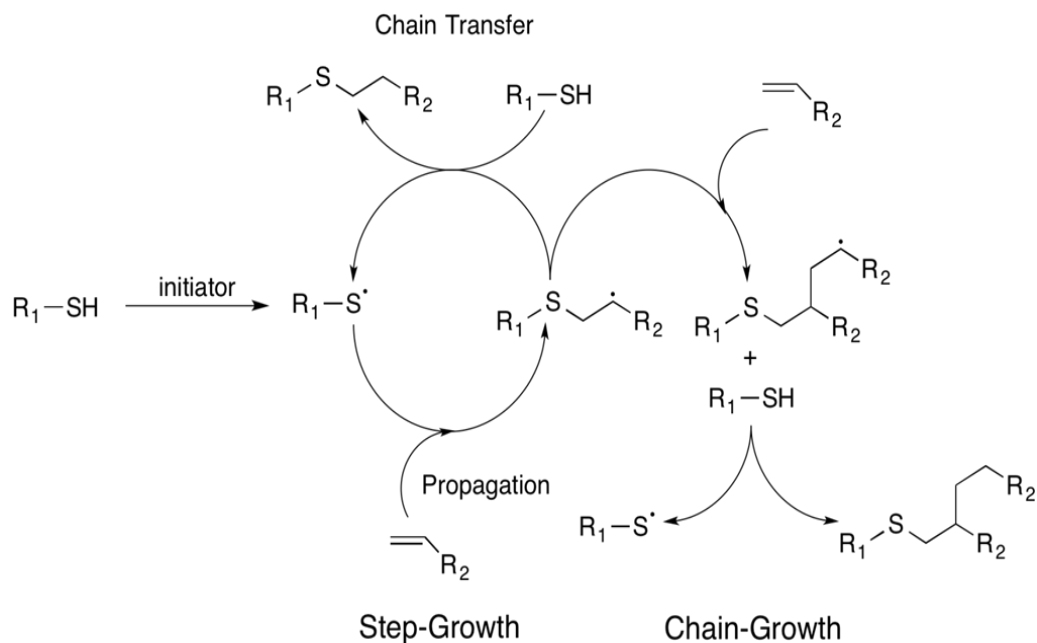
Due to the above characteristics, as well as a delayed gelation point (resulting in heterogeneous network), thiol-ene polymerizations result in materials with extremely sharp glass transition temperature windows, usually on the order of 30-50°C as compared to several hundred degrees of range in heterogeneous networks such as (meth)acrylate homopolymerization.^[25] The gel point may be calculated by the following equation:^[26]

$$\alpha = [1/r(f_t - 1)(f_e - 1)]^{0.5} \quad (2.3.1)$$

Here, the gel point, α , is determined by the thiol:ene functional group molar ratio r , as well as the functionality of the thiol and ene species, f_t and f_e , respectively. If several thiol and -ene species are used then their functionality is a weighted average of each component's individual functionality. The sharp transition resulting from a late gel point is widely used for intelligent material design for applications such as shape memory polymers,^[27, 28] mechanically superior materials,^[29] and flexible electronic applications such as softening intracortical electrodes.^[30-32]

Thiol-ene reactions can broadly be divided into two reaction mechanisms: radical-mediated photopolymerization and nucleophilic, Michael addition activated enes.^[33] Because this thesis focuses on photopolymerizable polymers and their processing via photo-3D printing methods, it is left to the reader to pursue base-catalyzed reactions at their leisure. The reaction scheme of thiol-ene photopolymerization is outlined below. To begin, a photoinitiator is exposed to light to generate a radical pair. This radical abstracts the thiol hydrogen to form a thiyl radical. Thiyl radicals do not further react with thiol functional groups, and therefore break the unsaturated C=C bond of the alkene species. It is here that the reaction may split down one of two paths: if the ene is self-reactive (as is the case for acrylates and methacrylates), it may undergo a chain-growth process wherein the ene radical attacks a C=C bond, or it can participate in the step-growth chain transfer process by circling back

to abstract a thiol hydrogen. Termination of the reaction occurs via two radical coupling (in lieu of disproportionation).



Scheme 1: Mixed Kinetics of Thiol-ene polymerization.

Radical-mediated photopolymerization of thiol-enes is a fairly fast and efficient process, with the majority of functional groups converting (engaging in the polymerization process) within seconds to minutes of reaction initiation.^[34] The kinetics of the reaction are dependent on the chemical structure of both the ene and thiol species, of which the ene hierarchy of reactivity is better understood. In particular, norbornenes > vinyl ethers > propenyl > alkenes ~vinyl ester in terms of reaction speed.^[34] As a general rule, functional groups that are more sterically available (terminal vinyl bonds or sulfurous hydrogens) react faster and more efficiently. Today, radical thiol-ene reactions are being used for a wide variety of applications such as lithography, high

impact coatings, optical applications, surface modification of nanoparticles, drug delivery, and 3D printing.^[35]

2.3.1. Spiroacetal Molecules

One subset of enes that has been understudied is spiroacetal molecules, which are a subset of spiro molecules. A spiro molecule is one in which two neighboring, strained rings are joined via a shared atom such as a tetrahedral carbon. Similar to thiol-ene reactions, spiro molecules have had an on-and-off history of investigation dating back to the early 1910s.^[36-38] Spiroacetals are spiro molecules with acetal linkages in their rings, and have been understood to exhibit crystallinity and act as fiber forming molecules.^[39] Furthermore, spiroacetal polymers demonstrate high transparency (when non-crystalline), heat and water resistance, have the potential to be synthesized via renewable pathways, and have impressive mechanical properties.^[40, 41] The high rigidity exhibited from spiroacetals led researchers as early as 1960s and 1970s to suggest flexible thioether linkages as a perfect complement to spiroacetal units to enhance their notoriously poor processability and increase their mechanical integrity.^[38, 39, 42] More recent studies have focused on using spiroacetals such as 3,9-divinyl-2,4,8,10-tetraoxaspiro[5.5]undecane (DVTU) for drug delivery applications.^[43-46] Despite the tremendous promise for a multitude of applications offered by spiroacetal polymers, there are few groups focusing on these materials, and fewer still are investigating the thermomechanical properties of polymers with spiroacetal units. It is for this reason that

the work of Chapters 4 and 5 use 3,9-divinyl-2,4,8,10-tetraoxaspiro[5.5]undecane exclusively as the -ene of interest.

Chapter 3. Three-Dimensional Printing of Highly Stretchable and Tough Hydrogels into Complex, Cellularized Structures

3.1 Aims and Summary of Completed Research on Robust, PEGDA-BSA Hydrogels

While tough hydrogels are being intensively developed as robust scaffolds in biological research and biomedical engineering,^[7, 15, 47-49] the application of these hydrogels is often severely limited by their incapability to encapsulate viable cells or form functional three-dimensional (3D) structures. Here, a new alginate-poly (ethylene glycol) hydrogel with designed, bimodal chain-length distributions and hybrid crosslinking that can achieve high stretchability (>500%), toughness (>1500 Jm⁻²), and encapsulation of human mesenchymal stem cells (hMSCs) with high viability (>80%) is described. Using biocompatible nanoclays to tune the viscosity of pre-gel solutions, the ability to print the tough and stretchable hydrogel into a wide variety of complex structures that can act as a structural scaffold to host cells is demonstrated. Owing to its simple one-step synthesis and facile 3D printing, it is expected that the new hydrogel will find broad and important applications; for example, to develop cellularized constructs that can withstand high stretching, or to mechanically stimulate hMSCs at high strains in 3D hydrogel scaffolds *in vitro* or *in vivo* for controlled differentiation or tissue regeneration.

Living tissues usually have high fracture toughness in order to withstand substantial internal and external mechanical loads.^[50] This challenges researchers to

design hydrogels capable of achieving similar toughness in order to withstand physiological mechanical loads.^[51] Despite recent success in developing tough hydrogels,^[10, 11, 15, 47, 52-57] the fabrication of these hydrogels often involves toxic chemicals and/or harsh reactions, limiting their capability to encapsulate cells. In addition, it is desirable to fabricate cell-embedded hydrogels with macroporous architecture conducive to generation of complex tissues. While 3D printing offers rapid prototyping^[16, 58-61] and can print hydrogels into complex 3D structures for functions such as vascular networks^[59, 60, 62] and aortic valves,^[63, 64] it has not been able to print tough hydrogels with complex geometry other than simple and flat structures such as dog-bone samples due to the difficulty of controlling pre-gel solutions' viscosity.^[16]

3.2 Results of PEGDA-BSA Investigations

Here, we chose the biocompatible materials brown sodium alginate and poly (ethylene glycol) diacrylate (PEGDA) to constitute an interpenetrating network as shown below in Figure 4. PEGDA and alginate polymers are covalently and ionically crosslinked through UV exposure and Ca^{2+} , respectively. As the hydrogel is deformed, the alginate chains are detached from the reversible ionic crosslinks and mechanical energy is dissipated. Once the hydrogel is relaxed from deformation, it regains its original configuration since the covalently crosslinked PEG network maintains the elasticity of the hydrogel. Over time, the ionic crosslinks in the alginate network can reform in the deformed and relaxed hydrogel.

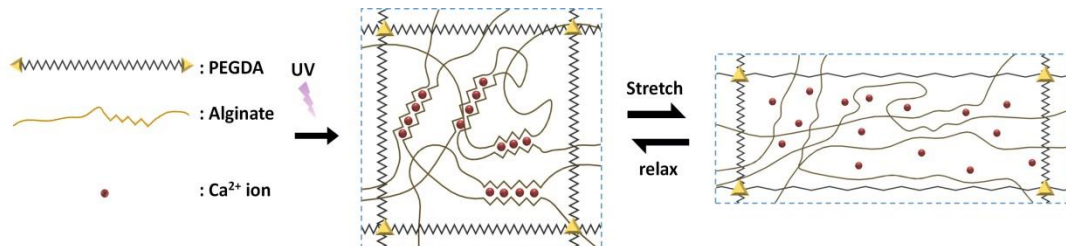


Figure 4: Biocompatible and tough hydrogel, which can reversibly stretch and relax while maintaining toughness.

The resultant hydrogel of covalently crosslinked PEGDA and ionically crosslinked alginate possesses high fracture toughness and allows cell encapsulation (Figure 9 and Figure 10). Detailed formulation of the hydrogel is described in the Methods and Materials Section. We hypothesized that the toughening of this biocompatible hydrogel relies on a combination of two mechanisms: the reversible Ca²⁺ crosslinking of alginate dissipates mechanical energy, while the covalently crosslinking of PEGDA maintains elasticity under large deformations (Figure 4). To test this hypothesis, we varied the molecular weight of PEG (6,000 Da to 20,000 Da) and the concentrations of Ca²⁺ (25 μ l of either 0M or 1M CaSO₄ solution added per 1 mL of the pre-gel PEG-alginate mixture) in the hydrogels, and used pure-shear tests to measure the fracture energies of the resultant hydrogels.^[18] The pure-shear test is shown below in Figure 5. As illustrated, we separately stretched two identical samples with the same thickness T_0 , width W_0 , and initial gauge length L_0 , where $W_0 \gg L_0 \gg T_0$. One sample was notched with a crack with length of $\sim 0.5W_0$ and the other was un-notched. The notched sample was stretched to a critical distance L_c (length at which crack

propagation began), while the un-notched sample was stretched to measure the force-

displacement curve. The fracture energy of the gel can be calculated by $\Gamma = \frac{\int_{L_0}^{L_c} F dl}{W_0 T_0}$.

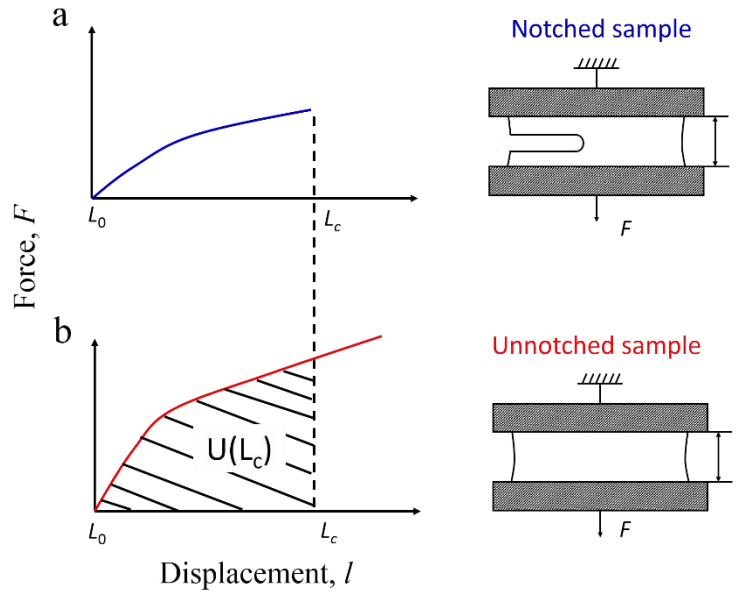


Figure 5: Pure Shear Test Schematic to Determine Fracture Toughness. A. Tensile deformation of a notched sample gives critical strain, L_c . B. Area under curve of tensile graph of an unnotched hydrogel through L_c gives fracture toughness.

As shown in Figure 6a, the fracture energies of hydrogels without Ca^{2+} are consistently low (below 211 Jm^{-2}) and they display negligible stress-strain hysteresis (Figure 6b). Introducing reversible Ca^{2+} crosslinking into the hydrogels significantly increases their fracture energies. It is also evident that increasing the molecular weight of the PEGDA (that is, the length of polymer between acrylate crosslink sites), leads to increasing ultimate tensile strain and fracture toughness. The increase in fracture energy is also accompanied by significant increase in stress-strain hysteresis, which indicates

mechanical dissipation in the hydrogels under deformation (Figure 6b). In addition, the fracture energy of calcium-containing hydrogels increases drastically with the molecular weight of PEG, because the longer polymer chains of PEG allow for higher stretchability of the hydrogel (Figure 6b and c). These results validate the hypothesis that the combined mechanisms of mechanical energy dissipation and high elasticity are critical to the toughening of the PEG-alginate hydrogels. To further test the hypothesis, we made a set of pure PEG hydrogels with different molecular weights and concentrations of PEG and measured their fracture energies. From Figure 6b and c, it is evident that the fracture energies of pure PEGDA hydrogels are significantly lower than the corresponding PEGDA-BSA hydrogels with Ca^{2+} , further validating the proposed toughening mechanism.

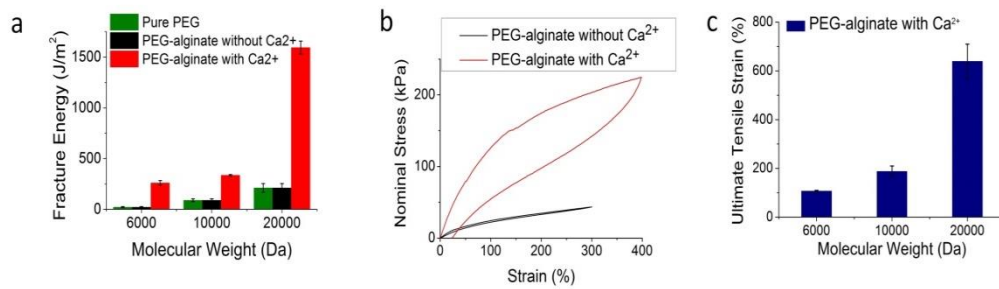


Figure 6: Effect of Ca^{2+} Concentration and PEGDA Molecular Weight on Various Mechanical Properties. A. Fracture Energy. B. Hysteresis. C. Ultimate Tensile Strength.

By further optimizing the concentrations of polymers and photo initiators (Figure 7 and Figure 8), the resultant hydrogel, with 20 wt % PEG and 2.5 wt % alginate, can reach a maximum fracture energy of $\sim 1,500 \text{ Jm}^{-2}$, which is higher than the value of

human articular cartilage.^{16]} First, the effect of PEG concentration on fracture energy of the hydrogel was investigated. Various concentrations of PEG-diacrylate (molecular weight 20,000Da) were mixed with a fixed concentration of alginate (2.5 wt%) in the pre-gel solutions. As shown in Figure 7, higher concentrations of PEG increase the fracture energy of the hydrogel. We chose 20 wt% PEG for the pre-gel solutions of PEG-alginate hydrogels in the current study, since the corresponding hydrogel readily exhibits fracture energy values surpassing 1,000 Jm⁻². As a control study, we also measured the fracture energy of hydrogels made from PEG-diacrylate (molecular weight 20,000Da) without alginate.

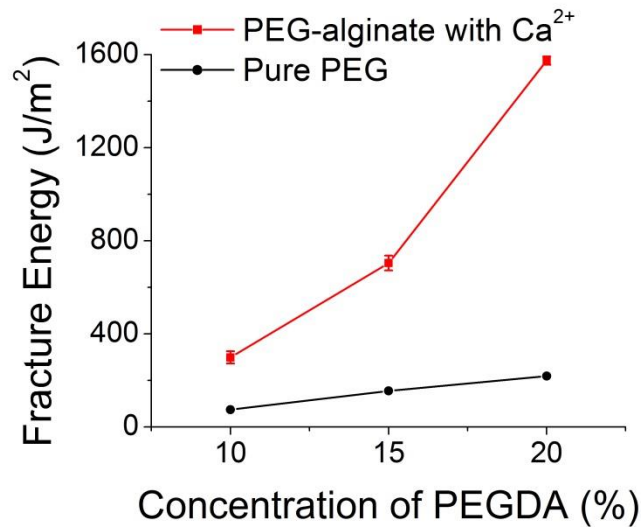


Figure 7: Fracture Toughness as a Function of PEGDA Concentration.

Higher concentrations of PEGDA above 25 wt% proved fruitless as the viscosity of the gel began to prevent homogenous mixing of polymer powder and water during synthesis, and therefore 20 wt% was chosen as the optimum balance between facile

processing and properties. This was then chosen as the baseline material composition used to optimize photoinitiator concentration, Irgacure 2959 (I-2959). As shown below in Figure 8, a concentration of I-2959 of .0007 wt/vol%¹ was found to produce the material with the highest fracture toughness.

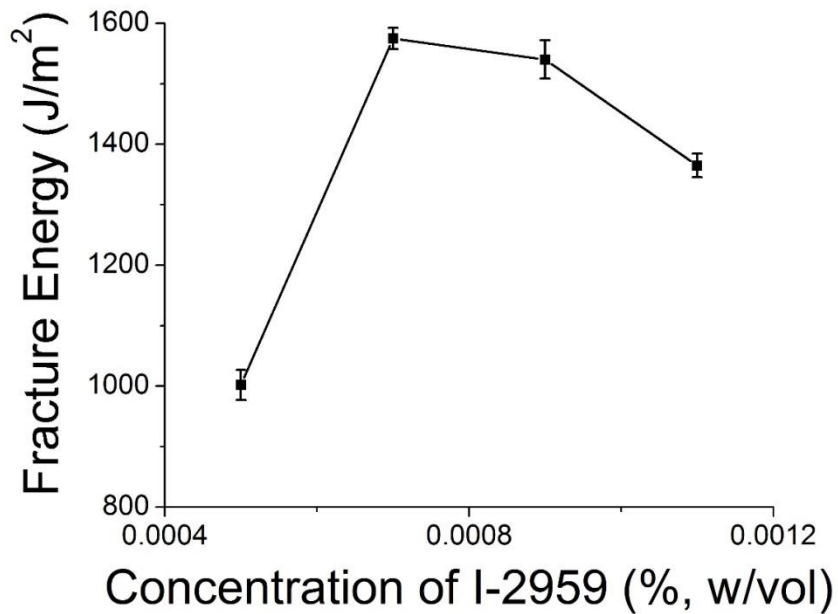


Figure 8: Fracture toughness of PEGDA-BSA as a Function of I-2959 Concentration.

Furthermore, we used a digital image correlation technique^[65] to measure the stress field around the tip of a crack in the hydrogel under pure shear tests. As shown in Figure 9, the crack in the hydrogel becomes highly blunted and the principal stress/strain at the crack tip before crack propagation reaches approximately the

¹ Irgacure 2959 is found to be biologically safe at concentrations of approximately 0.5wt/vol% or less.

ultimate tensile strength/strain of the same, unnotched hydrogel under pure-shear tension. This indicates that the alginate-PEG hydrogel is indeed a tough, soft material.^[65]

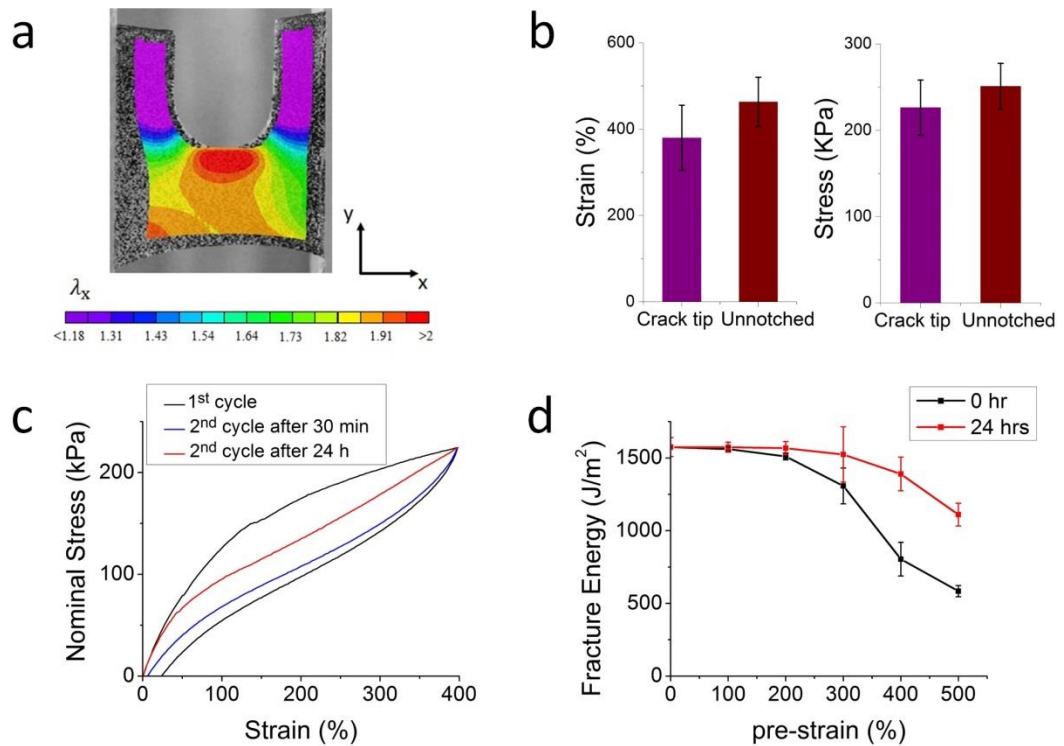


Figure 9: Mechanical Properties of Optimized PEGDA-BSA Hydrogel. A. Image correlation illustrates crack tip blunting. B. Failure stress and strain of comparison of notched and unnotched gels. C. Recovery effect on stress-strain through 400% stretching. D. Recovery effect on fracture energy.

In addition, since the mechanical energy dissipation in the PEGDA-BSA hydrogel relies on reversible crosslinking, the dissipative property of the hydrogel is partially recoverable after deformation.^[15] We illustrated this point by stretching a hydrogel sample with the optimized composition to a strain of 400%, followed by relaxation of the sample. The relaxed sample was then kept in a humid chamber at 37 °C, and we repeated the stretch-relax tests after 30 minutes and 24 hours of storage.

Figure 9c shows that after storage at 37 °C for 24 hours, the deformed hydrogel can achieve 58.9% of the hysteresis in the first loading-unloading cycle, indicating partial recovery of the dissipative properties due to reversible crosslinking of Ca²⁺.

The recovery of ionic crosslinking responsible for energy dissipation contributes to the maintenance of relatively high fracture energy of the hydrogel after deformation.^[7, 15] To demonstrate this, we stretched a set of hydrogels to different strains, ranging from 0% to 500%, under uniaxial tension. The fracture energies of the pre-deformed hydrogels were measured either right after the pre-strain or after storage in a humid chamber at 37 °C for 24 h. The measured fracture energies of hydrogels under different pre-strains are given in Figure 9d. It can be seen that pre-strained hydrogels have drastically reduced fracture energies if tested immediately after deformation, since the dissipative ionic crosslinks do not have enough time to reform. On the other hand, if pre-strained hydrogels are stored at 37 °C for 24 hours, they can recover most of their high fracture energy. For example, a hydrogel subjected to a large strain of 500% and then stored at 37 °C for 24 hours recovered 70.5% of the fracture energy of the undeformed gel. Such retention of fracture toughness after deformation is critical to the design of anti-fatigue hydrogels.^[10, 47]

Both PEG and alginate are widely known to be biocompatible and have been extensively used in biomedical applications.^[66, 67] We hypothesized that the tough PEG-alginate hydrogel can be used to encapsulate cells while maintaining high viability of

the encapsulated cells for biomedical applications. To test this hypothesis, human mesenchymal stem cells (hMSCs) encapsulated in the hydrogels were monitored for viability. Before encapsulation, 2 mL of PEG-alginate mixture was prepared, and the hMSC suspension was centrifuged at 1000 rpm for 5 minutes. The cell pellet was re-suspended with 70 μ L of I-2959 (1%, w/vol in H₂O) and mixed with PEGDA-alginate solution to seed a final cell density of 3×10^6 cells/mL. Then, 50 μ L of CaSO₄·2H₂O slurry was thoroughly mixed into the hydrogel, which was then transferred to a glass mold and exposed to 365 nm UV light for 10 minutes to crosslink the solution into PEG-alginate hydrogel. The hydrogel was immersed in α -minimum essential medium with 20% fetal bovine serum and 1% penicillin/streptomycin. Live/dead assays were used to determine cell viability in the hydrogel over the course of 7 days. From Figure 10a, it can be seen that high cell viability, ranging from $86.0 \pm 3.8\%$ to $75.5 \pm 11.6\%$, was maintained over seven days of culture. The result indicates that the current synthesis of the PEG-alginate hydrogel is a benign, cell-friendly process and the resultant hydrogel allows for nutrient diffusion and waste transport to support viable cell culture over extended periods of time.

Because the PEG-alginate hydrogel is highly stretchable and tough, the hMSCs encapsulated in this 3D extracellular matrix can be highly deformed by stretching the hydrogel. To illustrate this point, the hydrogel with encapsulated hMSCs was stretched to various strains from 0% to 300%, and then fixed on a clean glass slide. The stretched

gels were imaged under a Zeiss LSM 510 inverted confocal laser microscope. As shown in Figure 10b, both the actin-filament network and nuclei are highly deformed together with the gel. Consequently, the ratio between two axes of cell bodies and nuclei drastically increased with applied strains, as shown in Figure 10c.

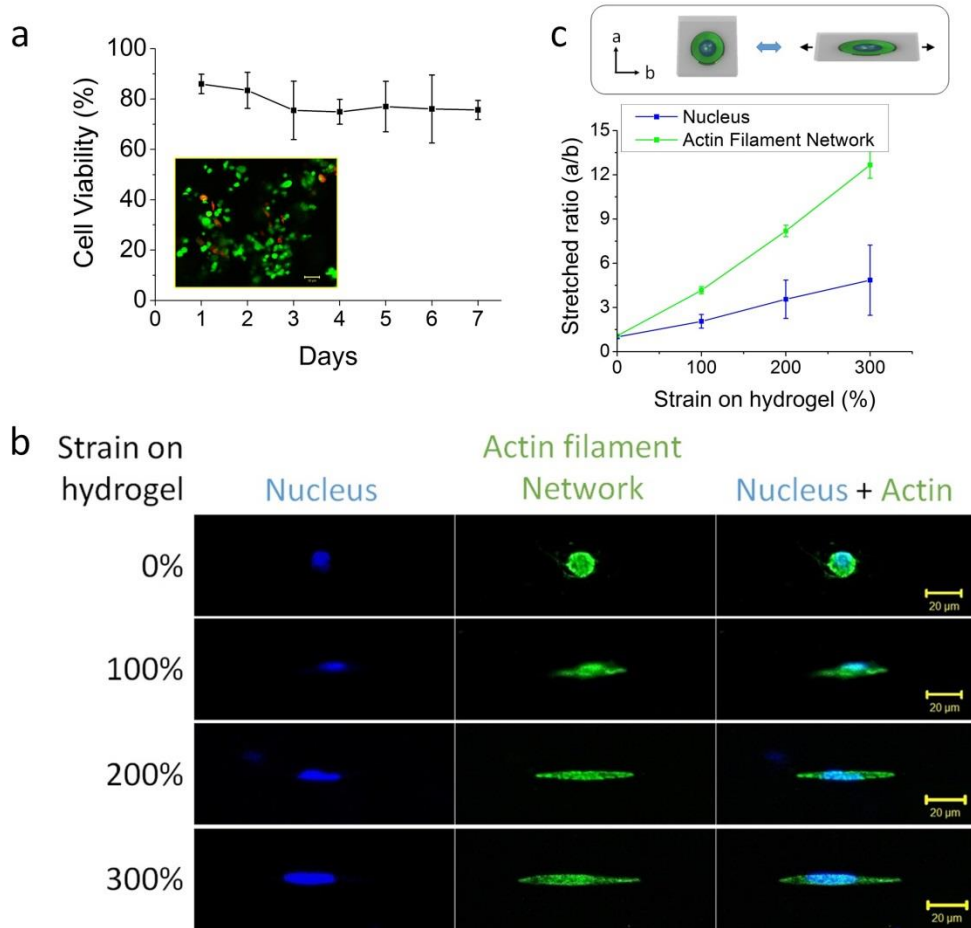


Figure 10: Biocompatibility of PEGDA-BSA and its capability to stretch encapsulated cells. A. Cell viability through one week. B. Stained cells stretch in parallel to hydrogel deformation. C. Nucleus versus actin stretching inside cells.

Next, we demonstrate the capability of printing the PEG-alginate hydrogels into various complicated 3D structures that can also be cellularized. Controlling the viscosity

of the pre-gel solution is critical to the success of printing 3D structures of hydrogels.^[16, 59, 68] It is usually desirable for the pre-gel solution to have relatively low viscosity at high shear rate but much higher viscosity at low shear rate, so that the pre-gel solution can easily flow out of the printer but maintain its shape once printed.^[63, 64, 69] Here, we chose to use bio-compatible nanoclay (Laponite XLG, BYK Additives, Inc., TX) to control the viscosity of the pre-gel solution by incorporating it into the PEG/alginate hydrogel.^[70] The nanoclay particles physically crosslink both with themselves, as well as with the polymer networks of the PEG and alginate to increase the viscosity of the pre-gel solution.^[71, 72] A cone and plate rheometer (TA Instruments, New Castle, DE) was used to confirm the increase in viscosity of the pre-gel solution as a function of nanoclay content, while maintaining its ability to shear thin and flow under the high shear rates present in the extrusion needle (Figure 11).

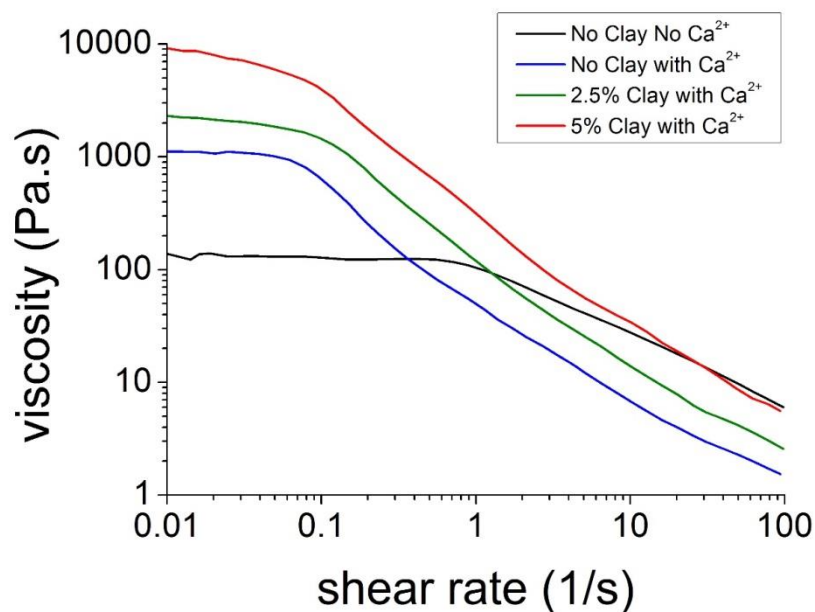


Figure 11: PEGDA-BSA Viscosity as a Function of Shear Rate and Nanoclay Concentration.

Because nanoclay significantly enhances the viscosity of the pre-gel solution and also increases its shear-thinning properties, we chose the PEG-alginate-nanoclay system as the ink of our 3D printer (Fab@Home Model 3, Seraph Robotics, Inc., NY). The printing process is described in the Methods section. In Figure 13, we show that the PEG-alginate-nanoclay hydrogels can be printed into diverse shapes such as a hollow cube, hemi-sphere, pyramid, twisted bundle and physiologically-relevant shapes such as human nose and ear models. Printed objects may also be composed of multiple materials, which is illustrated in the two-color mesh in Figure 13b. The mesh consists of alternating layers of PEG-alginate-nanoclay that either contains red or green food dye to demonstrate this concept. The spatial resolution of the printed objects depends on

factors such as precision of the printer, the pre-gel viscosity and extrusion needle diameter, and is approximately 500 μm with the current printer. This resolution is consistent with previous reports on hydrogel structures printed with the same type of printer (i.e., Fab@Home).^[63, 64] Tough hydrogel structures of higher resolution may be achieved by using the PEG-alginate-nanoclay system with a 3D printer of higher precision.

To investigate the biocompatibility of the printed tough hydrogel with incorporated nanoclay, human embryonic kidney (HEK) cells were encapsulated into a type 1 rat tail collagen solution (Corning Inc., Corning, NY), which then gelled throughout the interconnected pores of the printed PEG-alginate-nanoclay mesh to form a composite hydrogel as shown in Figure 12: Illustration of Collagen/PEGDA-BSA Composite Gel. Cell-containing collagen is shown in gold, while the PEGDA-BSA scaffold is tan.. The encapsulated HEK cells were seeded at a concentration of 3×10^6 cells/mL of collagen gel, and maintained high viability (~95%) over the course of 7 days of culture (Figure 13c and d).

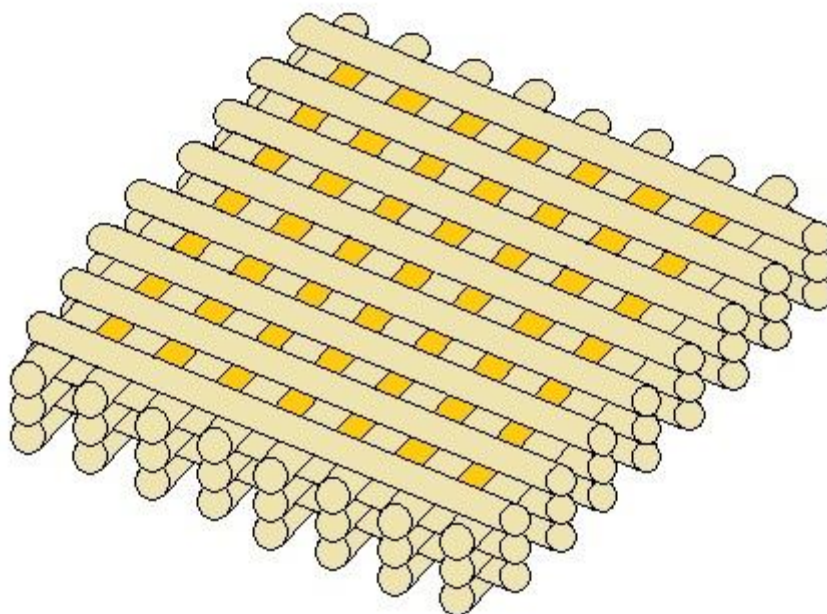


Figure 12: Illustration of Collagen/PEGDA-BSA Composite Gel. Cell-containing collagen is shown in gold, while the PEGDA-BSA scaffold is tan.

The printed hydrogel structures are also highly deformable and tough, demonstrating that the added nanoclay does not significantly affect the superior mechanical qualities of the hydrogel. As shown in Figure 13e, a printed mesh of the hydrogel was uniaxially stretched to 300% of its undeformed length, held for one minute, and allowed to relax to its initial state. The mesh experienced very little permanent deformation, since the long-chain PEG network maintains the high elasticity of the hydrogel. Figure 13f show a printed pyramid that undergoes 99% compressive strain and regains 97% of its original height within 5 minutes of unloading.

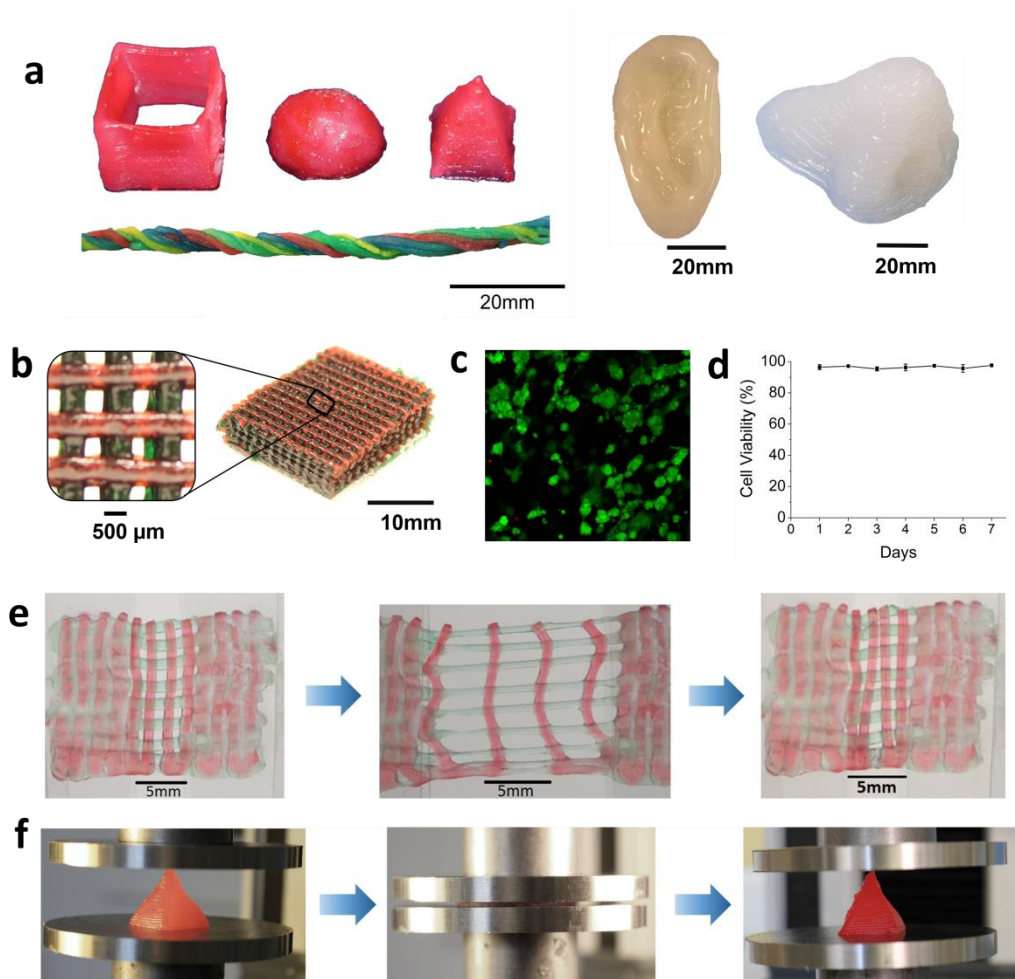


Figure 13: 3D Printed Constructs of PEGDA-BSA. A. Printed geometries, ear and nose models (simplified). B. Printed multi-layer mesh. C. Cell staining indicates high viability. D. Quantified viability through one week. E. Printed meshes sustain 300% strain. F. Printed constructs withstand up to 99% compressive strain with minimal permanent deformation.

3.3 Conclusion and Discussion

In conclusion, we have created a tough hydrogel comprised of PEG and sodium alginate that can be used for cell encapsulation. The hydrogel can endure high stress in both tension and compression and has a fracture toughness above $1,500 \text{ Jm}^{-2}$, making it tougher than natural cartilage and yet with water content ($\sim 77.5 \text{ wt } \%$) that is tunable

and within the physiologically acceptable range. The reversible crosslinking of the alginate dissipates mechanical energy under deformation and the long-chain PEG network maintains high elasticity of the hydrogel; these phenomena combine to result in a robust, tough hydrogel. Encapsulated cells showed high viability over 7 days, averaging $75.5 \pm 11.6\%$ in the PEG-alginate hydrogel and 95% in infiltrated collagen between the pores of a printed PEG-alginate-nanoclay mesh. In addition, we were able to print the tough hydrogel into complicated 3D structures by using nanoclay to control the pre-gel solution's viscosity. To our knowledge, this study is the first to demonstrate a hydrogel that is not only tough and 3D-printable, but suitable for long-term cell culture as well.

Despite the successes of these investigations, several critical shortcomings were discovered throughout the investigation, which ultimately led to a pivot in the focus of this dissertation to the thiol-ene system highlighted in the following chapters. In particular, maintaining the strength of the ionic crosslinks between alginate chains, oxygen inhibition of the photoinitiated covalent crosslinking of PEGDA, and an inherent tradeoff between cell viability and high toughness emerged as fundamental roadblocks to the progress of this technology out of the laboratory and into widespread usage. To understand how the ionic crosslinks lose their strength, it is important to consider the structure of alginate polysaccharides. As shown below, alginate is composed of (1,4)-linked β -D-mannuronate (M) and α -L-guluronate (G) residues.^[73] In solution, the

negatively-charged G blocks are pulled in proximity to one another via the divalent positive Ca^{2+} ions.

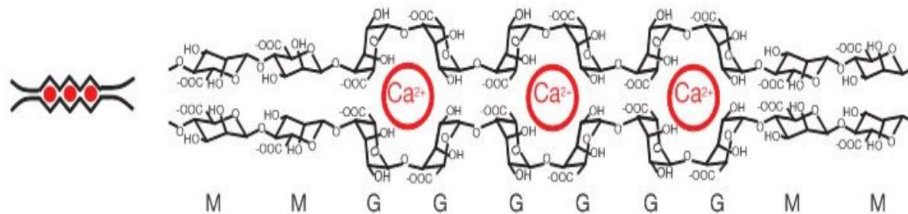


Figure 14: Two Alginate Chains in Proximity via Ca^{2+} ions. Reproduced with permission from [15]. Copyright 2012 Nature Publishing Group.

It was found that the optimal concentration of calcium was approximately 75 millimolar, which is far in excess of the ~ 1.15 mmol concentration of free calcium found in blood plasma.^[74] Thus, the amount of ionic crosslinking seen by the alginate chains would greatly diminish *in vivo* as the hydrogel equilibrates in a physiological environment. In a similar manner, monovalent cations that are present in serum, such as sodium and potassium, would complex with G blocks of single alginate chains and interfere with the calcium acting to pull two chains together. While these problems are circumvented by using deionized water, this also fails upon immersion in cell culture media or serum once the fluids reach equilibrium concentrations. Additionally, it leads to high cell death via lysis if the culture is encapsulated in a hydrogel whose base solvent is pure water. Thus, one is left with a choice: either design the hydrogel for excellent mechanical performance by using deionized water, or replace pure water with saline or cell media to sustain cell life. While a compromise was found by incorporating

a secondary collagen gel (with a base solvent of cell media) throughout the pores of a PEGDA-BSA network (whose base solvent was DI water), the relatively brittle collagen gel would fail before the PEGDA-BSA scaffold, and thus render the robust scaffold irrelevant. Building off of this, it was also found that the PEGDA-BSA hydrogel exhibited significant swelling beyond its initial water content, up to 3.3X its as-cast volume upon immersion in a water or saline bath. The high hydrophilicity of the PEGDA recruits additional water into the network, causing a reduction in mechanical properties via the increased strain on the PEGDA chains between crosslinking sites, as well as by reducing the percentage of solid material per volume.²

Oxygen inhibition is another limiting factor to the system. It has long been established that O₂ is a radical scavenger to form peroxy radicals,^[75] which are not reactive with the vinyl bond found in acrylate functional groups. Thus, acrylate polymerization is plagued by premature termination whenever a growing chain encounters an oxygen radical. This problem is circumvented by incorporating thiol moieties, which overcome oxygen inhibition via abstraction of the sulfurous hydrogen atom.^[76] The research in Chapter 4 leverages the ability of thiol-ene reactions to overcome oxygen inhibition, and is one of the motivating factors for the change in material system covered in this thesis.

² Since free water molecules cannot bear load, and there is now more water in the network, the result is reduced ultimate stress, toughness, and ultimate strain due to the pre-stretched nature of the chains.

3.4 Methods and Materials

3.4.1 PEGDA-BSA hydrogel fabrication

PEG powder was purchased from Sigma Aldrich and modified into poly (ethylene glycol) diacrylate (PEGDA) according to previously published protocols and dissolved in deionized water (DI, 40 wt %).^[77] Brown sodium alginate solution (5 wt %) was mixed with 40% PEGDA solution. After degassing the solution in a vacuum chamber, Irgacure 2959 (I-2959) and calcium sulfate slurry (1M CaSO₄·2H₂O) were added as photo initiator for PEGDA and ionic crosslinker for alginate, respectively. The mixture was then carefully poured into a glass mold and cured under ultraviolet light (365nm wavelength) for 10min. PEGDA chains covalently crosslink via radicals generated from the photo initiator (I-2959) when exposed to UV and form a covalent, ductile network capable of large deformation. In contrast, alginate is ionically crosslinked in the presence of divalent cations (such as Ca²⁺) and imparts stiffness into the network. These ionic bonds reversibly form, break, and reform in the hydrogel's aqueous environment and enable fast recovery after deformation. As the network is stretched, the ionically crosslinked alginate chains release entrapped divalent cations and dissipate applied mechanical energy while covalently crosslinked PEGDA elastically deforms in the direction of the load. When the hydrogel is released from stress, alginate recovers its crosslinking by recombining the calcium cations. After

curing, mechanical tests were performed at room temperature using a dynamic mechanical analyzer (RSA III, TA instruments, DE).

3.4.2 Digital Image Correlation

As is illustrated by Figure 15, digital image correlation is a non-contact optical technique that allows full-field strain measurement on a surface under deformation.^[78] A random speckle pattern was generated on the surface of a sample via spray painting. Images of speckle patterns at both the reference state and deformed state were recorded by a standard video camera during the process of the deformation. Based on the video, the commercial software VIC-2D (Correlated Solutions Inc., Columbia, SC) was applied to measure strain mapping of the deformed sample. Essentially, both images were transformed to grayscale matrices. To track the surface displacements of deforming materials, a mathematically well-defined correlated function was applied to match digitalized images before deformation and after deformation:

$$r(x, y) = 1 - \frac{\sum A(x, y)B(x^*, y^*)}{(\sum A(x, y)^2 \sum B(x^*, y^*)^2)^{0.5}} \quad (3.4.2.1)$$

$A(x, y)$ is the gray level at the location of (x, y) at reference state, $B(x^*, y^*)$ represents the gray level at the location of (x^*, y^*) at deformed state. The relation between (x^*, y^*) and (x, y) can be related as:

$$\begin{cases} x^* = x + u + \frac{\partial u}{\partial x} \Delta x + \frac{\partial u}{\partial y} \Delta y \\ y^* = y + v + \frac{\partial v}{\partial x} \Delta x + \frac{\partial v}{\partial y} \Delta y \end{cases} \quad (3.4.2.2)$$

Where u and v respectively represent the displacements in the directions of x and y . The displacements can be determined by minimizing the correlation function $r(x, y)$.

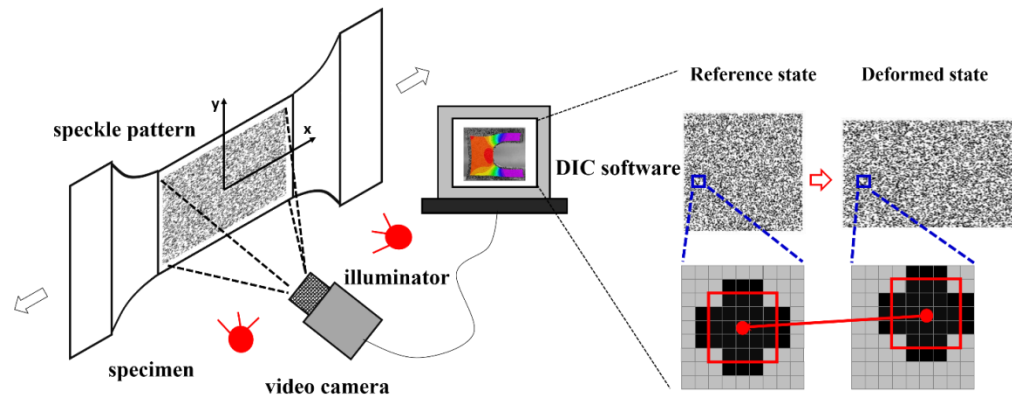


Figure 15: Digital Imaging Correlation Technique for Spatial Distribution of Strain.

3.4.3 Details of Cell Culture

Bone-marrow-derived hMSCs were provided by Tulane University Health Sciences Centre and cultured in α -minimum essential medium supplemented with 20% fetal bovine serum and 1% penicillin/streptomycin at 37 °C and 5% CO₂. The 4–7th passages of hMSCs were used in this study. HEK-293 cell line was obtained from ATCC (Manassas, VA) and cultured in Dulbecco's modified eagle medium (high glucose) with 10% fetal bovine serum and 1% penicillin/streptomycin. Cells were trypsinized with 0.25% Trypsin-EDTA (Life Technologies, Grand Island, NY) before being counted and mixed with the gel precursor solution.

3.4.4 Encapsulated Cell Viability Testing

To perform viability testing, the samples were washed in 1X Dulbecco's phosphate buffered saline before soaking in 2 μ M Calcein AM (Sigma-Aldrich, St. Louis, MO) and 5 μ M propidium iodide (Sigma-Aldrich, St. Louis, MO) solution for 30 min. Fluorescent images were taken using Zeiss LSM 510 inverted confocal microscope provided by Duke University Light Microscopy Core Facility.

3.4.5 Collagen gel preparation for cell encapsulation

Type 1 rat tail collagen (Corning Inc., Corning, NY) was diluted with 0.6% acetic acid (Sigma-Aldrich, St. Louis, MO) to a final collagen concentration of 2mg/ml. This solution was neutralized with 5M NaOH (Sigma-Aldrich, St. Louis, MO), and 10X α -minimum essential media (Sigma-Aldrich, St. Louis, MO) was added to a final concentration of 1X. HEK cells were added, and the solution formed a gel over the course of 30 minutes of incubation at room temperature.

3.4.6 Cell staining for stretch testing

The samples were fixed with 4% paraformaldehyde (Electron Microscopy Sciences, Hatfield, PA) for 30 min before staining with Alexa Fluor® 488 Phalloidin for the actin-filament network (Life Technologies, Grand Island, NY) and DAPI for the nucleus (Sigma-Aldrich, St. Louis, MO) for 1 hour. The samples were washed with PBS for three times before being mounted on a glass slide for imaging.

3.4.7 3D Printing PEG-alginate-nanoclay hydrogel

PEGDA–alginate mixture was prepared as described above, but Laponite XLG (final concentration 5 wt %) was first dissolved into deionized water, followed by PEGDA. This gel was allowed to homogenize and settle overnight, after which it was mixed in a 1:1 ratio with the 5 wt% alginate solution and allowed to equilibrate for one additional day. After degassing, I-2959 and CaSO₄ solution were added to the pre-gel solution. The PEGDA-alginate-nanoclay pre-gel solution was then loaded into extrusion cartridges, which were placed on the printing carriage of 3D printer for extrusion through a 15G-20G flat tip needle. During printing, the pre-gel solution experienced shear thinning inside the extrusion needle, and quickly regained its viscosity upon exiting. Following extrusion, the flat printed shapes were encased in glass slides and placed in the UV chamber to complete covalent crosslinking of the PEGDA polymer chains. Three-dimensional shapes were crosslinked in a sealed, nitrogenous environment under a 100mWcm⁻² UV source with emission peaks centered on 365nm. Since the viscosity of hydrogel was enhanced by adding nanoclay, it was able to be printed into various shapes free from vertical limitation (Figure 13a). Controlling the concentration of nanoclay in the gel permits the viscosity to be optimized for extrusion-based printing while still maintaining three dimensional structures without requiring support material (Figure 11).

Chapter 4. Thermomechanical Properties of Spiroacetal-based Thiol-ene Polymers

4.1 Introduction

While the thiol-ene reaction between thiols and unsaturated alkene compounds has been understood since the early 1900s,^[79] it has only been within the past two decades that thiol-ene “click” chemistry has developed into a mature and diverse field of study. Much of this is attributed to the high interest in click chemistry as a method of synthesis, which is characterized by near quantitative yields of highly specific compounds under facile conditions.^[80] Belonging to this category, thiol-ene polymerization is desirable for its fast reaction kinetics,^[81] homogenous network formation,^[82] and ability to control polymer backbone chemistry, functionality, and crosslink density.^[83] In recent years, several groups have used thiol-ene click reactions to synthesize materials for a wide variety of applications, including low-shrinkage dental fillings,^[84, 85] shape-memory materials,^[86] neurological probes,^[87, 88] photopatterned surfaces,^[89] microfluidic devices,^[90-92] films and coatings,^[81, 93] and optical networks that exhibit liquid crystalline behavior.^[88, 94-96] However, despite its many advantages, several limitations have been noted, including poor thermo-mechanical properties caused by flexible and nonpolar thioether linkages, strong odor of small thiol molecules, and a limited library of affordable and commercially available thiol monomers.^[81, 97]

As a result, much research has focused on incorporating different alkene moieties such as (meth)acrylates,^[81, 97] urethanes,^[98-101] and norbornenes^[102] along the polymer backbone to achieve desired material properties such as stiffness, elongation, and strength.^[89, 97, 98, 102] Tough thiol-enes have proven particularly elusive; the vast majority of thiol-ene polymers suffer from both low failure strain, caused by large amounts of crosslinking, and anemic stress-strain behavior due to a lack of energy dissipation present in the network. The toughest reported thiol-ene photopolymers have been thiourethanes and thiol-isocyanates,^[101, 103, 104] which harness a large amount of interchain hydrogen bonding to dissipate energy under deformation and improve mechanical performance, especially when polymerized into thermoplastics or elastomers that enable large deformation. Even tougher thiopolymers, which are unsurprisingly also thiourethanes, have been polymerized using non-photo techniques such as melt polymerization^[99, 100, 105] and Michael-addition.^[101] Outside of thiourethanes, however, there is an unmet need to expand the limited chemical library of thiol-ene materials with substantial mechanical robustness. To accentuate this, the toughest non-urethane thiol-ene photopolymer we found reported in the literature^[106] has a toughness near 12 MJ·m⁻³, which is approximately 33-50% that of the thiourethane photopolymers.

One molecular structure that is increasingly used for high performance applications are spirocyclic compounds, also known as spiranes. A spirocyclic polymer is one which contains two or more rings that share one common atom, which is most

frequently a tetrahedral carbon.^[107] The twisted ring nature of spiranes has been noted to result in polymers possessing high strength, toughness, and thermal stability.^[108] In particular, spirane compounds containing acetal linkages, or spiroacetal polymers, are eliciting investigation as stimuli-responsive materials,^[109, 110] hydrogels,^[111] and drug delivery platforms.^[112, 113] The high rigidity and crystallinity demonstrated by pure spiropolymers makes them difficult to process with heat or solvents, however, and therefore one approach is to balance these rigid segments with more flexible linkages to increase their workability as well as mechanical performance.^[114] To this end, we harness the precision and efficiency of thiol-ene polymerization to create tough, semicrystalline polymers from a neat monomer mixture using only ultraviolet light and photoinitiator to begin the reaction. Here we describe polymers made from a spiroacetal molecule, 3,9-divinyl-2,4,8,10-tetraoxaspiro[5.5]undecane (DVTU), and several linear and crosslinking thiol monomers. Furthermore, we investigate the interplay of polymer chemistry and crosslink density to better understand their influence on crystallinity and thermo-mechanical properties of these systems.

4.2 Materials and Methods

4.2.1 Materials

We obtained Tetrahydrofuran (THF) ($\geq 99.9\%$), 1,6-Hexanedithiol ($\geq 96\%$) (HDT), 1,3-Propanedithiol (99%), Trimethylolpropane tris(3-mercaptopropionate) ($\geq 95\%$) (TMPTMP), 2,2-Dimethoxy-2-phenyl-acetophenone (DMPA), and 3,9-Divinyl-2,4,8,10-

tetraoxaspiro[5.5]undecane (98%) monomers from Sigma Aldrich and used each as received with no further purification. DMPA acted as the ultraviolet (365 nm) photoinitiator and was added to monomer mixtures at a 0.1 wt% concentration. Monomer and photoinitiator structures are shown in Figure 16: Select thiol and alkene monomers

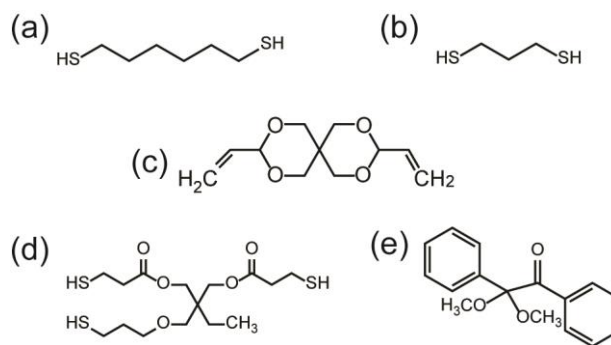


Figure 16: Select thiol and alkene monomers.

4.2.2 Methods

Sample Preparation. All polymers contained an equivalent amount of thiol and –ene functional groups to maximize polymerization efficiency, and were made following a previously described protocol.^[89] In brief, we mixed liquid monomers with photoinitiator in a clean glass vial and warmed the mixture to 75°C in an oven to melt the crystalline DVTU, which has a melting temperature of approximately 45°C. We cast the monomer mixture between parallel glass slides separated by 1mm thick rubber spacers and held in place by clips. Prior to casting, we cleaned glass slides with acetone and buffed them with Rain-X® twice to accommodate a clean release from the polymer. After casting, a UVL UL-1000 ultraviolet chamber irradiated the monomer mixture with

365 nm light for 60 minutes. We observed some crystallization had occurred immediately following photopolymerization of thermoplastic and lightly crosslinked samples, as evidenced by the DSC heating scans shown in Figure 17: DSC heating curves of samples with varying crosslink density immediately after photopolymerization.. The early appearance of the high temperature endotherm is attributed to larger lamella crystallite formation, while the low temperature endotherm is attributed to thinner lamella that form during secondary crystallization over time. More crosslink content slows the kinetics of crystallization, which masks the endotherm(s) from appearing in these samples immediately post photopolymerization, as shown by the 20 tmol% curve in red. Finally, polymer samples entered a postcure oven at 85°C for 24 hours to finish polymerization, remove any crystallinity that formed during the photopolymerization, relieve internal shrinkage stress, and release unreacted monomers from the bulk. Following postcure, we shut off the oven and allowed it to slowly cool back to room temperature according to Newton's Law of Cooling:

$$T(t) = T_a + (T_0 - T_a)e^{kt} \quad (4.2.2.1)$$

where $T(t)$ is the internal oven temperature at t minutes, T_a is the room temperature (22°C) surrounding the oven, T_0 is the initial internal oven temperature (85°C), and k is the oven-specific cooling constant, which was found to be -0.0107 min^{-1} .

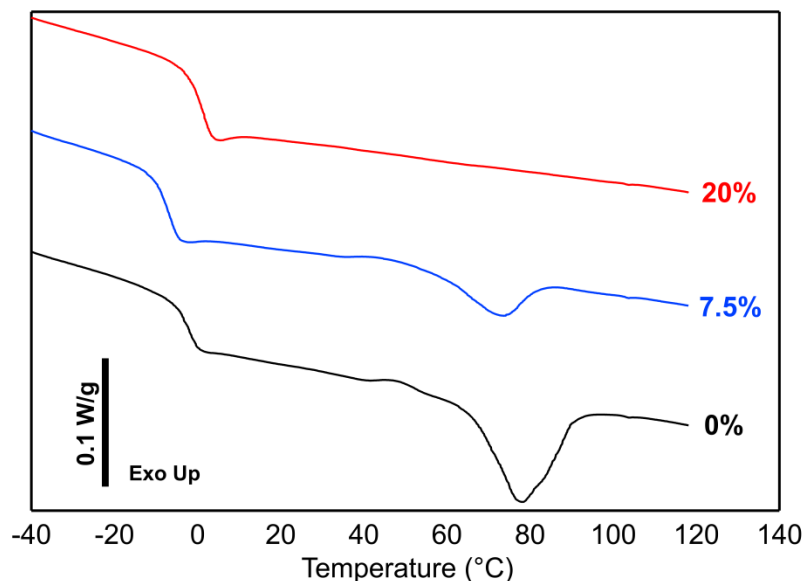


Figure 17: DSC heating curves of samples with varying crosslink density immediately after photopolymerization.

Samples annealed at 22°C after removal from the oven to allow crystallinity to reach equilibrium. Equilibrium ensured that maximum energy dissipation was achieved for each composition of HDT-TMPTMP-DVTU. Below, Figure 18: Optical characterization of semicrystalline morphology in HDT-TMPTMP-DVTUs. illustrates the compositions of HDT-TMPTMP-DVTUs considered here and the effect crosslinker concentration has on opacity: Increasing concentration of crosslinker leads to decreasing opacity. Ratios above samples indicate chain-builder thiol to crosslinking thiol monomer proportions.

where A_m and A_p are the areas under the thiol and alkene peaks of the monomer solution and polymer disk, respectively. Peaks used in the calculations were the -SH stretching vibration at 2550-2590 cm^{-1} and terminal methylene group stretching in vinyl alkenes at 3075-3095 cm^{-1} .^[115] Functional group conversion reported is the mean of a minimum of 3 samples.

We confirmed spherulite crystal presence using transmitted polarized light microscopy on a Zeiss Axio Imager Z2 Upright Microscope with a differential interference contrast analyzer and AxioCam 506 color camera. We examined films with crosslinking compositions ranging from 0% to 20% after subjecting them to the postcure and annealing procedure previously described. Following this, we imaged the films at 600X in oil at 22°C.

Thermo-mechanical Analysis. We performed differential scanning calorimetry using a TA Instruments Discovery DSC. We pressed polymer disks of approximately 7mg into aluminum pans and subjected them to a heat-cool-heat thermal analysis between -50°C and 120°C at 10°C per minute under nitrogen. We calculated glass transition temperature (T_g) on the second heating ramp as the midpoint between the onset and endset transition temperatures, which are defined as intersection temperatures between lines tangent to the steady state and transition slopes. We calculated mass-normalized enthalpy fusion as the integral of the melting peaks relative to samples' baselines during their first heating ramp.

~15mg discs of HDT-TMPTMP-DVTUs of all compositions acted as samples for gel fraction analysis. We immersed each sample in 20ml of pure THF solvent for 3 days at room temperature to swell the network and wash out all solids content unincorporated in the crosslinked network; following this, we removed the samples from the THF and boiled off all absorbed solvent at 70°C for 3 additional days. Gel fraction, g , of the materials is recorded as

$$g = \frac{m_o}{m_s} \quad (4.2.2.3)$$

where m_o and m_s are the mass of the disc before and after THF exposure and drying, respectively.

A TA Instruments Q800 DMA subjected rectangular thiol-ene samples measuring 1 mm by 3 mm in cross-section to a strain of 0.1% at 1 Hz while heating from -40°C to 120°C at 3°C/min. We report glass transition temperature as the maximum of the $\tan\delta$ versus temperature plot (Figure 24: $\tan\delta$ curves of HDT-TMPTMP-DVTUs.), and glassy and rubbery moduli as the maximum and minimum recorded moduli, respectively. We averaged a minimum of three samples of each for thermal transition data.

We measured stress-strain behavior on a TestResources 830 Axial Torsion System equipped with a 440N load cell by straining ASTM D638 Type V dogbone samples in tension at a rate of 5 mm·min⁻¹ at 22°C. For screening purposes, we computed strain using crosshead displacement divided by initial gage length; we then assessed strain of

select compositions with an Imetrum non-contact video and software package to understand their stress-strain response more thoroughly. Briefly, a video capture system tracked the strain of markers made inside the dogbone gage length; this ensured only deformation within the homogenous region was recorded. We calculated toughness as the area under the σ - ε curve (units of volumetric energy absorption, $\text{J}\cdot\text{m}^{-3}$); discussion of toughness throughout this article implies the same, and so excludes different metrics of toughness, such as results of Charpy or Izod tests, which report planar or linear energy absorption ($\text{J}\cdot\text{m}^{-2}$ or $\text{J}\cdot\text{m}^{-1}$) under different testing conditions.^[116] Engineering strain and stress were used in all calculations.

4.3 Results

4.3.1 Functional Group Conversion

We analyzed samples of HDT-DVTU, TMPTMP-DVTU, and PDT-DVTU polymers to assess the effect of holding samples at 85°C for 24 hours on degree of polymerization following ultraviolet-initiated radical polymerization. Consistent with previous reports in thiol-ene literature, all polymer samples exhibited high conversion ($\geq 91\%$) of their constituent monomers, with modestly higher alkene conversion.^[81, 82, 117, 118] Alkene monomers with dipole moments near their terminal vinyl bonds, as is the case with (meth)acrylates, are known to homopolymerize during radical polymerization. However, we determined that DVTU underwent no measureable homopolymerization when we compared the characteristic peaks in the monomer and photoinitiator mixture

before and after UV exposure. Furthermore, exposing the mixture to postcure conditions for 24 hours also did not cause any self-reaction. In general, we found that all polymer samples reached high conversion upon exposure to UV light; this is further indication that the polymerization proceeds in a step-growth fashion and benefits from a delayed gelation point, which permits mass transfer of oligomers and facilitates high conversion of their functional groups. Upon treatment of 24hr, 85°C postcure, the samples exhibited a modestly increased thiol conversion. We believe that increased thermal agitation of the polymer network allows small, unreacted thiol molecules to escape from the bulk and therefore slightly increases their measured conversion. Figure 19 shows a representative IR spectrum for HDT-TMPTMP-DVTU-7.5, and Table 9 in Appendix C summarizes extent of polymerization data for three thiol-alkenes and one thiol-thiol-alkene.

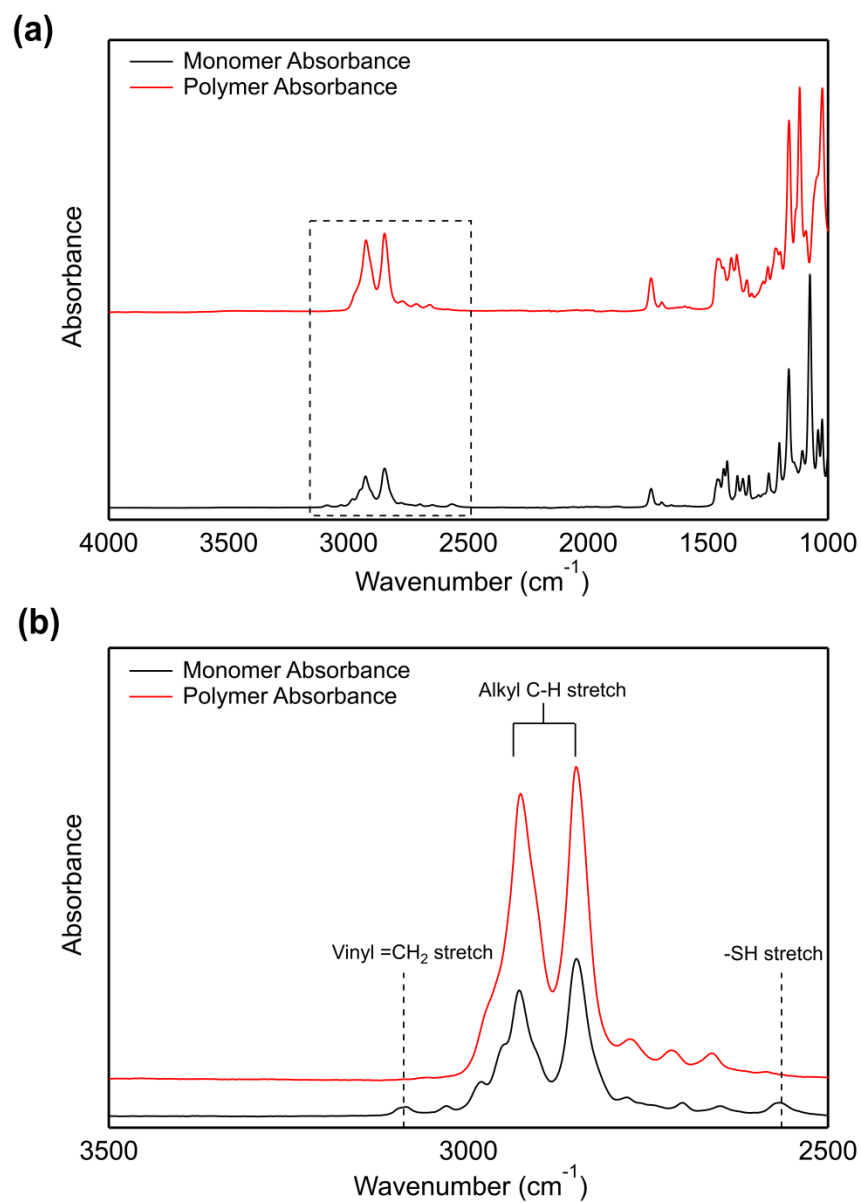


Figure 19: Representative IR spectrum for HDT-TMPTMP-DVTU-7.5. A. Full IR scan. B. Close-up of region of interest.

4.3.2 Crystallinity and Thermal Transitions

Figure 20 illustrates the crystallization of HDT-TMPTMP-DVTU-7.5 following the latter portion of the classic Avrami “S” curve, in which an early period of rapid nucleation and growth is followed by small increases in crystalline content via secondary crystallization and enthalpic relaxation as the chains adapt their lowest free energy conformations.^[119, 120] As Figure 20a and Figure 20c exemplify, crystallinity of HDT-TMPTMP-DVTUs increases steadily over time with annealing at 22°C until equilibrium is reached and maintained for all longer time points. The increasing population of crystallites increases opacity over time (Figure 20b), as well as broadening and raising the glass transition range during initial DSC heating ramps. Endotherms reach steady state by day 4 of annealing. Annealing at higher temperature shifts the lower endotherm upwards as lamella grow, while the more stable lamella responsible for the higher endotherm remain unaffected. A “shelf”, indicative of lamella either still growing or at their original thickness, is present between the low temperature endotherm from 22°C annealing and the low temperature endotherm of the same material as it has anneals at 30°C.

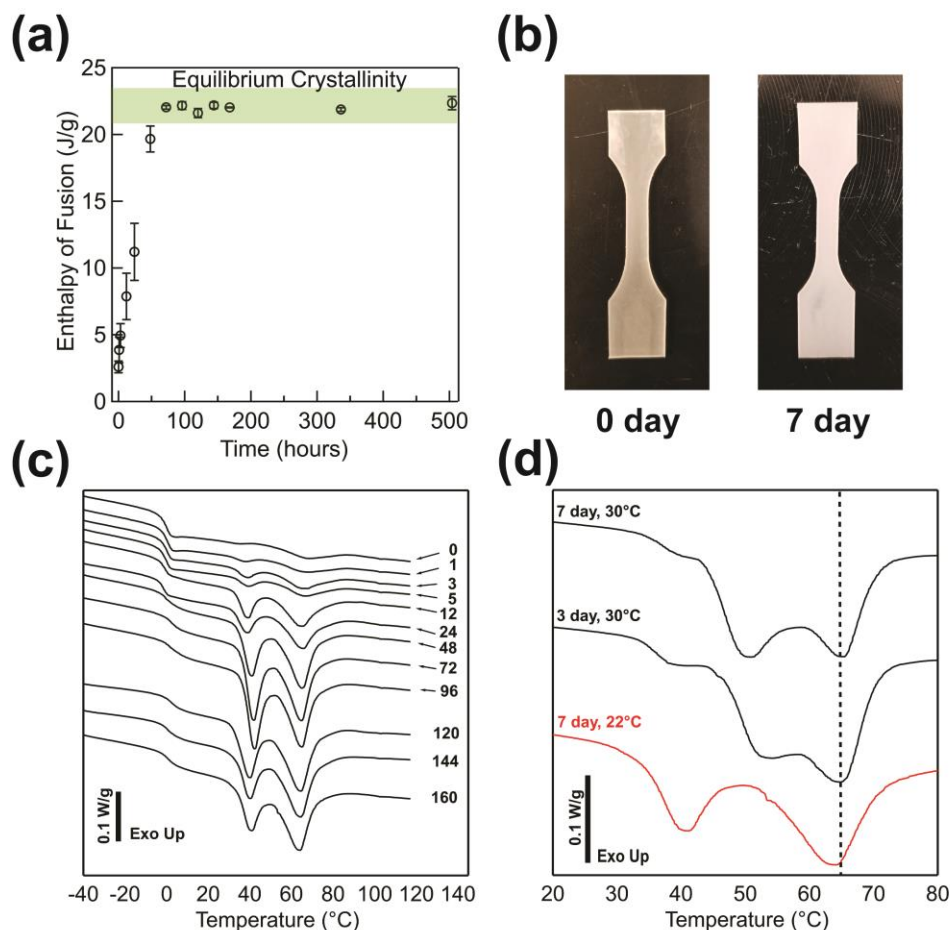


Figure 20: Crystallization behavior of HDT-TMPTMP-DVTUs over time. A. Material reaches equilibrium within three days. B. As-made versus annealed shows opacity increasing alongside crystallinity. C. DSC stacks over time show increasing melting endotherms and T_g broadening. D. Effect of elevated annealing temperature on thermal behavior.

We detected spherulites by polarized light microscopy (PLM) for HDT-TMPTMP-DVTU samples containing up to 12.5 thiol mol% ($t_{mol}\%$) TMPTMP. Maltese crosses couldn't be seen in samples with higher crosslink density; however, samples with crosslink density as high as 20 $t_{mol}\%$ still exhibited semicrystalline characteristics such as opacity and endothermic valleys in DSC heating curves. Qualitative analysis of

polarized images (Figure 21) revealed a spherulite size roughly $10\mu\text{m}$ in diameter for HDT-DVTU and HDT-TMPTMP-DVTU-5, and $\sim 5\mu\text{m}$ for HDT-TMPTMP-DVTU-10. Furthermore, polymers below 10% TMPTMP content exhibited clear extinction patterns within the Maltese crosses, while HDT-TMPTMP-DVTU-10 showed less regularity and appeared less spherical. This suggests that crosslinking starts to reach a critical density at 10 $t_{\text{mol}}\%$ TMPTMP and severely disrupt spherulite formation, resulting in fewer, smaller lamella and more amorphous volume.

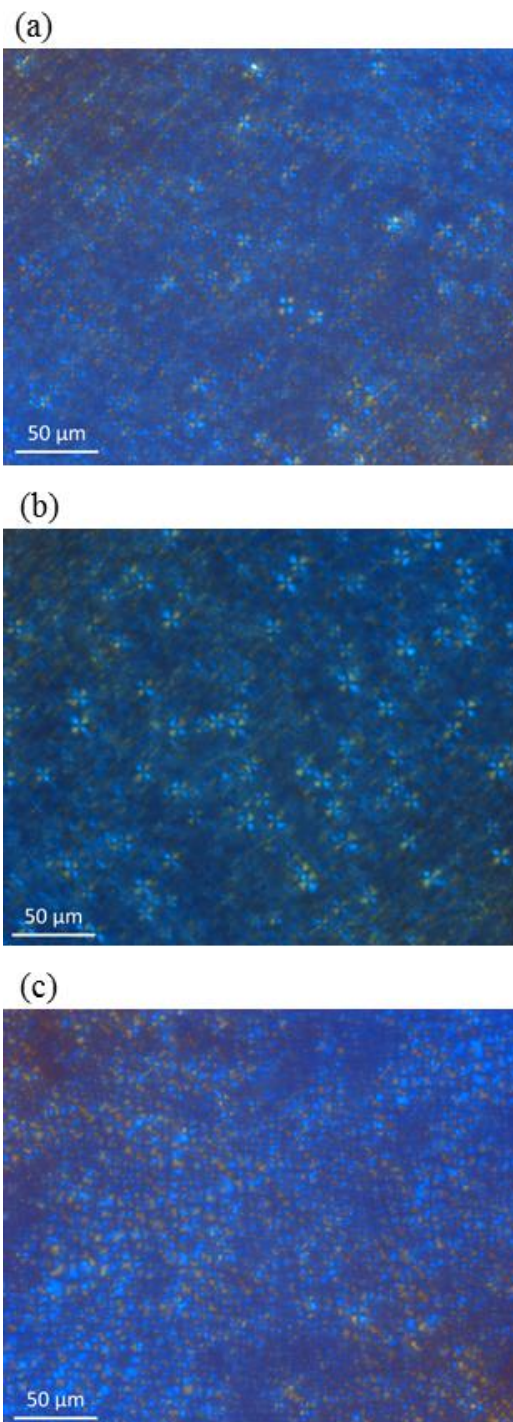


Figure 21: Polarized images of HDT-TMPTMP-DVTUs reveal characteristic Maltese cross patterns of spherulite crystals. A. HDT-DVTU B. HDT-TMPTMP-DVTU-5. C. HDT-TMPTMP-DVTU-10.

We used DSC to elucidate the effect of crystallinity and crosslink density on glass transition temperature, enthalpy of fusion, and melting temperatures of crystalline domains in the semicrystalline polymers. Figure 22 shows stacked representative heating curves of HDT-TMPTMP-DVTU polymers at equilibrium crystallinity and summarizes the endotherm temperatures, glass transition temperature, and mass-normalized enthalpy of fusion. We found that the glass transition temperature of HDT-TMPTMP-DVTUs generally increased with higher crosslink density, except between 17.5% TMPTMP and 20% TMPTMP, where the T_g decreased by approximately 1.1°C. We believe that this small decrease is caused by the large reduction of crystallinity in the polymer at this crosslink density, thereby suppressing physical crosslinks from the material and reducing T_g .

We attribute the two endotherms in Figure 22 to populations of lamella of varying thickness in the bulk polymer. The low temperature endotherms reflect the presence of relatively thin, less-perfect lamella, and the higher temperature endotherms indicate species of more stable, thicker lamella. Thicker lamella commonly form early in many annealed, semicrystalline polymers such as polyamides,^[121] polyethylene,^[121, 122] polycaprolactone,^[123] ethylene/vinyl acetate copolymers,^[124] and poly(aryl ether ether ketone),^[125-127] and are followed by the formation of thinner lamella during secondary crystallization over longer annealing times. Our findings indicate that the spiroacetal thiol-enes described herein act exactly in this manner. The high temperature endotherms

are initially more present immediately following polymerization of thermoplastic and lightly crosslinked samples (Figure 17), and while both endotherms grow in intensity with annealing time (Figure 20c), only the lower temperature endotherm shifts to a higher temperature when we raise the annealing temperature to 30°C (Figure 20d). By examining HDT-TMPTMP-DVTU-7.5 over multiple time points, we show the population of thin lamella growing and elevating their endotherm by an average of 6-8°C, which corroborates with literature reports of lower endotherm presence 5-25°C above annealing temperature.^[121, 122, 125, 126] The high endotherms shift to lower temperatures and also become shallower with higher crosslink content, which suggests that increasing TMPTMP concentration increases the relative amount of amorphous volume in the networks and reduces the average size of the crystals formed. Xue *et al* reported that the crystal melting point depression is inversely proportional to the crystal radius in the relationship,^[128]

$$\Delta T = T_0 - T = \frac{2T_0\sigma V_m}{\Delta_s^l H_m r} \quad (4.3.2.1)$$

where T_0 , T , r , σ , V_m and $\Delta_s^l H_m$ are the melting point of the bulk crystal, the melting point of a crystal with radius r , surface tension, molar volume, and molar heat of fusion, respectively. The melting point depression of the secondary endotherm of HDT-TMPTMP-DVTUs generally fits the above relationship, and reinforces the results from PLM that average crystal radius decreases with increasing crosslinking. We believe the lower temperature endotherm would similarly be reduced in temperature at sufficiently

high crosslinking, but the continued reduction in endotherm magnitude during DSC heat scans that accompanies more TMPTMP content inhibits our ability to measure this effect. Furthermore, the data in Figure 22 suggests that the initial small additions of crosslinker (i.e. the transition from 0 to 2.5 and 2.5 to 5 $t_{\text{mol}}\%$ TMPTMP) have the largest effect on reducing crystallite size. This agrees with the intuition that early additions of crosslinking have the biggest effect on limiting chain mobility by introducing covalent anchor points throughout the network. For visual clarity, E1, E2, Ef, and Tg in Figure 22b denote low temperature endotherm, high temperature endotherm, mass-normalized enthalpy of fusion, and glass transition temperature, respectively.

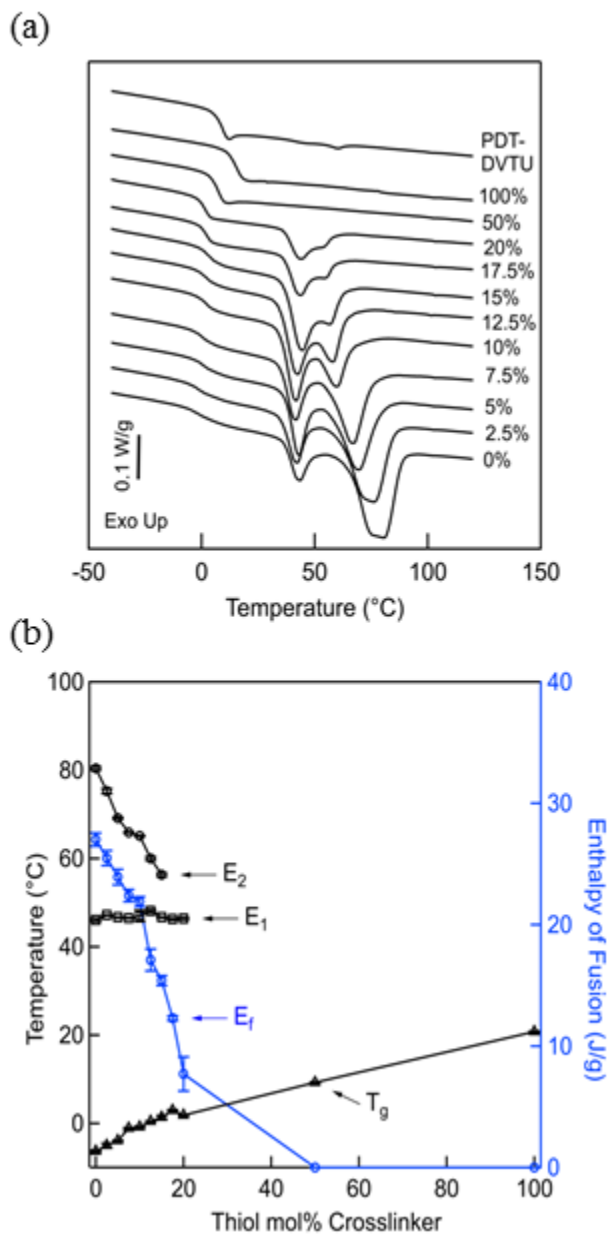


Figure 22: DSC curves and data for various HDT-TMPTMP-DVTU compositions. A. DSC heating curves of HDT-TMPTMP-DVTU compositions, labeled by tmol% TMPTMP. B. Thermal properties of HDT-TMPTMP-DVTUs as a function of crosslink concentration.

Shown in Figure 22a, the fusion enthalpy of the high temperature endotherm is initially significantly larger than that of the low one, but is definitively smaller once

TMPTMP concentration reaches 10 $t_{mol}\%$. This is because crosslinks act to disrupt larger lamella at lower concentrations than they do small ones. Thus, higher crosslinking drives the dominant population of crystallites to smaller sizes in parallel to reducing overall crystallinity. We found that the largest decrease in total melting enthalpy occurs at crosslink concentrations between 10 and 12.5 $t_{mol}\%$, between which the mass-normalized enthalpy of fusion dropped from approximately 22 J/g to 17 J/g. This supports our findings from PLM, which located the critical threshold of crosslink concentration at $\sim 10 t_{mol}\%$. Crosslinker concentrations between 12.5 and 20 $t_{mol}\%$ further reduced enthalpy of fusion, and samples with 50 and 100 $t_{mol}\%$ TMPTMP did not exhibit any measurable melting enthalpy, which indicates a sufficiently densely crosslinked network to completely remove all crystallinity. Furthermore, the glass transition regime was more clearly defined in samples containing larger amounts of crosslinker, which arises in more homogenous networks with less crystal content and shorter average chain lengths between crosslinks.

For comparison, a heating curve of PDT-DVTU (no chemical crosslinker) is stacked above the HDT-TMPTMP-DVTU curves in Figure 22a. It is clear that the presence of propanedithiol segments in the alternating copolymer significantly decrease its crystallinity, as evidenced by a single shallow endotherm and a sharply defined glass transition region. Because PDT has a lower mass per mole of thiol functional groups than HDT (54.12 g/mol versus 75.16 g/mol of terminal -SH moieties), PDT-DVTU

polymer contains more DVTU by weight than HDT-DVTU; therefore it appears that the increased spacing between DVTU molecules in HDT-DVTU increases crystallinity more so than higher DVTU content. We attribute this observation to the greater flexibility of each polymer chain in HDT-DVTU, which enables more chain realignment into organized lamella during the cooling from postcure and annealing at room temperature. Enthalpy of fusion, melting endotherms, and glass transition temperatures for all compositions of HDT-TMPTMP-DVTUs, as well as for PDT-DVTU and crystalline DVTU monomer, can be found in Table 6: Enthalpy of fusion, crystalline melting temperatures, and glass transition temperatures of various compositions of PDT- and HDT-TMPTMP-DVTU polymers as measured by DSC.

4.3.3 Thermo-mechanical Behavior

As illustrated in Figure 23, we investigated HDT-TMPTMP-DVTU samples of TMPTMP content ranging from 0 to 100 t_{mol}% by dynamic mechanical analysis to better understand how crosslinking and crystallinity interact to affect thermo-mechanical properties in the glassy, transition, and rubbery temperature regimes. At glassy temperatures, the stiffness of every composition of HDT-TMPTMP-DVTU copolymers ranged between 1.1-2.3 GPa, which is comparable to most amorphous and semicrystalline polymers.^[129] The glassy modulus for samples with 15 t_{mol}% TMPTMP or less was consistently above 2 GPa, while all samples with greater than 15% TMPTMP were softer than 2 GPa. We believe the decreasing glassy modulus results from both

diminishing crystallinity and reduced spiroacetal content (by weight) in specimens with higher TMPTMP content. Samples without crosslinking melted completely at temperatures beyond the high-temperature endotherm from DSC, and the first sample to exhibit a rubbery plateau beyond the glass transition temperature was HDT-TMPTMP-DVTU-5, which occurred beyond Figure 5 truncation. This agrees with the gel fraction data in Table 7, which indicates that substantial network formation does not occur until 5 t_{mol}% TMPTMP, and increases with further crosslinking. Samples containing 2.5 t_{mol}% TMPTMP deformed until the strain limit on the DMA was reached, which prevented us from obtaining a rubbery modulus. In samples with a rubbery plateau, the rubbery modulus was found to increase with increasing crosslinking content, following a well understood relationship,^[129, 130]

$$E_r \propto \frac{\rho RT}{M_c} \quad (4.3.3.1)$$

where E_r is the rubbery plateau modulus, R is the universal gas constant, T is the absolute temperature of the polymer, ρ is polymer density, and M_c is the molar mass between crosslinks. Furthermore, the higher gel percentage of polymer found at higher TMPTMP concentrations also contributes to raising the rubbery modulus, since greater network incorporation allows for a higher fraction of the material to stretch elastically instead of flowing beyond the melting temperature.

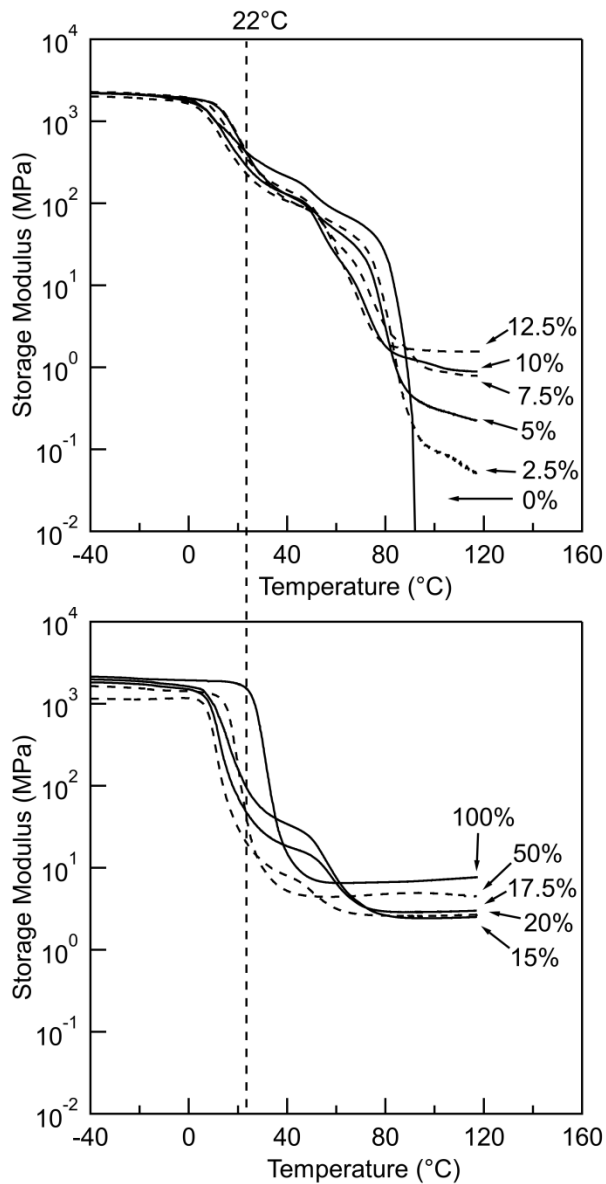


Figure 23: DMA scans of HDT-TMPTMP-DVTUs, listed by $t_{\text{mol}}\%$ TMPTMP. Tensile testing temperature (22°C) is demarcated by a vertical dashed line.

While the glassy and rubbery behavior of HDT-TMPTMP-DVTU polymers is fairly straightforward, their thermo-mechanical behavior is more nuanced throughout the transition temperature region (approximately 10°C to 100°C). Samples having ≤ 15

$t_{\text{mol}}\%$ TMPTMP exhibit two “shoulders” in their modulus versus temperature curves: the low temperature shoulder occurs approximately at 47°C and is independent of crosslinker density, and the higher temperature shoulder appears to shift from 80°C in HDT-DVTU down to 60°C in HDT-TMPTMP-DVTU-15. The occurrence of both shoulder regions, as well as the downward trend of the high temperature bend with increasing crosslinker, corroborate the DSC results from the previous section and correspond to thermal transitions linked to crystal melting. HDT-TMPTMP-DVTU-17.5 and HDT-TMPTMP-DVTU-20 only exhibit the low temperature shoulder; this suggests that while there may still be thicker lamella presence detectable by DSC, the population of these crystallites is too small to appreciably reinforce material modulus above 47°C. The low temperature shoulder disappears beyond HDT-TMPTMP-DVTU-20 and supports the concept that the network crosslinks are too dense to permit significant chain rearrangement into crystalline morphologies.

As shown in Figure 24 and the data of Table 7, clear trends in the thiol-ene thermomechanical behavior as a function of crosslink concentration emerge. The first is increasing homogeneity with increasing crosslinking, which is demonstrated by the full width at half-maximum (FWHM) of the $\tan\delta$ curve decreasing as TMPTMP content rises. Assuming random dispersion of TMPTMP monomers during polymerization, a higher concentration naturally causes a smaller distribution of chain lengths between crosslinks, and therefore a more narrow temperature range over which these segments

relax. Additionally, the reinforcing presence of crystals diminishes as crosslinking increases, which is illustrated by the large decrease in T_g and FWHM between samples containing 12.5 and 20 $t_{mol}\%$ TMPTMP. At 50 $t_{mol}\%$ TMPTMP, the networks are highly crosslinked, amorphous, and homogenous; because of this, additional crosslinking has no noticeable effect on FWHM. Last, the high gel fraction of these tightly crosslinked networks suppresses the broadening effect unincorporated polymer loops and chains have on the FWHM and so further sharpen their softening temperature range by nearly eliminating soluble content inside the networks of high crosslink compositions.

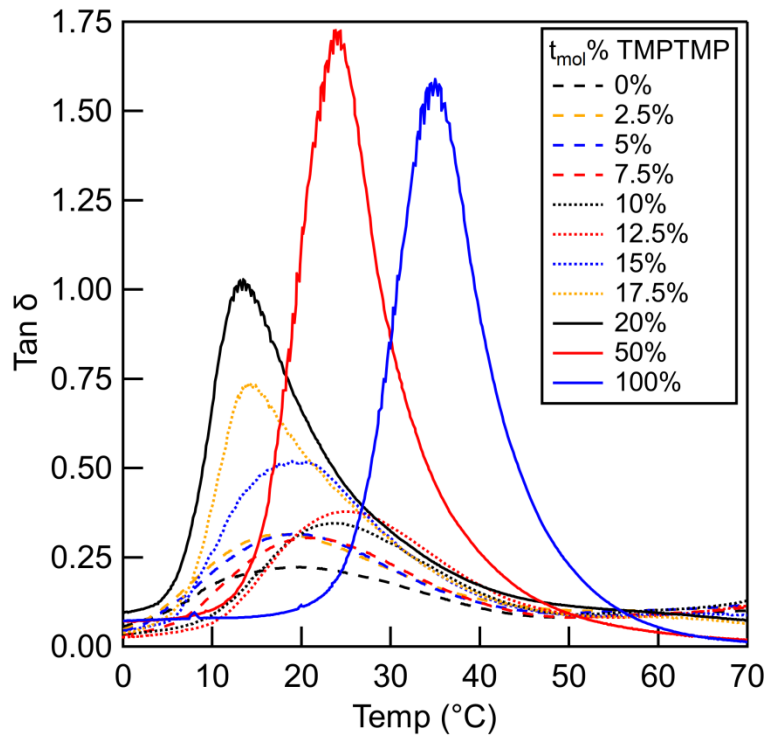


Figure 24: Tan δ curves of HDT-TMPTMP-DVTUs.

A second observable trend is the monotonic decrease of Young’s modulus at T_g with increasing crosslinking. Because crosslinks act to disrupt and reduce crystallinity in the thiol-enes, more crosslinking steadily reduces the stiffening effect of rigid crystalline domains at T_g . Further, the largest decrease in modulus occurs between 12.5 and 15 $t_{mol}\%$ TMPTMP; we find this in agreement with DSC and PLM results in identifying a “critical density” of crosslinks near 10-15 $t_{mol}\%$, beyond which crystallinity is severely reduced. Tabulated values for glassy modulus, rubbery modulus, T_g determined via $\tan\delta$ peak, as well as the maximum intensity of $\tan\delta$ values are found in Supplemental Table 2.

In Figure 25, glass transition temperatures are plotted as a function of TMPTMP content for both DSC and DMA measurements. For comparison, the predictions of the Fox equation for each dataset are plotted as well.^[131] The Fox equation describes the T_g of a polymer blend or copolymer as

$$\frac{1}{T_g} = \frac{w_1}{T_{g1}} + \frac{w_2}{T_{g2}} \quad (4.3.3.2)$$

where T_g , T_{g1} , and T_{g2} are the glass transitions of the blend, component 1 (HDT-DVTU), and component 2 (TMPTMP-DVTU), respectively, and w_1 and w_2 are the weight fractions of (HDT-DVTU) and (TMPTMP-DVTU), respectively. While the Fox equation is typically employed to understand the glass transition behavior of statistical copolymers and polymer blends, McNair *et al* successfully demonstrated its ability to accurately model the T_g s of crosslinked, ternary thiol-ene networks due to similar reactivities of constituent monomer species and relatively fast polymerization

kinetics.^[117] The Fox equation tracked closely with the DSC results, especially for both very low and very high TMPTMP concentrations, while mildly underestimating T_g for moderate crosslink densities of 7.5-17.5 $t_{mol}\%$. In general, the Fox calculation extrapolates intermediate T_g values based on the weight fraction of boundary cases (pure thermoplastic and complete thermoset, respectively for HDT-DVTU and TMPTMP-DVTU). As a consequence, materials containing modest crosslink densities exhibit a T_g higher than predicted due to the combined effects of crystallinity and crosslinking. Each component used in the calculation, however, is missing one of these T_g -raising factors; namely, HDT-DVTU has no crosslinking effects and TMPTMP-DVTU is devoid of crystallinity - the result is a theoretical prediction which mildly undershoots the compositions that benefit from both factors in concert.

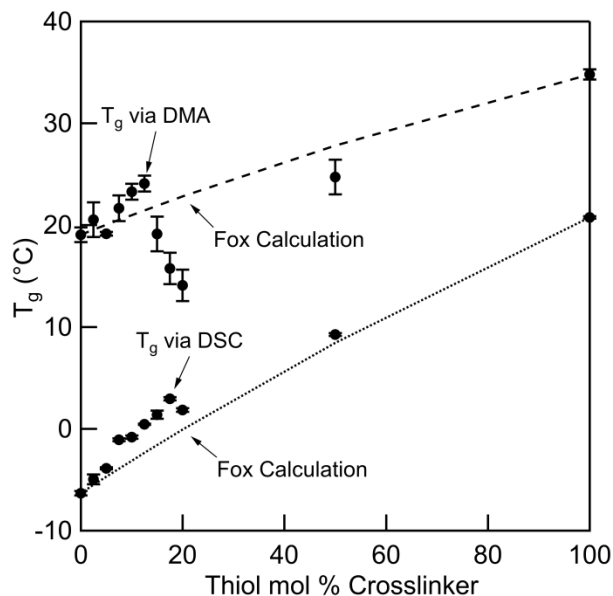


Figure 25: A comparison of T_g s as a function of crosslinker density in HDT-TMPTMP-DVTUs between DSC and DMA techniques, with the Fox equation used as a theoretical baseline.

T_g by DMA, in similar fashion to T_g by DSC, closely matches the Fox equation for low TMPTMP concentrations (0-5 $t_{mol}\%$) and mildly exceeds calculated values for moderate densities of 7.5-12.5 $t_{mol}\%$. Curiously, however, experimental DMA T_g drops significantly below the predicted T_g for TMPTMP concentrations of 15-20 $t_{mol}\%$. We hypothesize this is due to crystallites having a larger effect on DMA T_g (maximum mechanical damping at the peak of the $\tan\delta$ versus temperature curve) than TMPTMP crosslinks. Thus, samples with significant crystalline content (samples with $\leq 12.5 t_{mol}\%$ TMPTMP) have a higher T_g , and the diminished presence of these factors drops the transition temperature $\sim 10^\circ\text{C}$ between HDT-TMPTMP-DVTU-12.5 and HDT-TMPTMP-DVTU-20. Not until TMPTMP content is increased to 50 $t_{mol}\%$ does the T_g of the polymer

rise back above that of HDT-TMPTMP-DVTU-12.5. Thus, while the Fox equation is helpful in approximating the glass transition temperature of many amorphous thermoplastic and thermoset polymers, the glass transition temperatures of these semicrystalline thiol-ene networks appear to depend on both chemical composition and morphology, and presents an opportunity for future work to determine a more rigorous T_g prediction model incorporating crystal parameters such as average grain size and/or crystalline volume fraction.

4.3.4 Tensile Deformation Behavior

To better understand how crystallinity and crosslink density affect the mechanical behavior of PDT- and HDT-TMPTMP-DVTUs, we strained samples of varying TMPTMP content in tension at room temperature until failure and plotted the results in Figure 26. Both HDT-DVTU and PDT-DVTU are brittle and exhibit higher yield strength and lower failure strain than any crosslinked variations. We attribute low failure strain to the absence of TMPTMP monomers; these thermoplastic materials cannot deform significantly before fracture and thus demonstrate poor toughness. Additionally, we believe the high crystallinity found in the thermoplastic HDT-DVTU contributes to early failure of the material by crack propagation between crystal boundaries; during testing we observed that these samples broke prior to any necking behavior and had a rough and jagged fracture pattern, whereas crosslinked samples failed after significant necking and with a qualitatively smoother fracture. The high

yield strength is a result of the reinforcing effect of crystallinity; in fact, yield strength directly correlates with the relative crystal content for HDT-TMPTMP-DVTUs. Previous investigations have identified crystallinity as one of the primary influencing factors on yield strength;^[129, 132, 133] therefore, as we expected, the largest drop in HDT-TMPTMP-DVTU yield strength occurs between 10 and 12.5 $t_{\text{mol}}\%$ crosslinker, because the transition between these two TMPTMP concentrations is where crystallinity decreases most significantly.

Samples with higher crystallinity also exhibited larger upper-to-lower yield stress ratios, defined as the difference in stress between the yield point and lowest recorded stress at strains beyond the yield point. This phenomenon suggests that spherulite presence is the most significant barrier to early plastic deformation in the thiol-enes, even more so than crosslink density or T_g of the polymer. A high ratio of upper to lower stress indicates large early resistance to plastic deformation, but once this deformation is activated, the material offers relatively little resistance to resist further chain motion. Ideally, then, the toughest materials would have both a high yield point and a small ratio, which would describe substantial early resistance to deformation as well as continued energy dissipation at higher strains.^[133] While yield stress and yield ratio were directly coupled in PDT- and HDT-TMPTMP-DVTUs, it is possible that even tougher materials could be made by incorporating additional energy dissipation mechanisms along the polymer backbone such as motifs that partake in significant

hydrogen bonding to hinder chain motion and thus limit the early decrease in stress after the yield point.

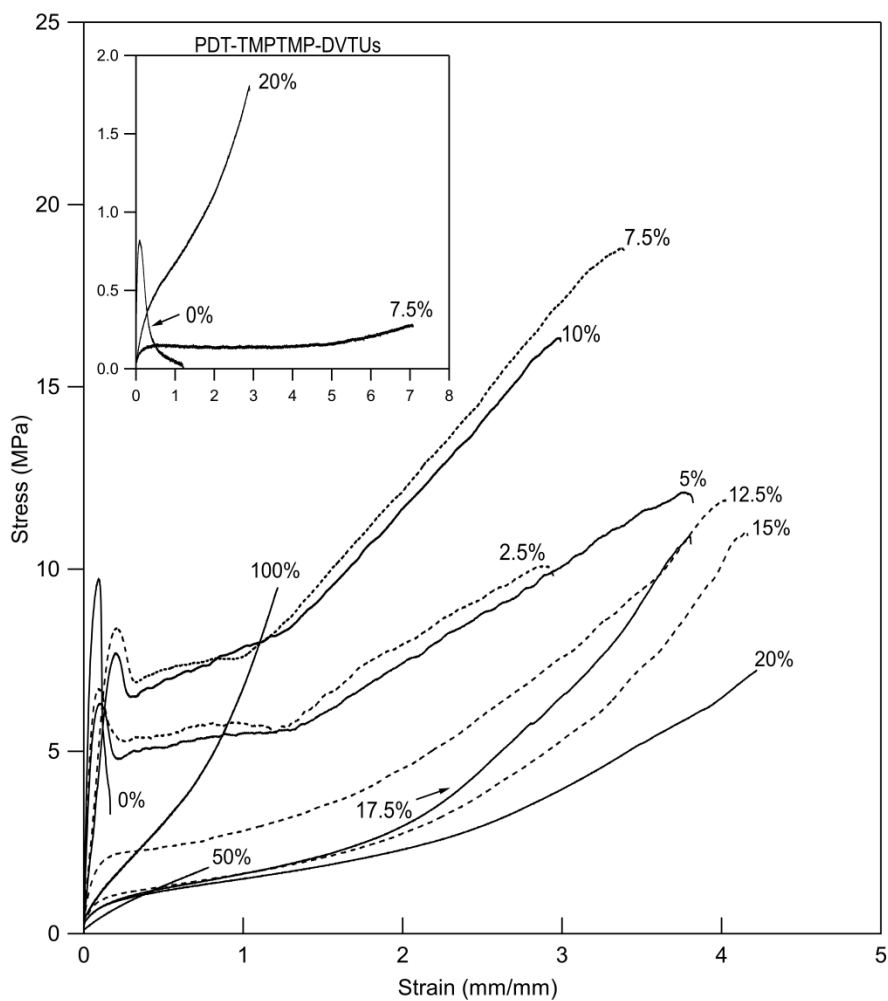


Figure 26: Stress-strain curves for HDT-TMPTMP-DVTUs. Samples are labeled to indicate $t_{\text{mol}}\%$ thiol monomers attributed to TMPTMP.

As crosslink density increases, failure strength, ultimate tensile strength, and toughness climb until reaching their peak values at 7.5 $t_{\text{mol}}\%$ TMPTMP; these metrics regress with additional increments of TMPTMP. Early additions of TMPTMP (2.5, 5, and

7.5 $t_{\text{mol}}\%$) reinforce the network by distributing applied loads more homogeneously across all connected polymer chains while minimally disrupting lamella and spherulite formation. Furthermore, as these samples stretch, they transition from opaque to translucent; this demonstrates the disruption of spherulite crystals under strain, which dissipates the applied strain energy and explains much of the tough behavior of the thiol-ene networks. When we examine Figure 26 in conjunction with the DSC data of Figure 22b and the $\tan\delta$ curves of Figure 24, the synergy of crystallinity and crosslinking in this system becomes apparent. While samples with low TMPTMP concentration (2.5 and 5 $t_{\text{mol}}\%$) are mechanically reinforced by their high crystallinity and transition temperatures near testing temperature (22°C), their low gel fraction and crosslink content results in a loose network with fewer covalent anchor points to resist chain motion and strengthen the polymer beyond the yield point. Materials with 7.5, 10, and 12.5 $t_{\text{mol}}\%$ crosslinker also have T_{gs} near 22°C and therefore benefit from maximum thermo-mechanical damping, but polymers with $\geq 12.5 t_{\text{mol}}\%$ TMPTMP have a fraction of the crystallinity present in less crosslinked materials, and therefore do not receive nearly the amount of mechanical reinforcement. Samples with more TMPTMP distribute applied loads more evenly between individual crystals throughout their network and require more covalent linkages be broken by a propagating crack tip, which are likely contributing reasons for the higher failure strains of HDT-TMPTMP-DVTU-12.5 through HDT-TMPTMP-20 compared to materials with less TMPTMP. Furthermore, samples

with 7.5% and 10% TMPTMP achieve the highest ultimate tensile stress resulting from the synergy of their physical and covalent crosslinking, and these elevated stresses likely contribute to network failure at smaller strains. At first, the notion that more crosslinking permits larger rather than smaller failure strains is a counterintuitive result, and one explanation could be that polymers' mechanical behavior is highly dependent on their testing temperature relative to their T_g .^[83, 129] For example, a polymer stretched at a temperature much higher than its T_g reaches higher failure strain but lower stress than the same polymer tested at or below T_g . Intermediately crosslinked HDT-TMPTMP-DVTU materials with 15-20 $t_{mol}\%$ crosslinker (which have significantly depressed T_g s as measured by DMA) would strain further by this effect. However, while more crosslinked samples reach higher strains, the additional strain cannot fully compensate for the loss of dissipative energy of the physical crosslinks. Thus, the increased crosslinking mutes the effects of spiroacetal presence in the polymer, and the greatly reduced crystallinity in these materials results in overall reduced toughness and strength. Both of the highly crosslinked materials, HDT-TMPTMP-DVTU-50 and TMPTMP-DVTU, have substantially poorer mechanical properties than all formulations except HDT-DVTU, which gives credence to the idea that a small amount of crosslinker compliments the properties of a polymer containing spiroacetal units along the backbone, while too much crosslinking negates these synergies. Plots of failure strain, yield and ultimate tensile strength, and failure strain versus TMPTMP concentration is

shown in Figure 27 to illustrate the effect of crosslinking on the performance of the material.

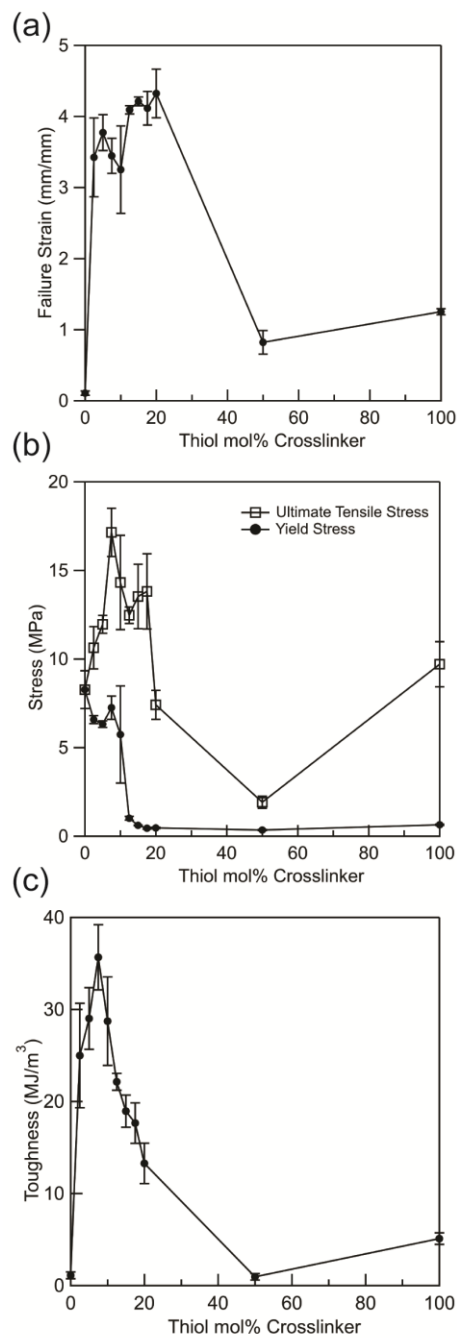


Figure 27: Several relationships between crosslinker content and mechanical properties. Samples were tested at 0, 2.5, 5, 7.5, 10, 12.5, 15, 17.5, 20, 50, and 100 t_{mol}% TMPTMP. A. Failure strain B. Ultimate tensile stress and yield stress C. Toughness.

The inset of Figure 26 shows several benchmark compositions of PDT-TMPTMP-DVTUs for comparison to those of HDT-TMPTMP-DVTUs. All samples tested were substantially less tough and achieved lower ultimate- and failure strengths than their HDT-TMPTMP-DVTU counterparts. Curiously, while PDT-DVTU mirrored the behavior of HDT-DVTU in breaking shortly after the initial yield peak, and both PDT- and HDT-TMPTMP-DVTU-20 follow classic thermoset stress-strain behavior, PDT- and HDT-TMPTMP-DVTU-7.5 differ quite dramatically. PDT-TMPTMP-DVTU-7.5 has a large strain to failure and a very low, flat stress response until high strain is reached. It does not contain the early yield peak or the large stresses at moderate-to-high strains present in HDT-TMPTMP-DVTU-7.5, which we attribute to the material's lack of crystallinity. The reduced stress on the network means fewer crosslinks are required to maintain network integrity and therefore more damage can be sustained, which results in higher strain prior to failure. In addition, extensive deformation outside of the dogbone gage length was observed for PDT-TMPTMP-DVTU-7.5, which inflates its failure strain as computed using grip displacement. A summary of the mechanical properties for PDT- and HDT-TMPTMP-DVTUs can be found in Table 8.

After determining HDT-TMPTMP-DVTU-7.5 to be the toughest thiol-ene, we assessed its stress-strain response using a non-contact video extensometer to better understand its behavior during deformation. As shown in Figure 28, the stress-strain curve can roughly be divided into three sections: early yield behavior, crystal dissipation

and chain untangling, and chain alignment to failure; these regions are labeled 1, 2, and 3, respectively. As shown in Figure 28a, the video extensometer emphasized regions 1 and 2 as compared to grip strain (strain computed using grip displacement divided by initial grip separation) because it only measures deformation inside the homogenous region of the dogbone. Grip strain, shown in Figure 28b, includes deformation both inside and outside of the gage length, and so underreports strain for samples with both high crystallinity and sufficient crosslinking (the case for samples with 7.5 and 10 t_{mol}% TMPTMP), and overreports strain for thiol-enes with insufficient crystallinity (≥ 12.5 t_{mol}% TMPTMP) or crosslinking (2.5 and 5 t_{mol}% TMPTMP) to prevent large deformation outside of the gage. The graph on Figure 28c depicts the ratio between video strain and grip strain; each region has a distinct relationship and it is clear that most deformation inside the gage length is completed by the end of region 2 (where video strain surpasses grip strain by as much as 225%). The video to grip strain ratio approaching unity throughout region 3 indicates that sample deformation occurs increasingly outside of the gage. The stress-strain curve of Figure 28a should be considered a more accurate representation of this material's deformation behavior, as it emphasizes the importance of crystallinity in increasing toughness during stretching. HDT-TMPTMP-DVTU-7.5 stress-strain data using the video extensometer may be found at the bottom of Table 8.

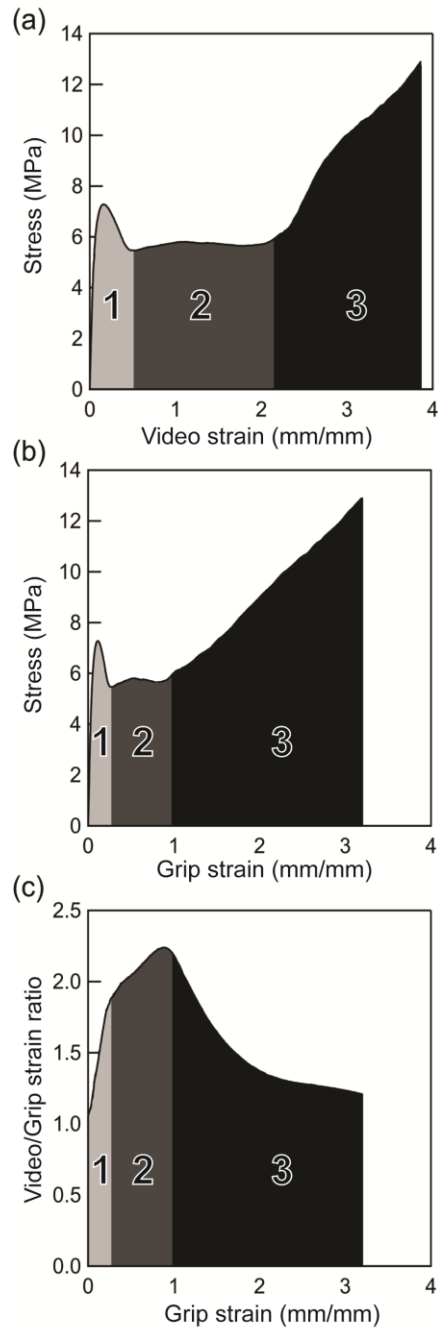


Figure 28: HDT-TMPTMP-DVTU-7.5 stress-strain behavior from video- and grip strain measurement techniques. A. Stress-video strain. B. Stress-grip strain. C. Video/grip strain ratio during tensile testing.

4.4 Conclusion

We synthesized a new system of thiol-ene photopolymers to contain spiroacetal alkene units periodically along the polymer backbones. The semicrystalline networks are some of the toughest thiol-ene photopolymers yet reported, and are the toughest of the subset to not include urethane linkages. Controlling the amount of crosslinking present in the samples provided a method to tune morphological and mechanical properties such as crystallinity and the stress-strain behavior of the polymers. We found that a lightly crosslinked network composed of 7.5 $t_{\text{mol}}\%$ TMPTMP resulted in a polymer capable of achieving $\sim 36 \text{ MJ/m}^3$ toughness. This material represents a unique, new photopolymer that derives its toughness at room temperature from a combination of crosslinking, crystallinity, spiroacetal chemistry, and the thermo-mechanical damping resulting from proximity to its glass transition temperature. More broadly, this work identifies spirocycles, molecules containing atom-sharing organic rings, as moieties that may be incorporated into traditionally weak polymers like thiol-enes to tune and improve their mechanical performance. We believe materials incorporating spirochemistry hold great promise for demanding applications such as load-bearing polymers and robust 3D printing resins.

Chapter 5. A Tough, Stable Spiroacetal Thiol-ene Resin for 3D Printing

The work of Chapter 4 successfully identified and optimized a thiol-ene platform that relies on spirochemical moieties for impressive thermomechanical properties. The final aim of this dissertation therefore builds off of this system, taking the optimal HDT-TMPTMP-DVTU-7.5 formulation (henceforth referred to as HTD7 for brevity) and furthering our understanding and control of the material in order to demonstrate its suitability as a robust, printable resin platform. To this end, the work of the penultimate chapter applies a heat treatment study to HTD7 to better understand how to best control and optimize its semicrystalline morphology, tweaks the formula to polymerize under visible light, and provides proof of concept that the thiol-ene resin can be printed using commercially-available DLP technology and provides mechanics on par with or exceeding many traditional printing materials such as (meth)acrylate resins, PLA, and ABS.

5.1 Introduction

Despite being understood for well over a century,^[79] thiol-ene polymerization has seen an explosion of industrial and academic interest in the previous two decades for a wide variety of applications, such as 3D printing,^[116, 134-136] shape memory materials,^[86] impact resistant materials and coatings,^[81, 98, 137] and biomedical implants such as dental restoratives and neurological probes.^[32, 84, 85, 87, 116] This expansion largely coincides with the development of “click-chemistry”, a reaction category that includes thiol-ene

polymerizations and was broadly categorized by Sharpless *et al* to describe reactions which have high yields, produce readily removable by-products, are stereoselective, and are easily conducted in the presence of little or mild solvent.^[80] The thiol-ene reaction proceeds in an anti-Markovnikov manner through either Michael addition, in which a carbon nucleophile is linked to an α,β -unsaturated carbonyl compound via 1,4-addition reactions, or free-radical addition, which progresses in a series of propagation and chain transfer steps (step growth), as well as chain growth by alkene homopolymerization for appropriate alkene chemistries such as (meth)acrylates.^[81] The present work proceeds only by step growth free-radical addition, and a generalized reaction is illustrated in Figure 29. Importantly, thiol-ene free-radical addition polymerization has several advantages over traditional radical reactions, including increased material homogeneity resulting from a delayed gel point, low shrinkage, and resistance to the radical quenching capability of molecular oxygen by generating a thiyl radical via chain transfer.^[81] These qualities make thiol-ene chemistry an excellent candidate for 3D printing applications, especially as the chemistry's biggest drawbacks (namely, odor and limited shelf-life) are addressable through appropriate choice of monomers and stabilizers.^[82, 138-140]

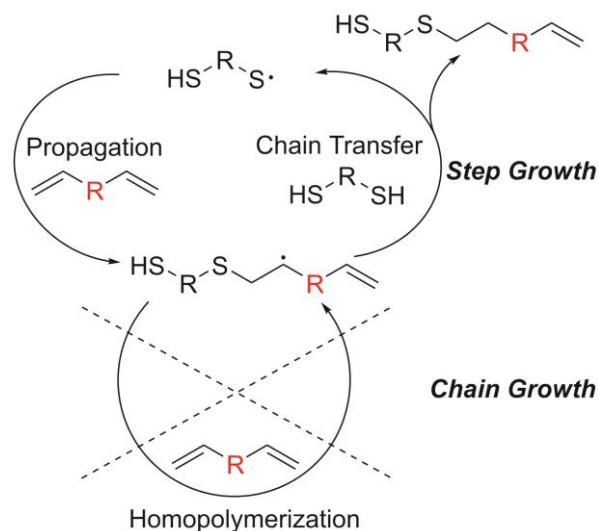


Figure 29: Ideal thiol-ene reaction proceeds only via step-growth to produce a tailored polymer backbone.

Invented in 1984,^[141] 3D printing has matured as a manufacturing choice and field of active research. Today, additive manufacturing is possible with every class of material and is increasingly used across fields as diverse as tissue engineering,^[142-144] prototyping,^[145, 146] microfluidics,^[91, 92] medical and dental engineering,^[147-149] aerospace and automotive design,^[145, 150] and electronics.^[151, 152] Early iterations of 3D printing suffered from poor mechanical properties as a result of limited material libraries and interlayer adhesion issues, but recent years have seen these problems addressed through an increasing diversity of suitable materials and improvements to the layer-by-layer technique that underlies all 3D printing.^[153] Of particular interest here is the recent improvement in printable polymers, whose properties can be tailored to suit their intended application by tuning crosslink density and molecular weight and incorporating energy dissipation mechanisms such as interchain hydrogen bonding,

aqueous ionic bonds in hydrogels, semi-crystallinity, sliding crosslinks, interpenetrating polymer networks, and the addition of filler material. Further, many polymers such as tough polycarbonate urethane thermoplastics,^[154, 155] self-healing polymers and composites,^[156-158] and high-strain semi-crystalline polymers^[159] also benefit from heat treatment during or post-printing to control phase-separation, increase or activate new polymerization, and tune morphology, thereby improving their mechanical profile.

We previously found the spiroacetal polymer described herein, HTD7, crystallizes at ambient temperature, reaches equilibrium crystallinity within 3 days at 22 °C, and presents dual-melting behavior indicative of a bimodal crystallite size distribution.^[121, 123, 160] Additionally, it possesses extraordinary tensile properties for a thiol-ene photopolymer, which is attributable to its semi-crystallinity and spirochemistry. Spiro compounds contain adjacent chemical rings that share one atom, giving the moieties a three-dimensional, twisted conformation that is responsible for many unique properties. Their homopolymers are characterized by high rigidity, temperature resistance, and crystallinity,^[108, 161, 162] qualities which simultaneously make the materials hard to process with traditional heat- or solvent-based processing techniques and give them excellent thermo-mechanical properties as fiber-forming and load-bearing polymers.^[40, 163, 164] Frequently found in natural compounds derived from plants, amphibians, and marine sponges,^[165, 166] they have medicinal applications as diuretics,^[167] anti-fungals,^[168] and anti-tumor compounds.^[165, 169, 170] Yet while spirocyclic small molecules draw more

investigation, intentional study of their effects in polymers has been more limited, with a few reports describing spiroacetal polymers used for drug delivery,^[43, 112] stimuli responsivity,^[110, 113] and hydrogels.^[111]

This work systematically investigates the resin stability, photokinetics, and effect of various heat treatments on the thermomechanical behavior of a semicrystalline, spiroacetal-containing thiol-ene polymer network. The most effective annealing regimen is applied to samples 3D printed from the stable thiol-ene resin formula to improve its tensile properties. 3D printing did not appreciably alter the morphology of HTD7 but did reduce its tensile performance, which we attribute to diminished interlayer adhesion in printed samples as compared to cast ones. This research provides a fundamental understanding of the structure and properties of these polymers, and demonstrates the potential of spirochemistry to improve the traditionally poor mechanical properties of printed parts and expand the available set of high-performance printable materials.

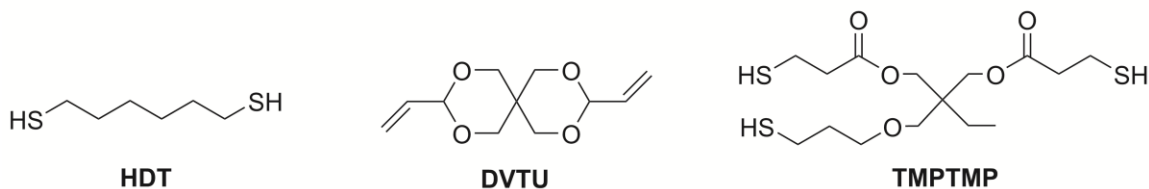
5.2 Experimental Details

5.2.1 Materials

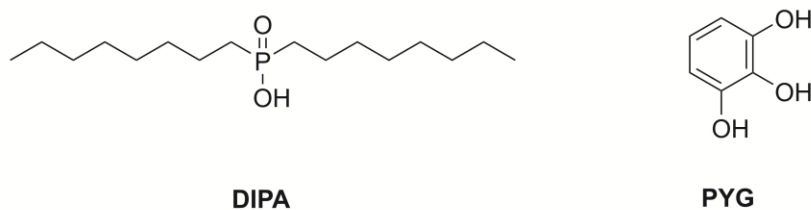
≥96 % 1,6-Hexanedithiol (HDT), ≥95 % Trimethylolpropane tris(3-mercaptopropionate) (TMPTMP), 2,2-Dimethoxy-2-phenyl-acetophenone (DMPA), 97 % Diphenyl(2,4,6-trimethylbenzoyl)phosphine oxide (BAPO), ≥98 % 3,9-Divinyl-2,4,8,10-tetraoxaspiro[5.5]undecane, ≥99% Pyrogallol (PYG), and ~90% Diisooctylphosphinic acid (DIPA) were obtained from Sigma Aldrich and used as received. We added DMPA or

BAPO to the resins as UV-Vis photoinitiators at a 0.5 wt % concentration to achieve smooth, repeatable photopolymerization profiles. PYG and DIPA stabilizers were used at 9mM and 90mM concentrations, respectively. The structures of all materials used in this study are shown in Figure 30.

Monomers



Co-stabilizers



Photoinitiators

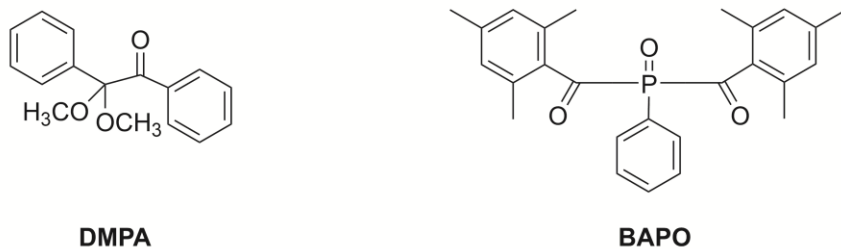


Figure 30: Materials used in this investigation.

5.2.2 Polymer Synthesis

We made all thiol-ene resins according to a previously described protocol.^[160] Each resin contained a stoichiometric balance of thiol and vinyl functional groups in the monomer mixture, while also holding crosslinker (TMPTMP) concentration constant such that 7.5% of all thiol functional groups belong to TMPTMP. After mixing all monomers together in a clean glass vial, we warmed the mixture to 75 °C to expedite the mixing of crystalline DVTU monomers with the liquid thiols. When appropriate, we then added photoinitiator and stabilizer molecules, followed by additional warming, 60 seconds of vortexing, and 10 minutes of sonication to remove dissolved gasses from the resin. Samples for the heat treatment investigation were cast as ASTM D638 Type V dogbones between clean glass slides separated by 1 mm rubber spacer dogbones and contained DMPA photoinitiator to match the 365 nm light of the UVL UL-1000 ultraviolet chamber. All cast samples were irradiated for 60 minutes to achieve full polymerization. In lieu of DMPA, photo-DSC and 3D printing samples contained BAPO photoinitiator, whose absorption profile extends appreciably into the visible spectrum and to match the light output from the DLP projector described in the 3D Printing section.

5.2.3 DSC and Photo-DSC

DSC data was acquired with a TA Instruments Discovery DSC. Polymer discs weighing approximately 8 mg were pressed into aluminum pans and subjected to a

heating ramp from -50 °C and 120 °C at 10 °C min⁻¹ under nitrogen gas. T_g was calculated as the midpoint between onset and endset temperatures, themselves taken to be the intersection temperatures between lines tangent to the steady state and transition slopes of the heat flow versus temperature plots. Fusion endotherm temperatures were recorded to be either the temperature at which heat flow was locally minimized. When a true local minimum was not present, the temperature was taken as the intersection between tangent lines of the heat flow curve immediately preceding and following the transition region. Mass-normalized enthalpy of fusion was taken to be the integral of the melting peaks against their steady state heat flow baselines.

The working environment of the printer was emulated by positioning a Vivitek D912HD DLP projector above the DSC cell at working distance and illuminating the cell at the lowest brightness setting with white light; this produced a light intensity of 17-18 mW cm⁻². Resin samples of 5-15 mg were placed in open-face aluminum pans and exposed to the light at 22 °C for the photopolymerization curves; each cured sample was then re-exposed to light for the same period of time to establish a baseline heat flow. Experiments were conducted at 22 °C with the cell covered by a transparent quartz window to modulate nitrogen flow and permit visible and near UV light transmittance.

5.2.4 Rheology

Resin viscosity was determined using an ARES-G2 rotational rheometer 25 mm and cone-and plate system in which 75 µl of material was sheared at a shear rate of 300

s⁻¹ with a truncation gap of 49 μm at 22 °C. Samples were held in sealed glass jars in a dark, room-temperature environment at all times prior to testing. Deionized water (literature viscosity of 0.9544 mPa at 22°C) was obtained from a MilliporeSigma MilliQ water filtration system and used as an external standard to correct any systemic errors in the rheometer.

5.2.5 Stress-Strain Behavior

The stress-strain response of ASTM D638 Type V dogbones was investigated with a TestResources QController tensile test frame outfitted with a 440N load cell. Strain was measured using an Imetrum video extensometer and software package to track the separation of opaque markers inside the dogbone gage as samples were stretched at a rate of 10 mm min⁻¹. All samples were equilibrated to the ambient temperature of 22 °C prior to being pulled in tension to failure. Tensile toughness was calculated as the integral of the stress-strain curve, and is reported as volumetric energy dissipation with units of J m⁻³. Yield strength was taken as the early local maximum in the stress-strain curve, and the yield strength of samples without such local maximum was taken to be the stress at the yield strain obtained by extrapolating the yield strain versus annealing temperature curve from samples which did have a directly observable yield point.

5.2.6 3D Printing

We built a custom 3D printer in a top-down orientation using a Vivitek D912HD DLP projector as the light source and a Thorlabs 150mm Linear Translation Stage to control printed layer height. We printed custom resin vats and stage arms using a Carbon3D CLIP printer with PR25 prototyping resin and a UltiMaker with polyvinyl alcohol filament according to their prescribed protocols. A custom MATLAB script, adapted from Thorlabs, controlled the projector and translation stage in concert to cure the resin one cross-section at a time. Printing parameters default to the following, unless otherwise noted: layer thickness = 100 μm ; layer exposure time = 20 s; layer overshoot = 2mm; resin equilibration delay = 10 s.

5.3 Results and Discussion

5.3.1 Resin Stability

Thiol-ene resins have widely varying shelf-life stability, from under a few hours to several months.^[82] In addition to dependence on the structure of the –ene moiety, resin shelf-life can be reduced by dark reactions such as thiol to –ene Michael addition, impurities or peroxides generating radical species to induce polymerization, and ground-state charge transfer complexes formed between thiol and –ene groups.^[82, 140, 171, 172] Many groups have studied the efficacy of hydrogen-donating phenolic radical scavengers in combination with neutralizing or acidic co-stabilizers to prevent premature polymerization, with some of the most effective results obtained by Edler *et*

al using a combination of 9 mM Pyrogallol and 90mM Diisooctylphosphinic acid.^[140] They found this combination effectively prevented premature dark polymerizations without suppressing photopolymerization. In polymerizations proceeding via radical propagation, it is important that the radical scavenging species is only present at the minimally effective concentration to avoid suppression of chain growth during polymerization. An additional consideration is that the acidic conditions enhanced by DIPA co-stabilizer have the potential to hydrolyze acetal linkages of the spiroacetal units. We found that 90 mM of DIPA did not alter the pH of the base resin from approximately 4.5, which has been shown to not degrade the molecule over long time periods.^[108] The acid-stability of DVTU is consistent with previous literature reports that cyclic acetals have small, negative entropies of hydrolysis that reduce their degradation rate up to 35 times slower than acyclic acetals.^[173, 174] For these reasons, we investigated the ability of 90mM DIPA and 9 mM PYG co-stabilizers to maintain a low resin viscosity under dark conditions over long storage times.

As shown in Table 1, we found no significant difference between the changes in viscosity of resins containing inhibitors PYG and DIPA and those without. We found that all formulations experienced less than a 10% increase in viscosity after two months at 22 °C and retained their fluidity. We tested samples with both DMPA AND BAPO photoinitiators and found that while BAPO resulted in a slightly more viscous resin, it remained sufficiently fluid for printing purposes. The addition of stabilizers did not

have a meaningful impact on the immediate thiol-ene viscosity nor viscosity up to 2 months of storage. Though longer time points may elucidate a more pronounced benefit from the incorporation of stabilizers, our results indicate that the naturally mild acidic conditions of the resin, in addition to the absence of –ene homopolymerization of DVTU, make this thiol-ene formulation naturally stable under dark, room temperature storage conditions.

Table 1: Resin viscosity over time shows stability with both photoinitiators

Resin Contents	0 Days (mPa)	5 Days (mPa·s)	10 Days (mPa·s)	15 Days (mPa·s)	20 Days (mPa·s)	30 Days (mPa·s)	45 Days (mPa·s)	60 Days (mPa·s)
0.5 wt% DMPA	8.62 ± 0.12	8.31 ± 0.25	8.98 ± 0.08	8.83 ± 0.15	9.03 ± 0.16	10.23 ± 0.28	8.77 ± 0.44	9.23 ± 0.55
0.5 wt% BAPO	9.68 ± 0.30	10.20 ± 0.07	9.88 ± 0.58	9.07 ± 0.40	10.59 ± 0.51	9.45 ± 0.97	11.04 ± 1.22	9.72 ± 1.49
0.5 wt% BAPO 9 mM PYG 90mM DIPA	9.20 ± 0.30	9.77 ± 0.42	8.90 ± 0.51	9.91 ± 0.27	9.77 ± 0.42	8.07 ± 0.30	8.44 ± 0.23	8.72 ± 0.13

5.3.2 Kinetics of Photopolymerization

Because most DLP and stereolithography 3D printers operate using light in the visible and near-UV spectrum, resins must incorporate photoinitiators with appropriate absorption profiles to initiate polymerization at in an efficient manner. Photoinitiators are generally found in commercial resins at concentrations ranging from 0.1-3 wt% to sustain a critical radical population for initiation while avoiding problems associated with excess radicals such as polymer aging, side reactions, and overly fast and

uncontrollable polymerization kinetics.^[175] The rate of initiation, R_i , is equivalent to the change in initiator species over time according to the following relationship:^[176]

$$R_i = -\frac{d[I]}{dt} = \ln(10) f \varepsilon [I] I_0 d \quad (5.3.2.1)$$

Here, $[I]$ is the concentration of photoinitiator, I_0 is incident light intensity (power per volume), ε is the initiator molar absorptivity coefficient, f is the radical generation efficiency of the initiator, and d is the curing film thickness. In applications like 3D printing, initiator concentration is low and layers are thin (approximately 100 μm); this allows Equation 5.3.2.1 to be rewritten as essentially independent of cure depth for the thin layers as:^[177, 178]

$$R_i = -\frac{d[I]}{dt} = \frac{\ln(10) f \varepsilon [I] I_0' \lambda}{N_A h c} \quad (5.3.2.2)$$

Equation 5.3.2.2 allows the rate of initiation to be expressed in terms of more accessible variables like Avogadro's number (N_A), Planck's constant (h), the speed of light (c), and incident light intensity in power per area (I_0'). While these equations are useful for fundamental understanding of photocurable resins, it is difficult to obtain and use accurate values of f and ε when incident light occurs across a spectrum of wavelengths instead of monochromatically. Thus, it is often more instructive to report key metrics such as maximum heat flow (h), exposure time required to reach maximum heat flow (t_{max}), and total enthalpy of polymerization (ΔH) to summarize the photopolymerization kinetics of a resin.^[138, 140] These parameters directly correlate to several controllable variables that are important to successful DLP printing. In

particular, a higher value of h indicates more drastic heat gradients throughout the resin as the monomers release energy during polymerization; if constrained, the corresponding rise in local temperature can cause internal stresses due to thermal expansion and contraction. Other important considerations include layer exposure time, which is influenced by the speed of reaction, t_{\max} , and the need to achieve a high extent of polymerization (fraction of total ΔH)^[179] for each layer to maintain its shape while simultaneously leaving enough unreacted functional groups on the surface to bond to the following layer and create strong interlayer adhesion.

Though previous reports have shown that thiol-ene reactions may proceed without photoinitiator under appropriate conditions,^[81, 180, 181] the DLP projector used in this study was incapable of producing sufficiently high energy (*i.e.* short wavelength) UV light to induce polymerization in initiator-free resin mixtures. This is evidenced by the flat curve corresponding to the heat flow behavior of the initiator-free resin shown in the inset of Figure 31b. We found that illuminating this resin for as long as 30 minutes produced heat flow curves that were indistinguishable from their respective baselines. Incorporating DMPA at 0.5 wt% enabled us to fully polymerize the thiol-ene while maintaining a modest heat flow of less than 2.5 Wg^{-1} . However, because the efficiency of DMPA decreases dramatically in the near UV-Vis wavelengths, t_{\max} was over 215 seconds and the corresponding FWHM of the heat flow versus time curves was approximately 3 minutes. To address this, we replaced DMPA with 0.5 wt% BAPO, a

photoinitiator with an absorbance profile that extends to wavelengths in the mid-400s of nanometers. The resulting resins had a much shorter t_{\max} of 11.1 seconds and FWHM of 9.3 seconds. These values are much more amenable to 3D printing and avoid the potential issue of overly long print times for objects taller than a few millimeters.

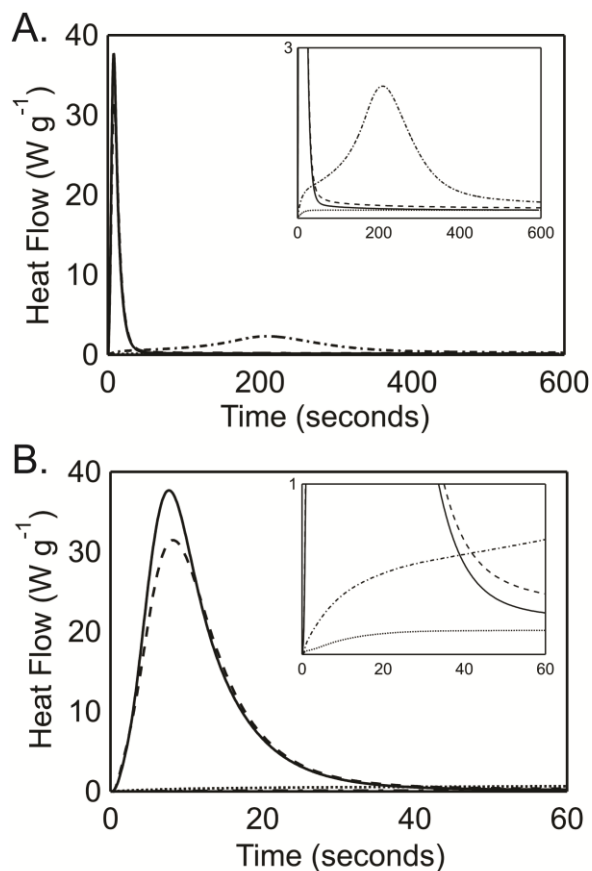


Figure 31: Heat flow of resins under light from DLP positioned above DSC cell at operating distance. A. 10 min exposure. B. 1 min exposure. Solid: BAPO photoinitiator. Dashed: BAPO photoinitiator, 9 mM PYG, 90 mM DIPA. Dash-dots: DMPA photoinitiator. Dots: No photoinitiator.

We also examined the effect of co-stabilizers PYG and DIPA on the kinetics of HTD7 photopolymerization. With respect to the non-stabilized formulas, resins with

PYG and DIPA showed little change in their ΔH , t_{\max} , and FWHM. The modest damping of maximum heat flow in the stabilized resins may be attributed to the hydrogen-donating PYG species, which acts to quench radicals and competes with the ongoing polymerization. PYG neutralizes radicals in proportion to their concentration and therefore is most effective early in photopolymerization. Ultimately, its ability to scavenge radicals is exhausted, and the polymerization proceeds in a manner similar to stabilized thiol-ene formulations reported in the literature.^[138, 140] Although reducing maximum heat flow is beneficial, the only heat-generating mechanisms are the thiol-ene radical transfer and the cleavage of photoinitiator molecules, and therefore the reduction of ΔH that also accompanies the presence of PYG and DIPA likely indicates that fewer thiol-ene bonds are formed and a less cohesive network is created. Thus, the resin formula we chose for mechanical testing and 3D printing was free of stabilizers and contained 0.5 wt% BAPO photoinitiator. Representative heat flow curves are illustrated in Figure 31, and the values of t_{\max} , h , FWHM, and ΔH are given in Table 2.

Table 2: Photo-DSC parameters for various resin formulations exposed to DLP projector above DSC cell at working distance.

Photoinitiator	PYG (mM)	DIPA (mM)	t_{\max} (seconds)	h (mW mg ⁻¹)	FWHM (seconds)	ΔH (J g ⁻¹)
-	-	-	-	0.16 ± 0.01	-	-
0.5 wt% DMPA	-	-	216.97 ± 20.32	2.19 ± 0.16	182.60 ± 9.36	410.64 ± 4.70
0.5 wt% BAPO	-	-	11.1 ± 3.33	37.83 ± 4.21	9.26 ± 1.41	435.22 ± 2.53
0.5 wt% BAPO	9	90	9.97 ± 1.00	28.91 ± 3.22	11.69 ± 1.88	403.18 ± 4.53

5.3.3 Heat Treatment

In a previous publication, we reported HTD7 as having a spherulitic microstructure that anneals passively at room temperature and exhibits dual endotherm behavior.^[160] Though there a wide variety of underlying causes giving rise to multiple melting endotherms in polymers, the most common explanations are multiple crystallite sizes,^[182] multiple crystal structures,^[183, 184] as well as melting and re-crystallization of crystalline regions in the polymer.^[185, 186] Our prior research found the cause of HTD7 dual endotherms to be multiple crystal sizes, which was supported by the tunability of the lower temperature endotherm and the independence of the melting temperatures on heating speed during DSC scans. Because of this, we performed a comprehensive heat treatment study by annealing samples at temperatures ranging from -20 °C to 60 °C for periods as long as 3 weeks in duration to tune its morphology and understand the structure-property relationships of the semicrystalline thiol-ene.

5.3.3.1 Thermal Behavior

Figure 32 illustrates the thermal behavior of HTD7 via DSC heating scans from -40 °C to 120 °C. Shown in Figure 32a, samples that were quenched from the postcure temperature of 85 °C and held below the glass transition temperature, T_g , underwent no appreciable crystallization through all time points. This agrees with the consensus understanding that temperatures below T_g do not provide enough thermal energy for chain relaxation and rearrangement into their lowest energy, crystalline

configuration.^[187] The glass transition region of the samples held at -20 °C did not noticeably change in position or breadth with increasing exposure times, which stands in contrast to all samples annealed at temperatures higher than T_g . Samples held at -20 °C displayed melting endotherms around 34 and 68 °C; both are slightly lower in temperature and significantly smaller than those of HTD7 annealed at 22 °C. We attribute their diminutive size and presence to a small amount of crystallization that occurs both during the quenching process from 85 °C to -20 °C in air, as well as the minutes the sample spends at temperatures above its T_g of approximately -3 °C during DSC heating scans. The larger size of the upper temperature endotherm in the non-annealed samples is consistent with primary/secondary crystallization theory, which states that larger grain boundaries in polymers cooling from melt state form first and are followed by smaller crystal formation via secondary crystallization.^[188] Larger crystals are known to have a higher melting temperature, which was quantified by Xue *et al* in the following relationship:^[128]

$$\Delta T = T_0 - T = \frac{2T_0\sigma V_m}{\Delta_s^l H_m r} \quad (5.3.3.1.1)$$

in which T_0 and T are the melting point of theoretical bulk crystal and the melting point of a crystal with radius r , respectively, and σ , V_m and $\Delta_s^l H_m$ are the surface tension, molar volume, and molar heat of fusion of r -radius crystals, respectively.

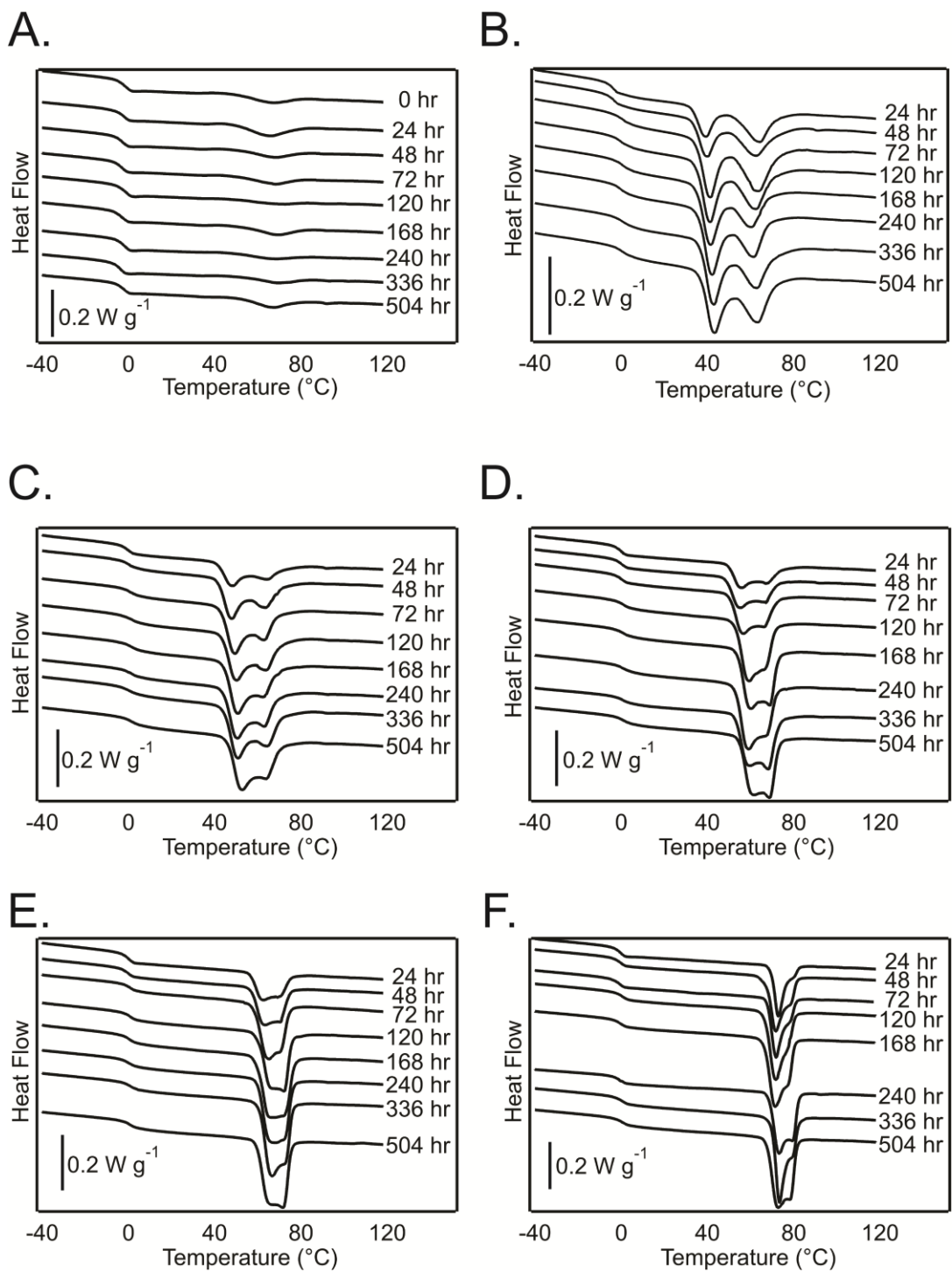


Figure 32: DSC heating curves at various annealing temperatures over time. A. -20°C anneal. B. 22°C anneal. C. 30°C anneal. D. 40°C anneal. E. 50°C anneal. F. 60°C anneal.

Figure 32b-f demonstrates that all temperatures between 22 °C and 60 °C cause HTD7 to increase in crystallinity, as evidenced by the rising and broadening of their glass transition regions (a result of the random physical crosslinks crystallites create) and the deepening of their melting endotherms to a maximum fusion enthalpy of approximately 20.5-21.5 J g⁻¹. However, the precise thermal behavior of the material depends heavily on the annealing temperature. We found that two distinct local minima were generally found between 40 and 80 °C, with both rising in temperature at higher annealing temperatures and longer annealing times. This phenomenon conforms to reports of crystals formed at higher temperatures melt at correspondingly higher temperatures of approximately 5-25 °C above the annealing temperature.^[121, 122, 125, 126]

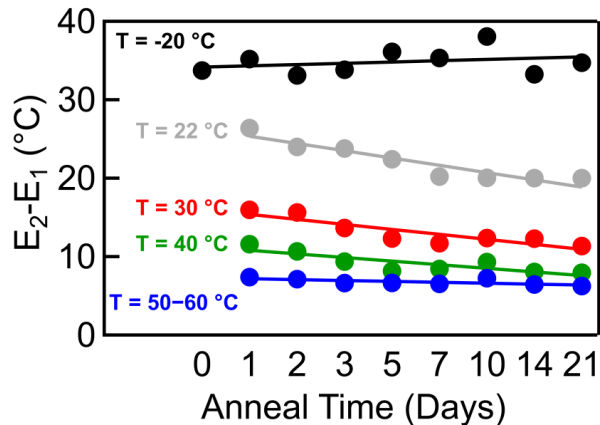


Figure 33: Temperature difference between low- and high-temperature melting endotherms as a function of annealing temperature over time.

We also found the temperature difference between the two endotherms decreased with both increasing annealing temperature and time. Figure 33 plots the temperature difference between the lower- and upper-endotherm temperatures (E_1 and

E_2 , respectively) for the various heat treatments. We interpret the trend of decreasing temperature difference between endotherms in the context of crystallite size and growth. Specifically, higher annealing temperatures increase the minimum nucleating size of a crystallite and have a larger effect on increasing the melting temperatures of the small lamella responsible for E_1 than they do on the larger, primary crystals. For example, we found that raising the annealing temperature from 22 °C to 40 °C increased the melting temperature of E_1 almost exactly 18 °C. In contrast, E_2 only rose by a modest 5.5 °C across the same annealing temperature increase, which agrees with the intuition that primary crystal size is predominantly established during cooling from the melt state. We found the exception to this rule was between 50 °C and 60 °C groups, due to 60 °C being so near the melt temperature that E_2 and E_1 were difficult to distinguish. Because DSC scans of samples annealed at 50 °C and 60 °C did not always have a true local minimum for E_2 , and in these cases we computed E_2 as the intersection of tangent lines drawn immediately before and after the “shoulder” of the thermal curve. Samples at 60 °C were also the only group of annealed samples that did not achieve fusion enthalpy greater than 20 J g⁻¹, instead reaching only 18.5 J g⁻¹ through the three week experimental endpoint. We hypothesize that the 60 °C sample group would have reached similar melting enthalpy with additional time, but the slower kinetics of crystallization at such a high temperature prevented it from doing so in our experimental window. Values for T_g

breadth, E_1 , E_2 , and enthalpy of fusion for each annealing temperature group are plotted in Figure 48 through Figure 53, with tabulated data located in Table 10 through Table 15.

5.3.3.2 Mechanical Behavior

Figure 34 contains representative monotonic tensile curves from HTD7 dogbones annealed at the previously described time-temperature combinations. Generally speaking, the dogbones that were stored below their T_g achieved higher failure strains but lower failure stresses than their annealed counterparts, which is consistent with the mechanical effects of increasing crystallinity in semi-crystalline polymers.^[129] The $-20\text{ }^\circ\text{C}$ stress-strain curves in Figure 34a consistently remain at low stress through 300% strain, and lack the crystalline alignment and dissipation region that is present in all annealed samples at intermediate strains between the yield point and the onset of coil stretching. Without crystalline reinforcement in the bulk, these samples suffer from a greatly reduced ability to bear load at moderate elongations, and so are considerably less tough than heat-treated samples of identical chemistry. In accordance with the DSC results that indicated no detectable morphology change with time, the $-20\text{ }^\circ\text{C}$ sample group also did not show any consistent trends in their mechanical properties such as toughness, yield stress, failure stress, or failure strain as a function of time through three weeks.

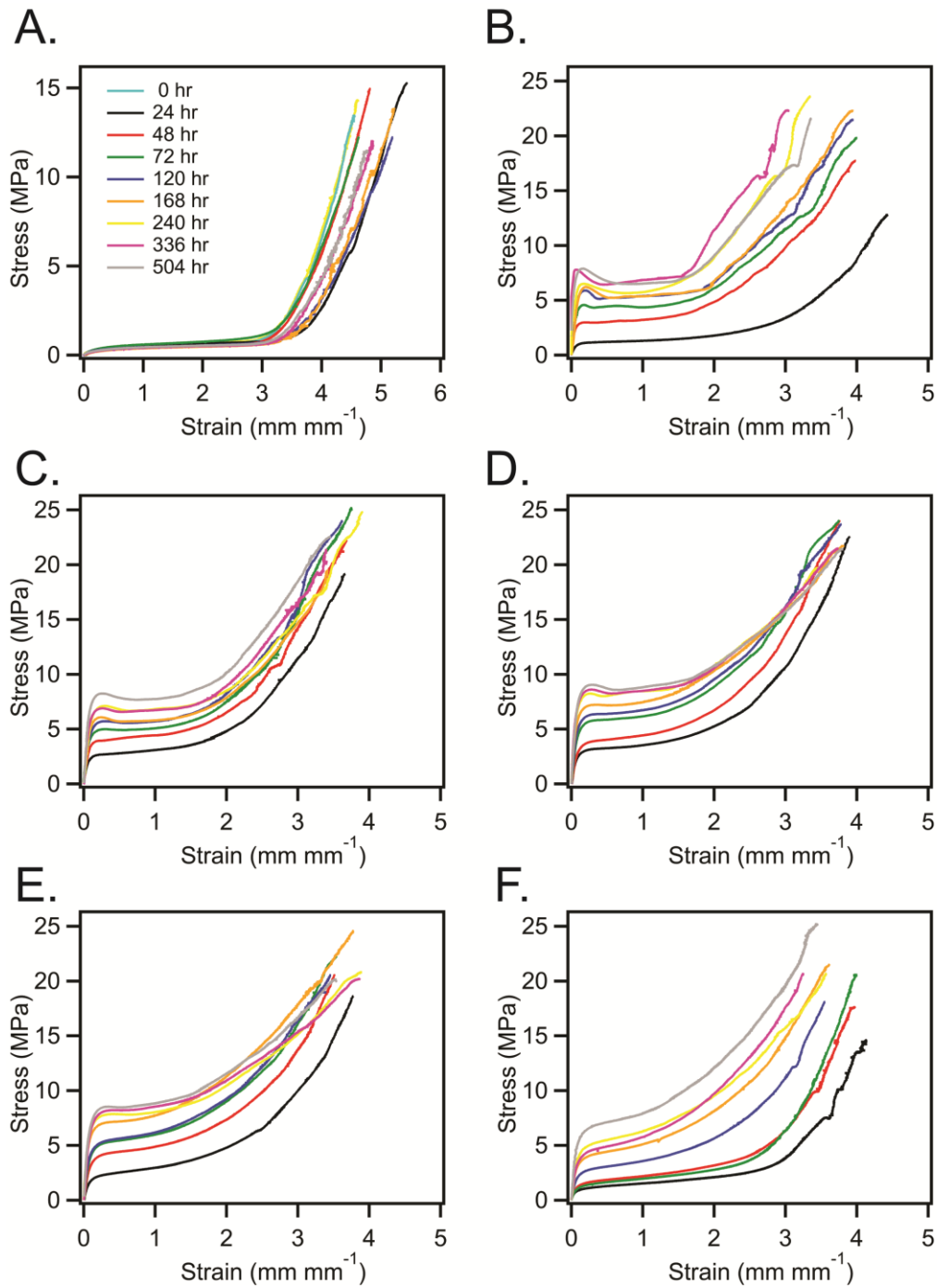


Figure 34: Effect of heat treatment at various temperatures on the mechanical behavior of cast dogbones made from base composition. A. -20 °C exposure. B. 22 °C anneal. C. 30 °C anneal. D. 40 °C anneal. E. 50 °C anneal. F. 60 °C anneal.

As depicted in Figure 34b-f, annealing at every temperature above T_g consistently resulted in yield stress, toughness, and failure stress increasing over time, while failure strain decreased with additional annealing; all of these behaviors are consistent with previous reports discussing the relationship of semi-crystalline polymer mechanical properties and crystalline content.^[129, 131, 132, 189-191] In addition, we found that the upper-to-lower yield difference (UY-LY), defined as the stress difference between the local maximum of the yield point and the lowest recorded stress at strains beyond the yield point, generally increased over time for all temperatures in which it was present, but was smaller or nonexistent in thiol-ene samples annealed at higher temperatures. We also found the appearance of UY-LY required longer annealing times at higher temperatures. Tough materials ideally have high yield strength, which indicates large resistance to plastic deformation, as well as a small UY-LY, which is the case for materials that continue to dissipate and absorb substantial deformation energy after the yield point.^[133]

Figure 35a-c plots UY-LY against annealing time, enthalpy of fusion, and E_2-E_1 , respectively, for all annealing temperatures and times in which it was present. We show in Figure 35a Figure 35c that UY-LY generally grows with time and is larger in the polymers that were annealed at lower temperatures. Further, Figure 35b illustrates that UY-LY was only consistently present in HTD7 samples having a total enthalpy of fusion exceeding 18 J g^{-1} . However, we found no correlation between enthalpy and UY-LY in

the polymers meeting this crystallinity threshold. Thus, as E_1 approaches E_2 in temperature and they begin to meld into a single continuous endotherm, their corresponding UY-LY decreases. This relationship between these two phenomena shows that the loss of strength immediately following the yield point can be mitigated by annealing the secondary crystallites larger to impose a more homogenous crystallite size distribution throughout the bulk of the polymer. In contrast to UY-LY, absolute yield strength of all annealed HDT7 samples correlates highly with total enthalpy of fusion in a power law relationship (Figure 35d). The fit curve predicts a theoretical yield stress of 0.19 MPa in completely amorphous polymer and has an adjusted coefficient of determination, R^2 , of 0.83 to the experimental data.

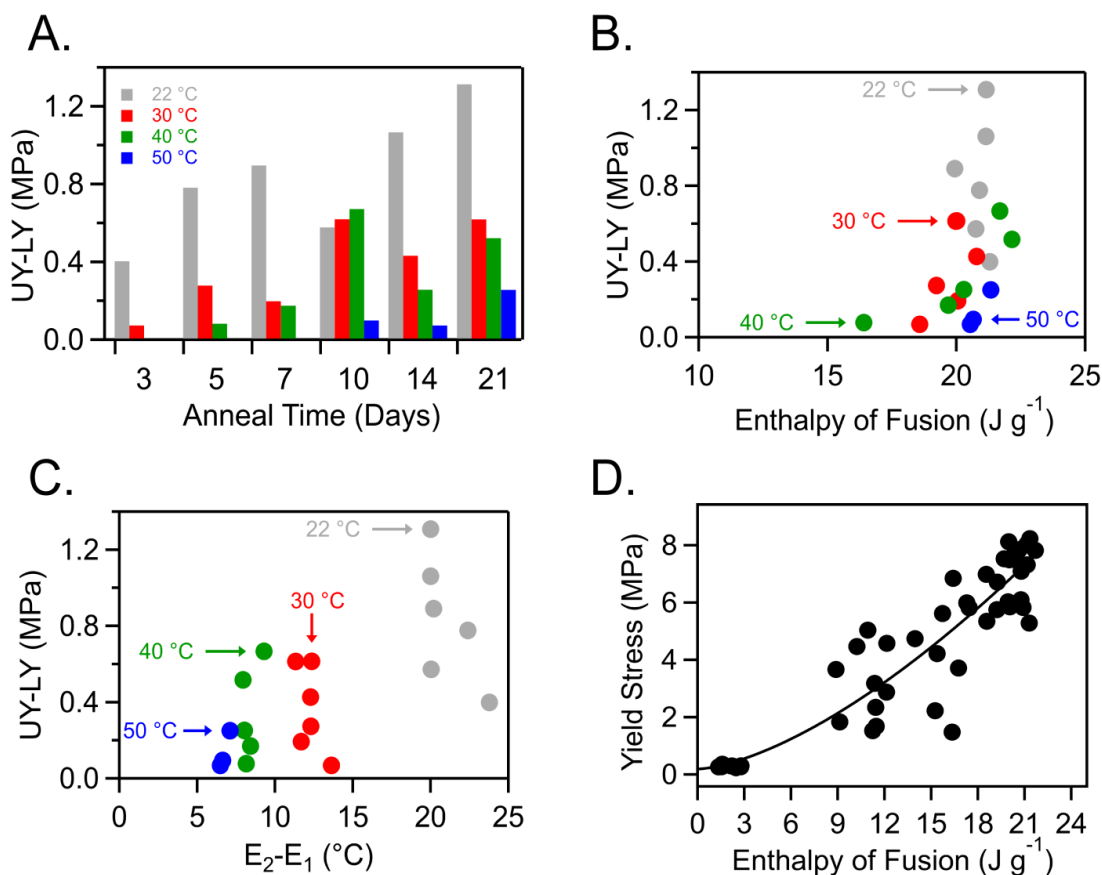


Figure 35: Yield behavior HTD7. A. UY-LY vs annealing duration. B. UY-LY vs enthalpy of fusion. C. UY-LY vs $E_2 - E_1$. D. Yield stress vs enthalpy of fusion.

By maintaining a constant chemistry, we isolate the relationship between degree of crystallinity in HTD7 and tensile properties of the thiol-ene. Figure 36a-c depicts yield stress, toughness, and failure strain versus annealing time, respectively. It is well known that crystalline regions in semi-crystalline polymers grow in a manner described by the JMAK (Avrami) equation:

$$V_{cf} = 1 - \exp(-K * t^n) \quad (5.3.3.2.1)$$

in which the crystalline volume fraction, V_{cf} , grows as a function material constants K and n over time t .^[192-194] Previous reports have reported have indicated that crystallization occurs more slowly at temperatures just below the T_m as well as just above T_g .^[195, 196] This is because high temperatures require a larger critical nucleating particle size to survive increased high thermal agitation of the polymer chains and low temperatures reduce chain rearrangement into lower free energy configurations (*i.e.* crystalline morphology) by providing less thermal energy. The plots of Figure 34 indeed follow this trend; the tight clustering of successive tensile curves in the 30 °C and 40 °C groups indicates that this temperature range is ideal for annealing HTD7 material to equilibrium most efficiently. Despite this qualitative trend, we did not observe sizable, consistent differences in the yield strength or toughness of samples annealed at temperatures between 22 °C and 50 °C, and therefore grouped them together for the presentation and analysis of Figure 36a and Figure 36b. Similarly, we found little difference in the failure strains of the annealed groups and therefore present their averages in data of Figure 36c to emphasize the general effect of any annealing. In this spirit, we fit the yield and toughness data of the annealed samples in Figure 36a and Figure 36b to a modified Avrami equation:

$$P = a * [1 - b * \exp(-K * t)] \quad (5.3.3.2.2)$$

with P corresponding to the property of interest (yield or toughness), a representing the maximum average value of that property, K conserved from the previous equation, b

acting as a fit-optimization parameter, and by setting n in Equation 5.3.3.2.1 equal to 1, which describes materials heterogeneously crystallized perpendicular to a nucleating surface such as the glass slides used in casting the dogbones. By doing so, we obtained good fits to the experimental data, with adjusted R^2 values of 0.86 and 0.89 for the 22-50 °C and 60 °C toughness data, respectively, and values of 0.96 and 0.94 to their corresponding yield strength averages. In light of this result, we posit that modified Avrami equations such as Equation 5.3.3.2.2 are powerful and useful tools for predicting not only crystallization kinetics, but several of their time- and heat-dependent mechanical properties as well.

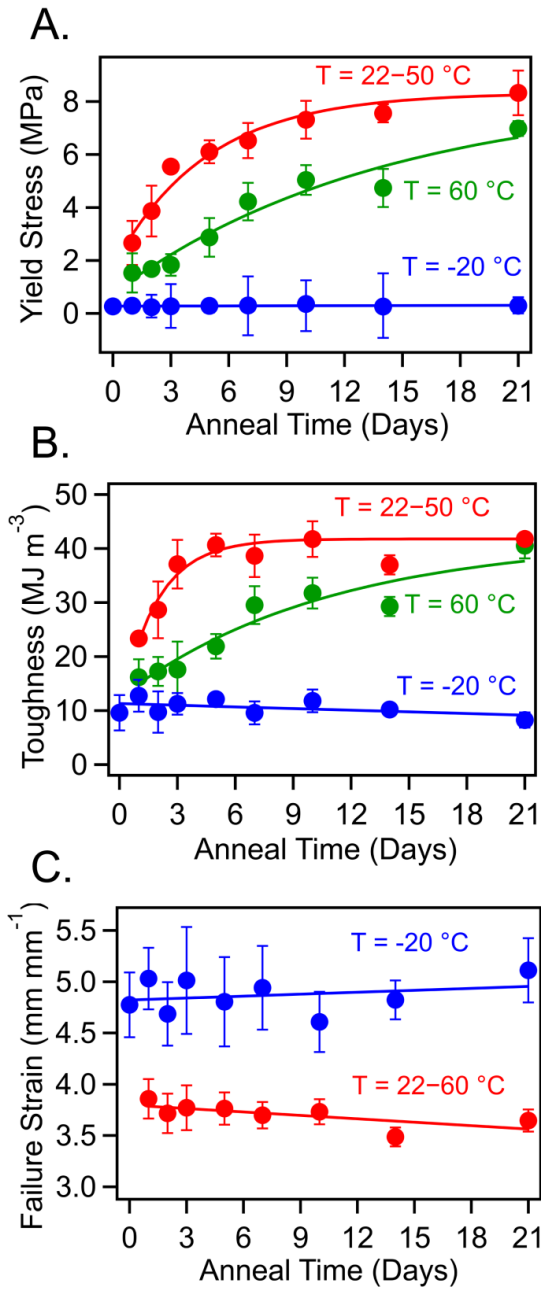


Figure 36: Mechanical behavior of HTD7 through 21 days of annealing. A. Yield stress. B. Tensile toughness. C. Failure strain. Yield and Toughness data for 22-60 °C groups are fit to a modified Avrami relationship. Linear fit curves for -20 °C samples are not intended as prescriptive and instead are included for visual clarity.

After examining the mechanical behavior of Figure 36, in conjunction with the time-temperature combination data of Table 16 through Table 21, we determined that intermediate temperature annealing beyond 120 hours continued to raise yield stress and reduce failure strain, but did not further affect average tensile toughness. We therefore identified 120 hours at 40 °C as a heat treatment regimen that provides ideal mechanical properties, and investigated its effect on DLP-printed dogbones.

5.3.4 3D Printing

After identifying the most promising HTD7 resin and optimizing its heat treatment, we set out to determine the feasibility of DLP printing. Early experiments with standard printers in a bottom-up configuration were unsuccessful due to the high tackiness of the thiol-ene, which excessively polymerized to transparent print windows and were damaged during inter-layer motion of the print bed. Therefore, we built the DLP printer described in the Materials section in a top-down orientation to bypass the need for a window interface altogether. We printed the resin under atmospheric conditions; because thiol-ene polymerization circumvents O₂ inhibition through hydrogen abstraction of thiols, thiol-ene resins may be printed without the need for an inert environment. While we did not attempt to optimize the printing resolution in this proof-of-concept, we estimate the XY feature size to be on the order of a few hundred microns due to light diffusion and reflection from the print bed, and the Z resolution to be approximately 85 μm as a result of resin viscosity and surface tension effects.

Moreover, most of the light reflection effect took place at early layers, which was removable using a razor blade in a manner similar to “print skirts” used by many current printers. This gives us confidence that print resolution can be improved with the appropriate inclusion of dyes and light filters. Informed by the photo-DSC results, we found successful prints used layer exposure times of 20 seconds, which equates to an extent of reaction around 80% as measured by total heat of polymerization. Using several simplified models of gelation such as Flory’s statistical theory, Carother’s theory, and the Bethe Lattice model,^[129, 187] we calculate that network formation of HTD7 does not occur until extent of reaction reaches 96.5-98.8%, which occurs at approximately 74 seconds in this system. Thus, the layers formed at 20 seconds of exposure are not single-networks, but a loosely connected collection of branched chains further capable of bonding to successive layers. Examples of printed objects, such as ASTM dogbones and an open-faced hollow cube, are presented in Figure 37.

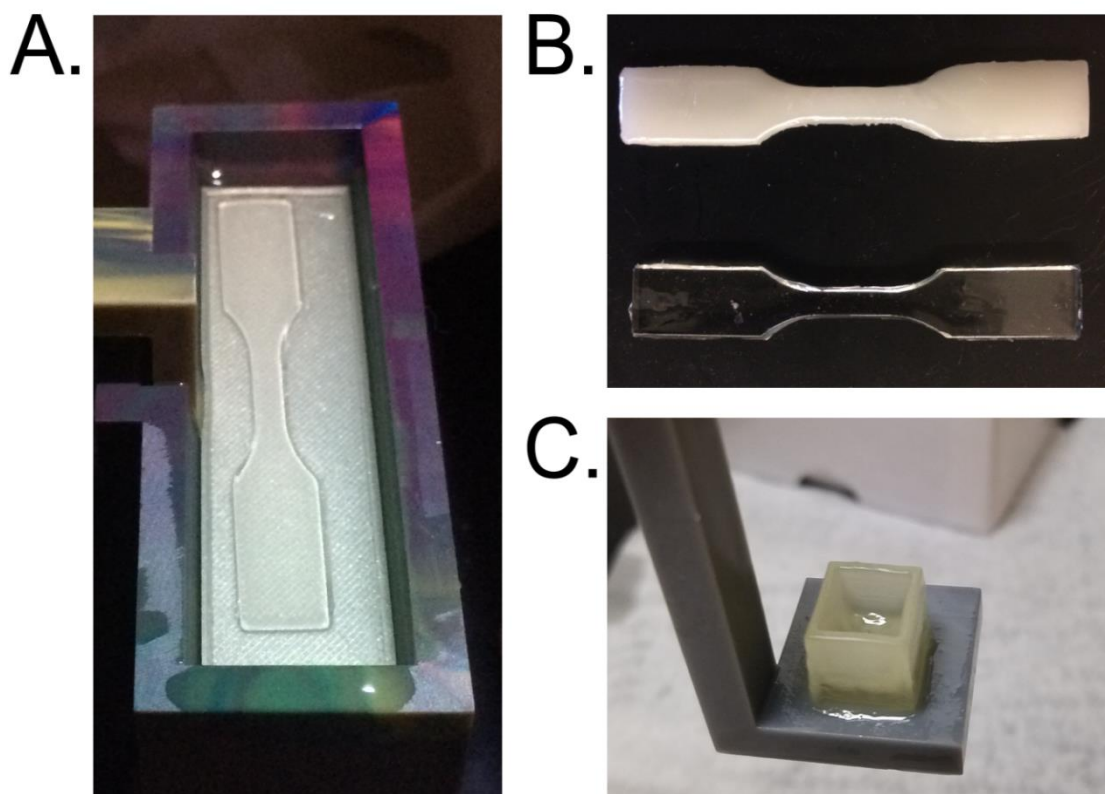


Figure 37: Printed HTD7 parts. A. An ASTM D638 Type V dogbone mid-print. B. Annealed versus non-annealed printed dogbones. C. Printed hollow cube.

After printing the dogbones of Figure 37, we compared the thermo-mechanical behavior of both annealed and non-annealed printed dogbones to their cast analogues. As shown in Figure 38a, we found very few thermal differences between the two methods of manufacture. Non-annealed dogbones were indistinguishable from cast ones with respect to T_g , E_1 and E_2 , and crystallinity measured by enthalpy of fusion. Interestingly, we found that annealing printed parts led to greater diversion from the properties established using cast samples. For example, the breadth of the glass-transition region of printed HTD7 was found to be approximately 10 °C wider than cast

HTD7, which indicates a more heterogeneous material morphology. This stands in contrast to the non-annealed samples that have no distinct differences in their thermal transition behavior.

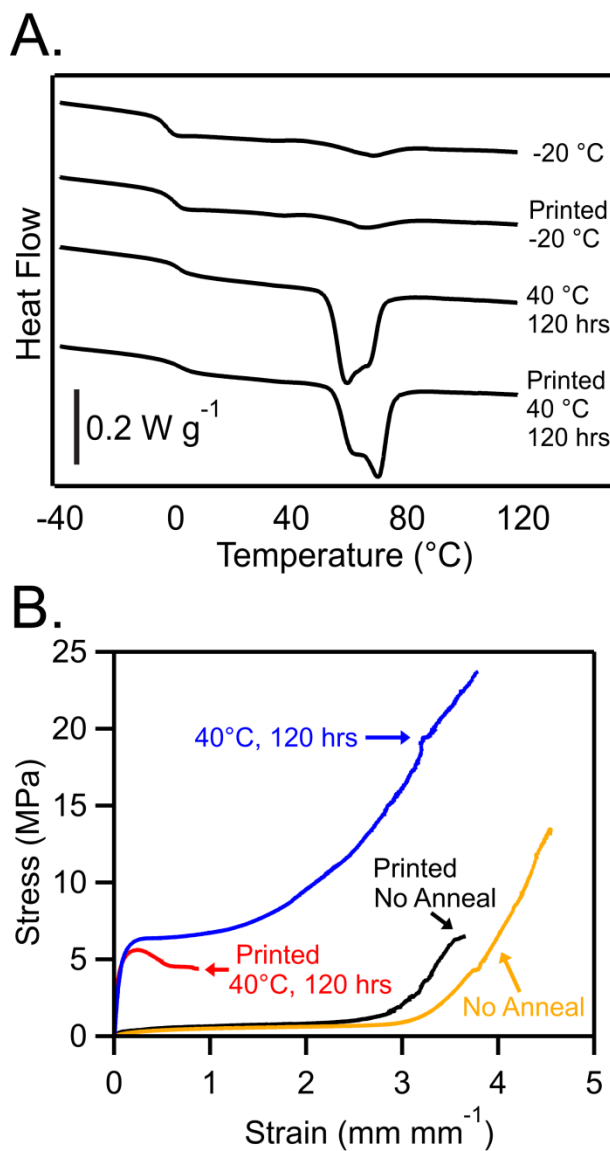


Figure 38: Characterization of printed parts and comparison to their non-printed analogues. A. DSC heating curves. B. Tensile stress-strain behavior.

We hypothesize increased heterogeneity is a direct result of the layer-by-layer nature of DLP printing. While the 100 μm slice thickness of printed parts is sufficiently large to permit the formation of both crystallite populations and effectively conserves the volume fraction of crystallizable polymer, thin discontinuities at layer interfaces likely act as disruptive boundaries that weaken printed parts. Their effect is visualized in the stress-strain comparison plot of Figure 38b, in which printed dogbones demonstrate significantly reduced failure strain and strength than their cast counterparts. Non-annealed prints achieved failure strains over 350%, and annealed samples failed at 108% strain; both groups, and especially the annealed materials, consistently underperformed relative to the cast dogbones. We propose that such a drastic stress and strain reduction results from the layer-discontinuity phenomena. Because each layer leaves fewer free functional groups to polymerize in the Z-direction than cast material, the interlayer boundaries are the likely failure points under load and explain why no increase in ultimate strength occurred between the annealed and non-annealed printed parts. In fact, average ultimate strength actually decreased with annealing. This unintuitive result is probably due to crystallization-induced shrinkage within each layer, which would create voids and increase stress on the chains that connect the printed cross-sections. Thermal and mechanical data for printed HTD7 is located in Table 3 and Table 4, respectively.

Table 3: Thermal data from 3D printed annealed and non-annealed parts.

Sample Group	T _g (°C)	T _g Breadth (°C)	Endotherm 1 (°C)	Endotherm 2 (°C)	Enthalpy of Fusion (J g ⁻¹)
Printed -20 °C 120 hrs	-0.86 ± 0.73	7.10 ± 1.06	36.91 ± 1.24	67.64 ± 2.04	1.71 ± 1.00
-20 °C 120 hrs	-2.40 ± 0.34	6.43 ± 0.25	34.39 ± 1.46	70.50 ± 2.18	1.45 ± 0.35
Printed 40 °C 120 hrs	-3.81 ± 3.95	15.00 ± 3.27	59.49 ± 1.08	69.28 ± 1.46	19.74 ± 1.61
40 °C 120 hrs	0.81 ± 0.30	5.21 ± 0.36	59.23 ± 0.52	66.04 ± 1.39	16.41 ± 2.29

Table 4: Tensile data from 3D printed annealed and non-annealed parts.

Sample Group	Yield Stress (MPa)	Yield Strain (mm mm ⁻¹)	Failure Stress (MPa)	Failure Strain (mm mm ⁻¹)	Ultimate Stress (MPa)	Ultimate Strain (mm mm ⁻¹)	Toughness (MJ m ⁻³)
Printed -20 °C 120 hrs	0.30 ± 0.10	0.22	5.55 ± 3.74	3.72 ± 0.59	5.58 ± 3.75	3.71 ± 0.60	5.90 ± 2.51
-20 °C 120 hrs	0.29 ± 0.07	0.22	14.84 ± 2.57	4.80 ± 0.43	14.98 ± 2.78	4.80 ± 0.44	12.13 ± 1.16
Printed 40 °C 120 hrs	5.86 ± 0.67	0.20 ± 0.05	4.20 ± 0.71	0.64 ± 0.24	5.86 ± 0.67	0.20 ± 0.05	3.31 ± 1.57
40 °C 120 hrs	6.84 ± 0.29	0.36 ± 0.05	24.07 ± 1.87	3.91 ± 0.17	24.07 ± 1.87	3.91 ± 0.17	46.04 ± 4.75

5.4 Conclusions

In this report, we have described a photo-printable thiol-ene resin with impressive mechanical properties that result from its chemistry and morphology. This resin is stable when stored under dark, room-temperature conditions. The morphology and crystallization kinetics of HTD7 are tunable by controlling the post-production heat

treatment regimen, which effects the bimodal distribution of crystallite sizes present in the material. In turn, control of the material structure makes it possible to tune the thiolene's tensile behavior. We determined that annealing samples at 40 °C for 120 hours is an optimal balance between efficiency and improved mechanical properties like yield strength and toughness. Because HTD7 polymerizes in a rapid, controlled manner when exposed to white light, we compared DLP-printed samples to cast ones to better understand the effect of 3D printing on the morphology and mechanics of the spiroacetal resin. While we found crystallinity to be relatively unaffected by printing, interlayer boundaries act to make the material more heterogeneous and introduce failure points that cause early failure under tension; this problem could be addressed using a more continuous print method such as that pioneered by the DeSimone group.^[153] Our results prove that spirochemistry holds promise as a motif that may be incorporated into the backbone of traditionally weak polymers to improve their performance.

Chapter 6. Conclusions

Chapters 3-5 have focused on two respective material systems, namely, a PEGDA-BSA IPN hydrogel and photoinitiated, semicrystalline thiol-ene bulk polymer networks. The research in Chapter 3 successfully demonstrated a robust, biocompatible system that could be 3D printed via extrusion-deposition. However, several fundamental limitations in the work discouraged further examination and catalyzed a shift in the material platform of interest. In brief, these limitations stemmed from the high degree of swelling of the hydrogel; the extreme hydrophilicity of the PEGDA resulted in 3X volumetric swelling, which placed a high internal stress on the covalent network and therefore reduced extensibility and load-bearing capacity. Furthermore, the calcium concentration required for optimal ionic bonding of the secondary network, brown sodium alginate, was determined to be far in excess of equilibrium calcium concentrations found throughout human physiology. Ionic bonding was also determined to be hampered by monovalent ions present in cell media or saline such as sodium and potassium.

The work in Chapters 4 and 5 addresses the shortcomings of Chapter 3 through the use of different polymer toughening and strengthening mechanisms. Instead of relying upon reversible ionic dissipation in an aqueous environment, the focus becomes using thermomechanical damping (operating near the glass transition point of the polymer), crystalline domains, and an open and modular chemistry that facilitates a

wide variety of backbone structures. The results are encouraging, and show the potential of a robust and tunable material platform. Further, the resin was successfully 3D printed, with impressive tensile behavior that exceeds many commercially available options. Furthermore, the effect of heat treatment on the material morphology and mechanical profile has been elucidated. This has implications on the morphology of the thiol-ene, and therefore a more thorough understanding of the crystal structure(s) present in the material is advised. The biocompatibility of thiol-spiroacetal alkene materials should be verified *in vitro* to confirm that the copolymer is equally benign as its individual components have demonstrated in previous literature reports.^[44] Last, because this material is being considered for long term use inside of the human body as an implant material, an understanding of how this material performs and withstands the environment (elevated temperature, aqueous environment filled with salts, acidic or basic pH dependent on the locale, etc.) should be pursued. Some of these proposed investigations are detailed more precisely in the following subsections, supplemented with preliminary data to add to the discussion.

6.1 Future Studies and Initial Findings

6.1.1 Biocompatibility Assays

As has been previously stated, many thiols and alkenes are biocompatible and therefore of interest for their incorporation in medical implants. In fact, hexanedithiol is currently used as an additive in many food products, and 3,9-divinyl-2,4,8,10-

tetraoxaspiro[5.5]undecane has shown biocompatibility as a drug carrier when polymerized with hydroxyethyl methacrylate (HEMA).^[43-45] However, all novel material combinations are subject to increased scrutiny from the FDA before they are approved for biomedical applications, and therefore it is important to begin this process by investigating HDT-TMPTMP-DVTU's degree of cytotoxicity. To begin, we collected effluent from HTD7 by immersing it in culture media supplemented with 10% bovine calf serum (BCS) for 120 hours at 37 °C in a sterile environment. Following this, we cultured mouse fibroblast (3T3) cells in the presence of the extract for 5 days in a serial dilution from 1:1 through 1:32 dilution according to ASTM F619 and ISO 10993 and assayed their viability using LIVE/DEAD analysis with Calcein AM and propidium iodide. Although we used a photoinitiator known to be biocompatible, Irgacure 2959, we tested both 1 wt% and 0.1 wt% photoinitiator to determine if there is a concentration-dependency of cell viability. The results of both 5 day viability tests are shown below. In general, we found high viability with both photoinitiator concentrations; this suggests good biocompatibility of spiroacetal thiol-enes. We believe the reduction of viability at lower dilutions in the low-PI populations of Figure 39A is a result of overseeding the initial cell density and not representative of increased toxicity at lower extract concentration. Further, the 1:16 dilution group was contaminated and therefore is not shown. All population groups were also scored for qualitative viability and health on a 1-4 scale in a double-blind, randomized fashion by 5 trained, independent researchers.

Every group received a score of 2 or lower, which is generally accepted to describe non-toxic material.

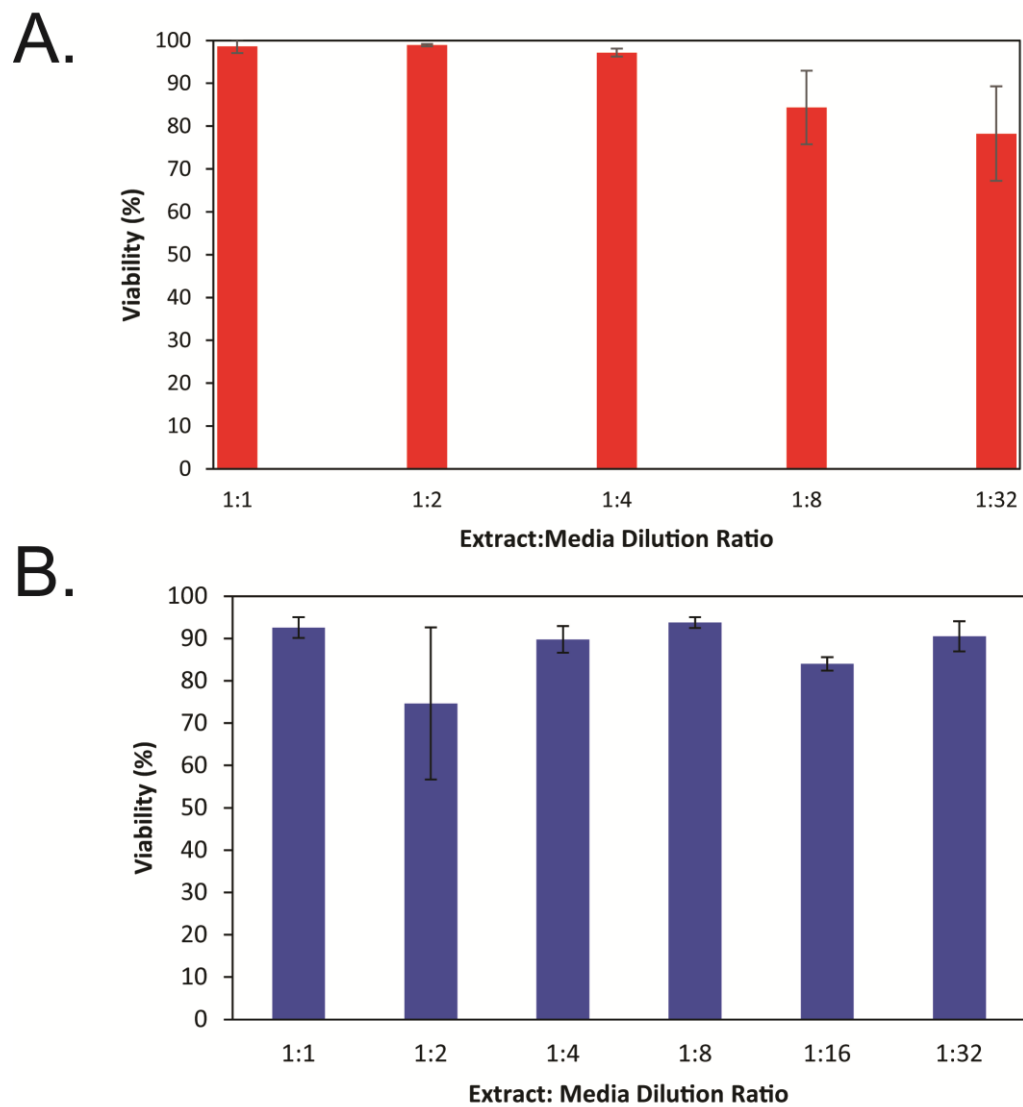


Figure 39: 3T3 Viability. A. HTD7 Extract with 0.1 wt% PI. B. HTD7 Extract with 1 wt% PI.

Because initial biocompatibility testing yielded such positive results, the next steps are cell culture experiments in contact with HTD7 surface, leachant testing, and *in vivo* testing in a mice model.

6.2 Polymer Crystallinity

Though the work of Chapters 4 and 5 illustrates the relationships between heat treatment, crosslinking, crystallinity, and thermomechanical properties of thiol-ene materials containing spiroacetal monomers in the backbone, it does not identify the specific nature of crystal domains of the material in any appreciable. Therefore, further studies are required to better understand the fundamental structure of the material. To this end, preliminary investigations have been conducted using a light microscope on the surface of several of the HDT-TMPTMP-DVTU compositions studied. It has been found that low concentrations of crosslinking can result in distinct crystal domains on the order of 50-200 μ m, as depicted in Figure 21 and Figure 40.

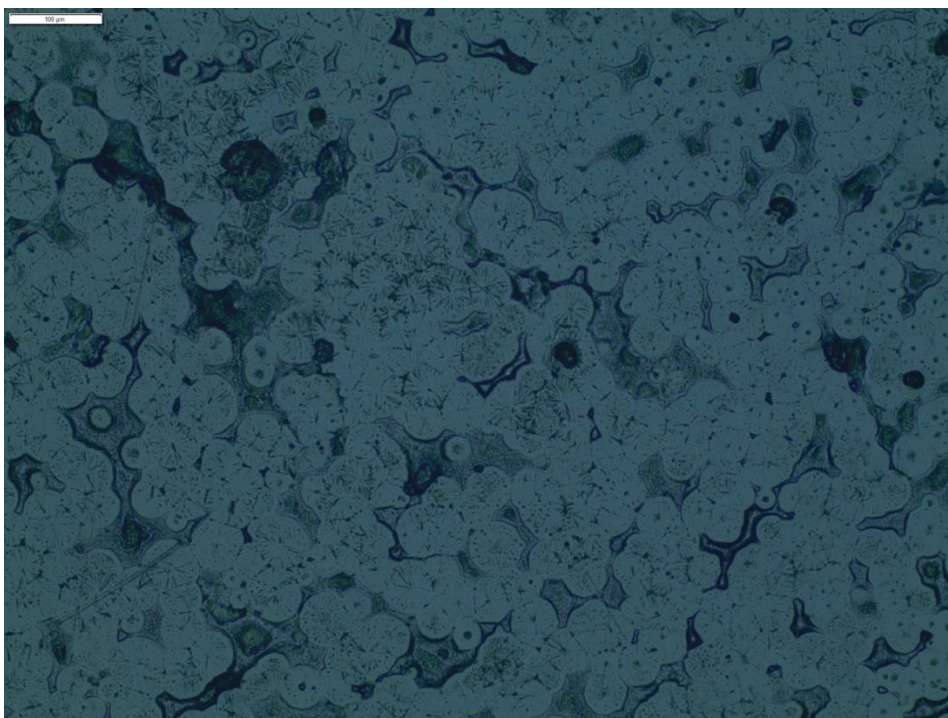


Figure 40: Spherulite Presence in HDT-TMPTMP-DVTU (200X Magnification)

Samples with crosslinking concentrations greater than 12.5 t_{mol}% do not depict this morphology, and even within samples of similar TMPTMP concentration it can be more of an art than science in obtaining a quality picture of the crystal domains. To supplement light microscopy, I have run x-ray diffraction (XRD) scans of HDT-TMPTMP-DVTU as well as DVTU monomer using the Panalytical X'Pert PRO MRD HR X-Ray Diffraction System in the Duke SMiF facility. The scans of the polymer and monomer are depicted in the figures below.

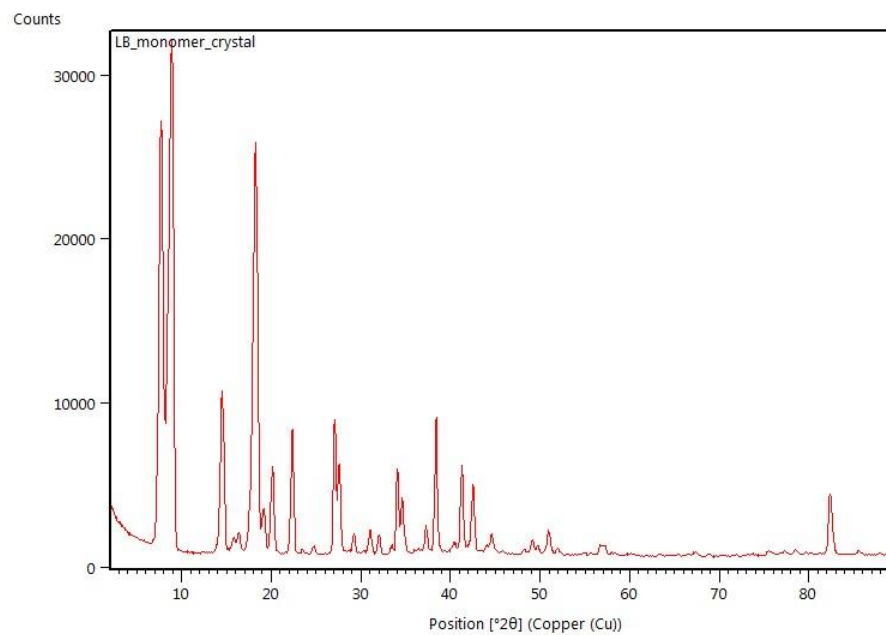


Figure 41: DVTU Monomer X-ray Diffraction

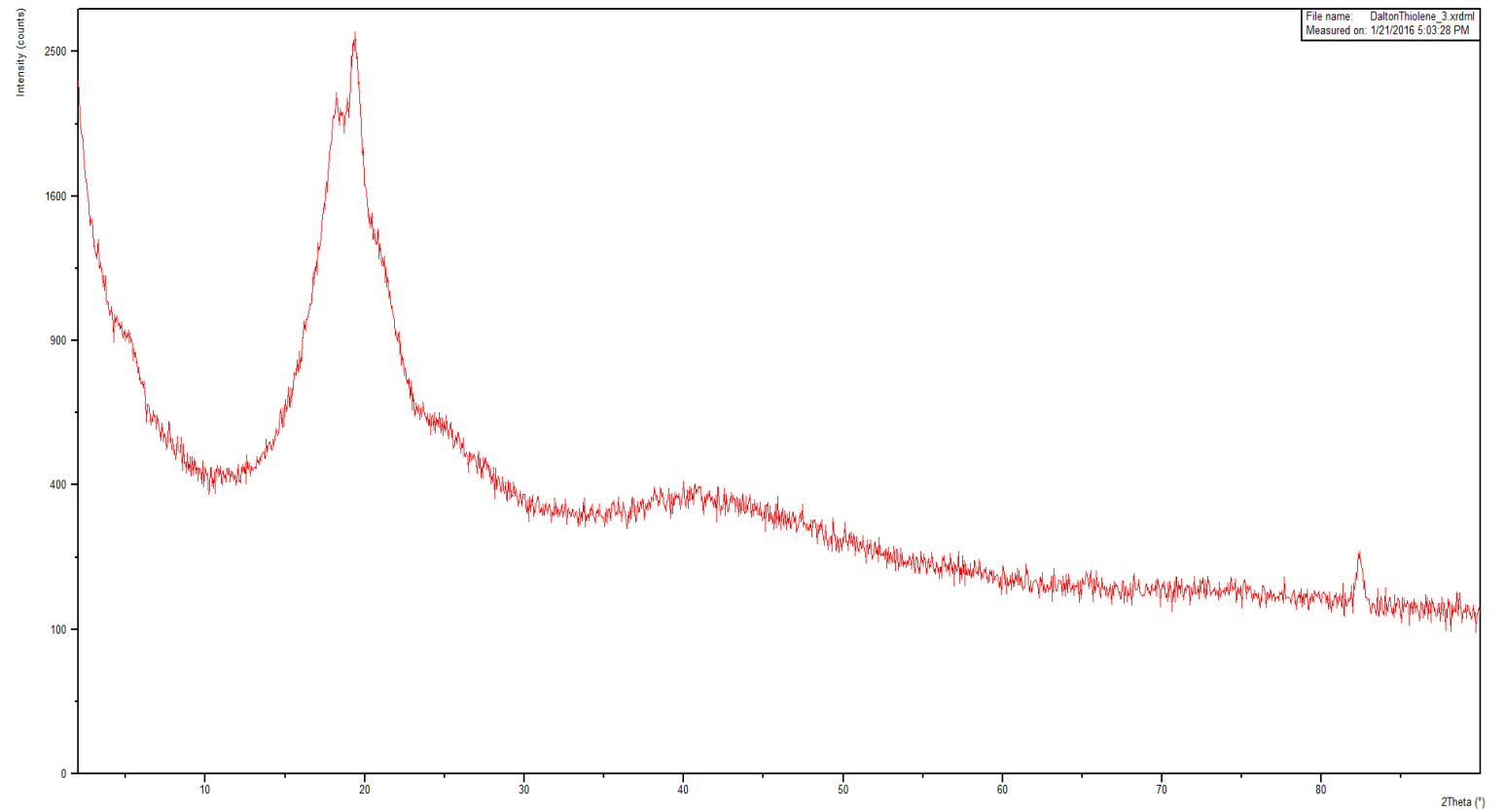


Figure 42: HDT-DVTU X-ray Diffraction Spectrum

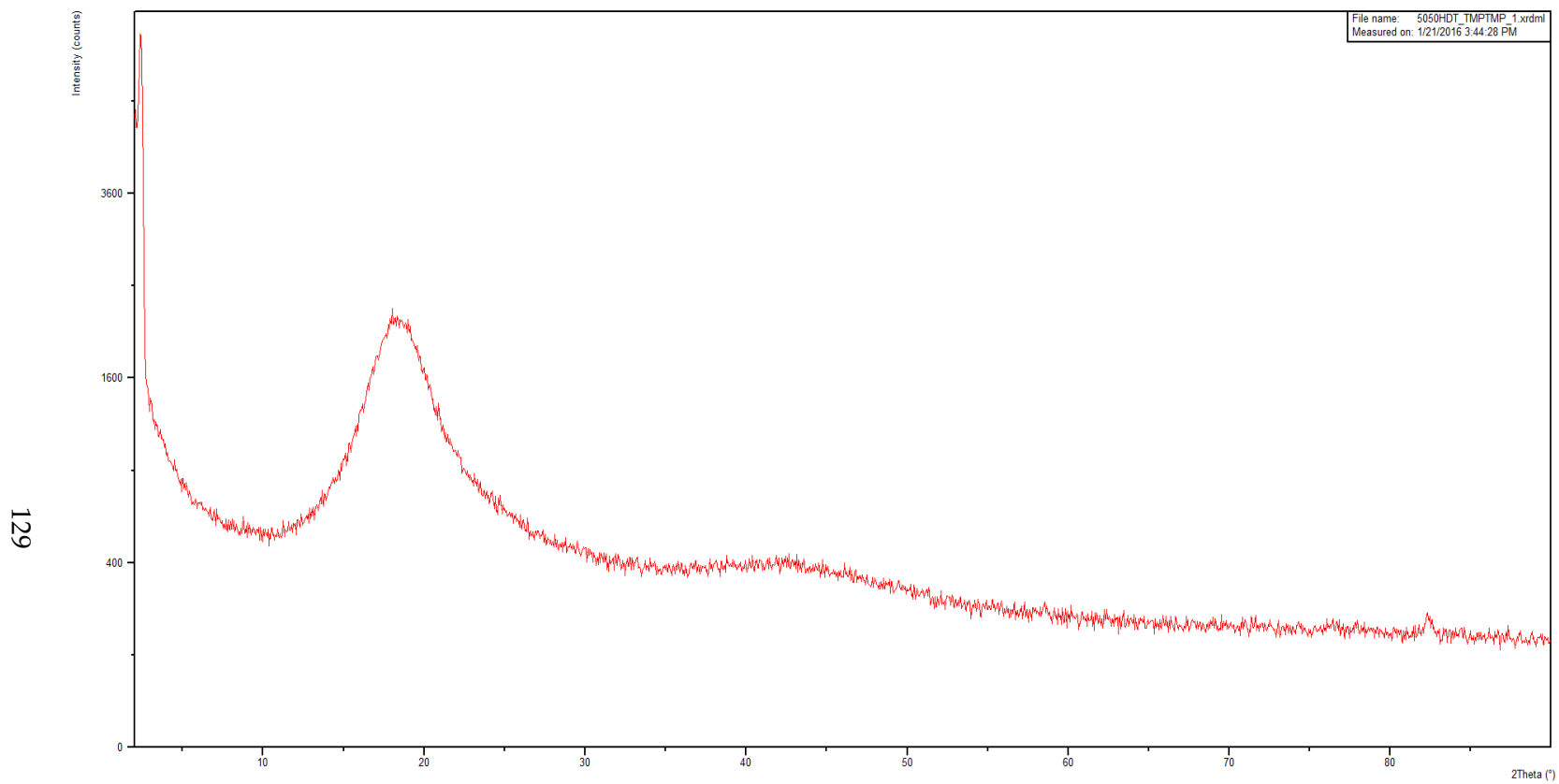


Figure 43: HDT-TMPTMP-DVTU-50 X-ray Diffraction Spectrum

It is clear from Figure 41 that while DVTU monomer adopts many crystallite forms, only those near $2\theta = 18-22^\circ$ and 82° are conserved in the lightly crosslinked polymer networks. Diffraction peaks in the $18-22^\circ$ range correspond to d-spacing of 4-5 Å, while the peak at 82° has a d-spacing of 1.17 Å. The Scherrer Equation:

$$S(2\theta) = \frac{K\lambda}{L\cos(\theta)} \quad (6.2.1)$$

is useful in determining crystallite size. Here the crystallite size, $S(2\theta)$, is equal to the Scherrer constant, K , multiplied by the wavelength of X-ray used, λ , divided by peak full width at half maximum, L , and the cosine of the Bragg angle, θ . Using the equation and setting K to 1, we found that crystallites in HDT-TMPTMP-DVTUs ranged in size from approximately 11.6-20.3 nm.

Higher crosslinking, as shown in Figure 43, suppresses the individual peaks and results in an amorphous microstructure. In addition, unpublished work by collaborator Dr. David Tavakoli has shown that these peaks do not shift with increasing temperature; this is further indication that the dual-endotherm behavior described in Chapters 4 and 5 is a result of two distinct crystal size distributions and not multiple crystal structures.

6.4 Environmental Effects and Long Term Material Performance

In theory, the thiol-ene materials discussed herein have the potential to perform in a soft tissue-augmenting or replacing role. However, further study is required to determine their potential for use as artificial cartilage, which is an attractive potential application due to the relatively avascular and acellular nature of load-bearing

cartilage.^[6] The first step in determining the fitness of these thiol-enes for long term applications begins in understanding how protracted exposure to body-like conditions affects key characteristics of the materials. For example, it has been shown in (meth)acrylate systems that absorbed water acts as a plasticizing agent on the network and depresses the glass transition temperature of the material.^[29] Furthermore, water absorption can disrupt intermolecular interactions such as hydrogen bonding and cause significant internal stress via swelling of the network.¹ Therefore, a long term study has been conducted to determine several of these effects on an appropriate selection of thiol-ene materials. Specifically, samples were immersed in phosphate buffered saline at 37°C for 30 days, after which times tensile testing and swelling measurements were performed to elucidate how key performance metrics are affected by simulated *in vivo* conditions.

As shown in the figure below, HDT-TMPTMP-DVTU-10 swelled by approximately 1 wt% at 30 days immersion in PBS and 2% at 60 days. We believe that the hydrophobic nature of the thiol-ene (which was found to be approximately 85 degrees as measured by water contact analysis), combined with the high packing density of semi-crystalline polymers, contributes to the thiol-ene's reduced swelling of polar fluids such as saline. Low swelling, especially in comparison to many amorphous

¹ This was seen in the work of Chapter 2 to be particularly true when the solution contains dissolved ionic species.

(meth)acrylate networks,^[29] is a good indication that long term immersion in body-like conditions will not have a pronounced effect on polymer morphology or properties.

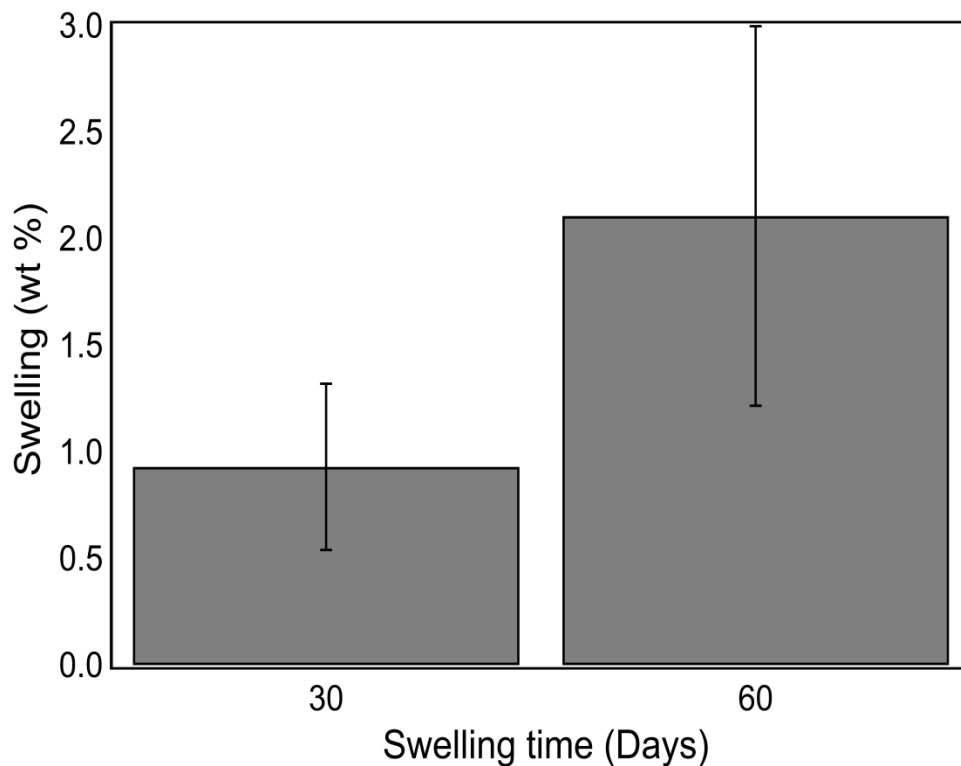


Figure 44: HDT-TMPTMP-DVTU-10 Swelling Behavior.

In addition to minimal swelling, we found that tensile behavior was also relatively unchanged for both 30 and 60 day immersion tests in PBS. Yield strength, ultimate strength and strain, as well as toughness all remained consistent between control and test groups, as shown below in the representative curves.

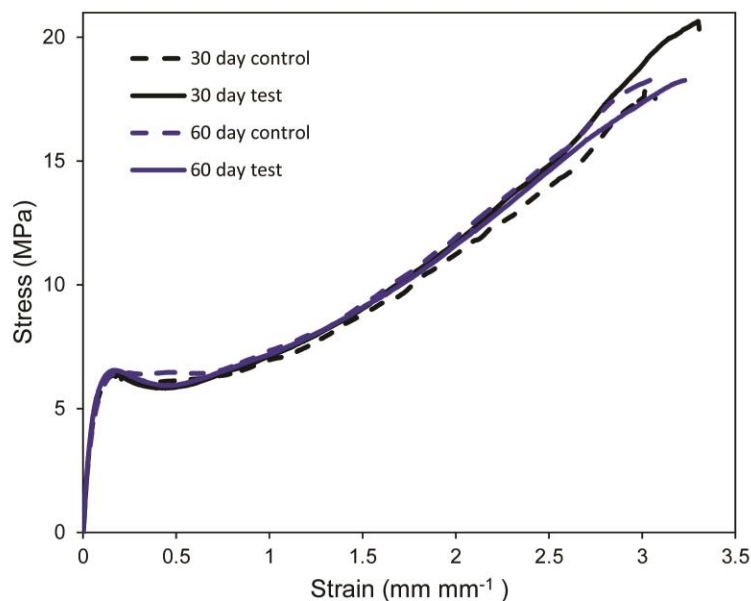


Figure 45: Stress-Strain Behavior After PBS Immersion.

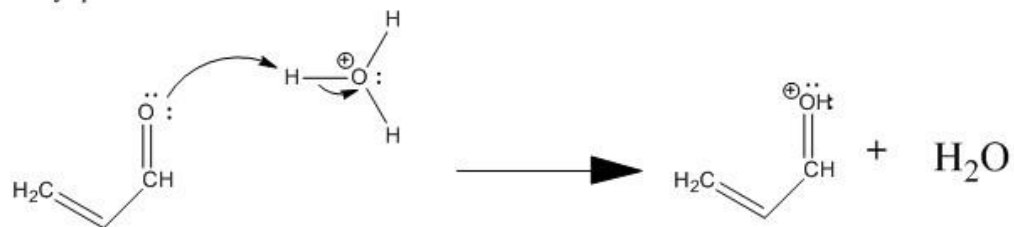
The preceding tests have all evaluated material performance under relatively short-term testing conditions; however, factors such as creep, dislocation movement, polymer scission, crack propagation and more all work to degrade polymeric material performance over extended periods of time. While the thiol-ene system under current investigation isn't classified as a "self-healing" material in the sense that there are designed mechanisms to repair damage over time, it does benefit for a unique thermomechanical effect that may increase the longevity of the material under extended loading. This effect, as shown in the work of Chapter 4, is that all compositions of HDT-TMPTM-DVTU (i.e. materials spanning from thermoplastic to highly crosslinked network) are above their T_g but below the first crystal melting peak at room

temperature. This indicates that the materials anneal their crystals in conditions requiring nothing further than a shelf to store them.^[197, 198] Therefore, further testing for shape memory effects and sustained load-bearing are also being considered as we move forward with the material platform.

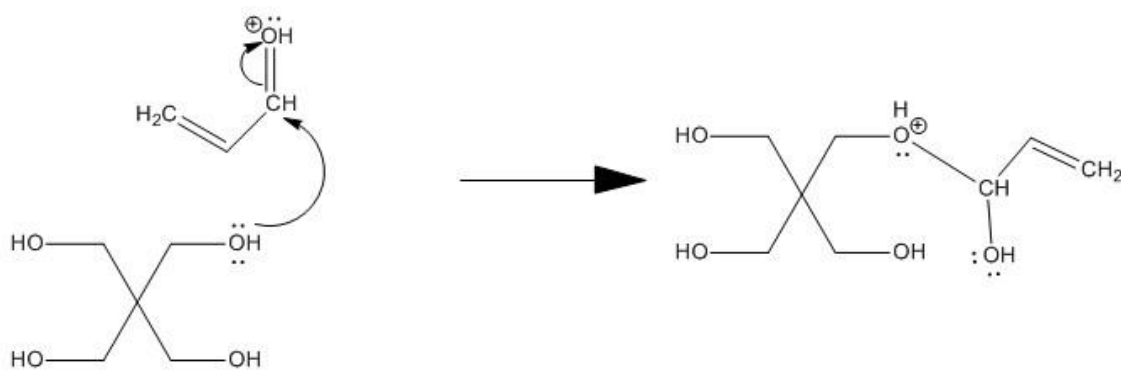
Appendix A: Synthesis of 3,9-divinyl-2,4,8,10-tetraoxaspiro [5.5] undecane (DVTU)

DVTU is synthesized through a series of protonation, deprotonation, and nucleophilic attack reactions between the tetrafunctional alcohol pentaerythritol and the aldehyde acrolein. A schematic outlining the reaction is shown on the following pages.

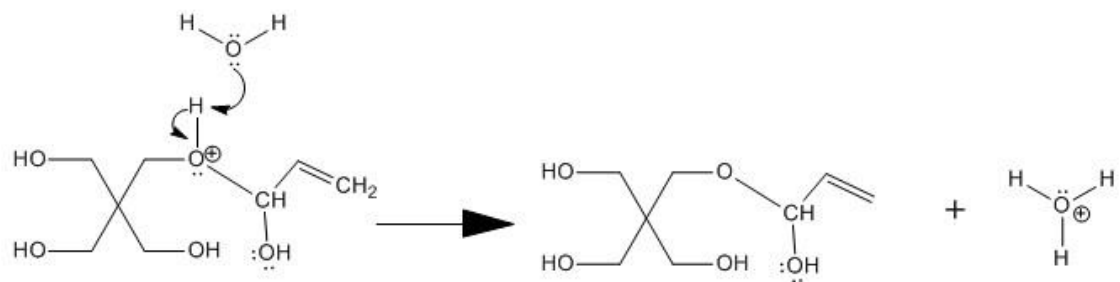
Carbonyl protonation



Nucleophilic attack by alcohol of pentaerythritol

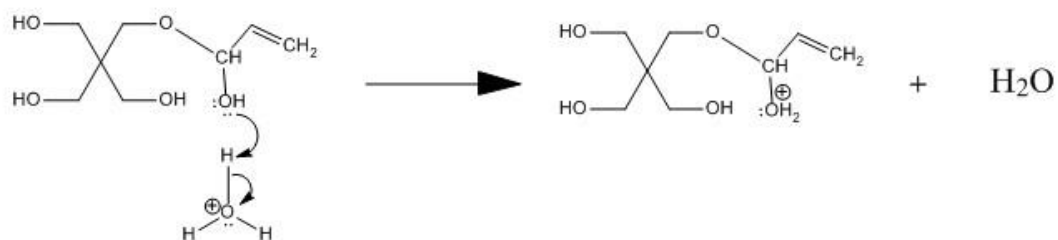


Hemiacetal formation via deprotonation

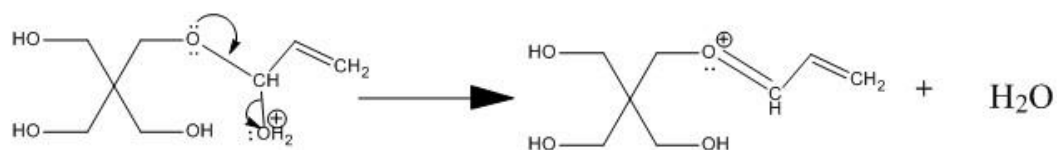


Scheme 2: Synthesis of DVTU molecule, Part 1.

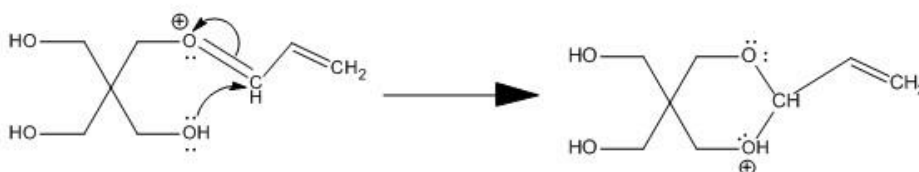
Alcohol protonation



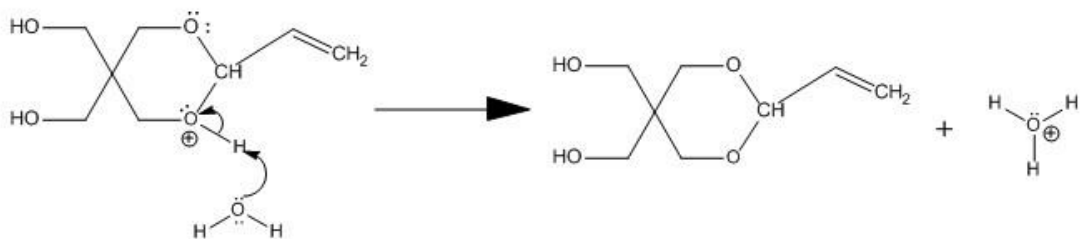
Water removal



Nucleophilic attack by same-molecule alcohol



Deprotonation via water



Repeat for opposite side

Scheme 3: Synthesis of DVTU molecule, Part 2.

Appendix B: Structures and Names of Select Thiols, Alkenes, and (Meth)Acrylate Monomers

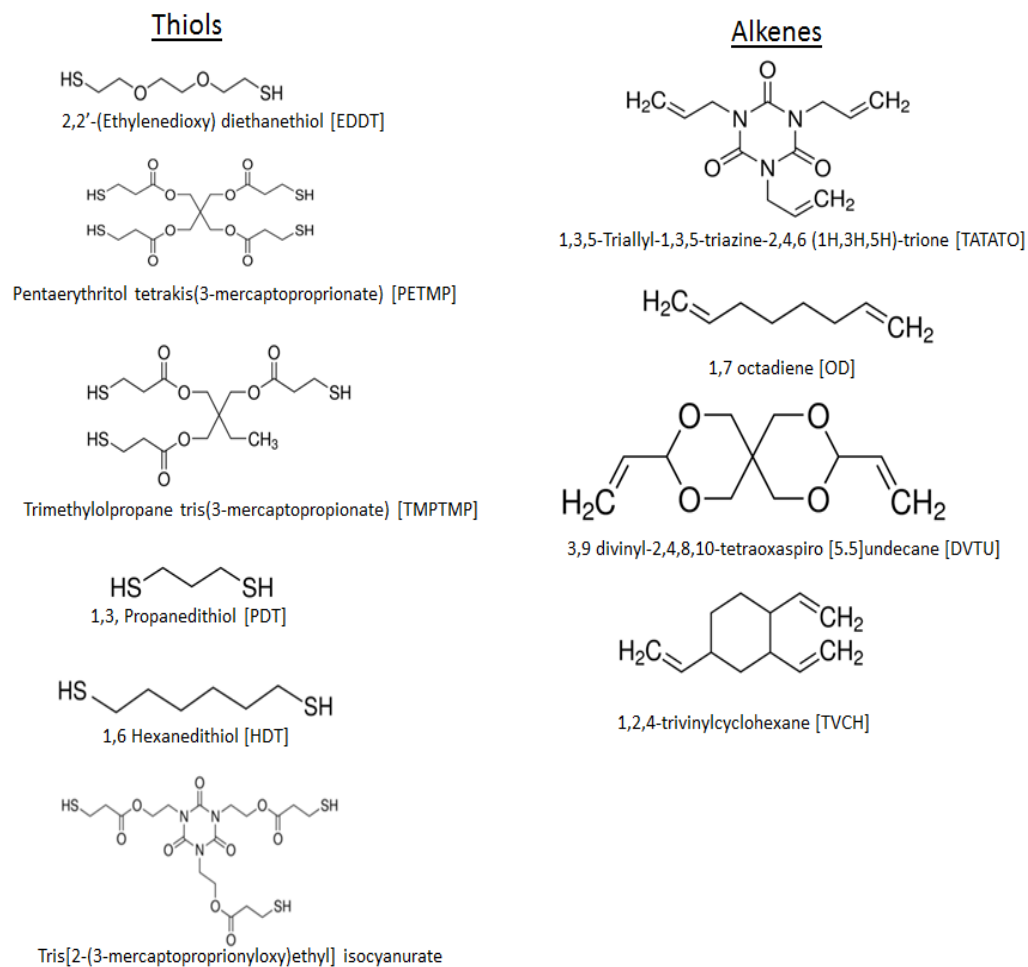
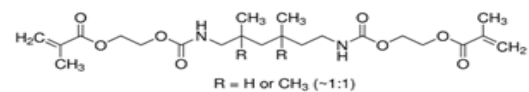
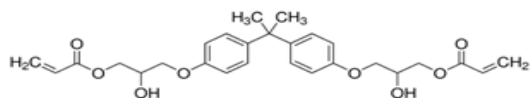


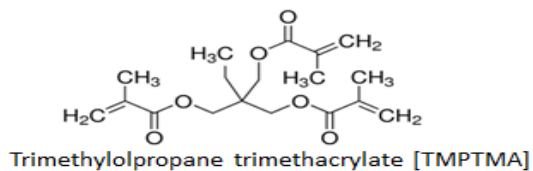
Figure 46: Thiol and Alkene Monomers Screened



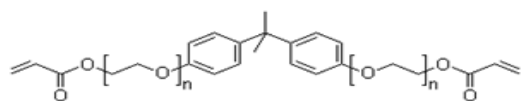
Diurethane dimethacrylate [DUDMA]



Bisphenol A glycerolate diacrylate [BPAGDA]

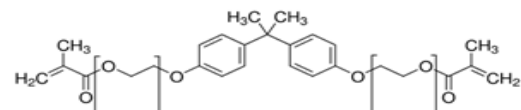


Trimethylolpropane trimethacrylate [TMPTMA]

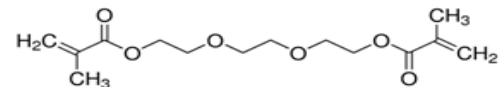


Bisphenol A ethoxylate diacrylate [BPAEDA]

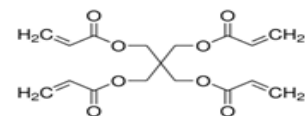
Acrylates



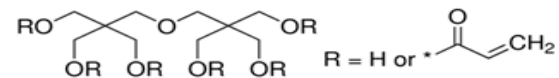
Bisphenol A ethoxylate dimethacrylate [BPAEDMA]



Triethylene glycol dimethacrylate [TEGDMA]



Pentaerythritol tetraacrylate [PETA]

Tricyclo[5.2.1.0^{2,6}]decanedimethanol diacrylate [TCDMA]

Dipentaerythritol penta-/hexa-acrylate [DPETA]

Figure 47: (Meth)Acrylate Monomers and Oligomers Screened

Appendix C: Various Tabulated Data

Table 5: Thiol and Alkene Conversion via ATR-FTIR

Material	Thiol conversion (UV only)	Thiol conversion (UV + postcure)	Alkene conversion (UV only)	Alkene conversion (UV + postcure)
HDT-DVTU	91.1 ± 0.7	91.6 ± 0.5	97.3 ± 0.3	97.3 ± 0.5
TMPTMP-DVTU	92.5 ± 0.4	92.7 ± 0.2	96.7 ± 0.6	97.1 ± 0.9
HDT-TMPTMP-DVTU-7.5	93.0 ± 0.5	93.6 ± 0.9	97.8 ± 0.4	98.0 ± 0.6
PDT-DVTU	94.4 ± 0.8	95.0 ± 0.2	97.7 ± 0.2	97.4 ± 0.7

Table 6: Enthalpy of fusion, crystalline melting temperatures, and glass transition temperatures of various compositions of PDT- and HDT-TMPTMP-DVTU polymers as measured by DSC.

TMPTMP (t_{mol}%)	Total enthalpy of fusion (J/g)	Temperature of primary melting endotherm (°C)	Temperature of secondary melting endotherm (°C)	Glass transition temperature (°C)
0	27.0 ± 0.5	46.1 ± 0.3	80.4 ± 0.4	-6.3 ± 0.2
2.5	25.5 ± 0.6	47.2 ± 0.1	75.2 ± 0.6	-5.0 ± 0.5
5	23.9 ± 0.6	46.7 ± 0.1	69.1 ± 0.2	-3.9 ± 0.1
7.5	22.4 ± 0.5	46.5 ± 0.1	65.9 ± 0.1	-1.1 ± 0.1
10	21.9 ± 0.4	47.0 ± 1.3	65.1 ± 0.1	-0.8 ± 0.2
12.5	17.1 ± 0.9	48.1 ± 0.3	60.0 ± 0.4	0.4 ± 0.1
15	15.4 ± 0.4	46.7 ± 0.1	56.3 ± 0.4	1.4 ± 0.4
17.5	12.3 ± 0.2	46.3 ± 0.2	N/A	3.0 ± 0.2
20	7.7 ± 1.4	46.4 ± 0.2	N/A	1.9 ± 0.2
50	N/A	N/A	N/A	9.2 ± 0.2
100	N/A	N/A	N/A	20.8 ± 0.1
PDT-DVTU	0.8 ± 0.1	59.9 ± 0.1	N/A	8.9 ± 0.5
PDT- TMPTMP- DVTU-7.5	N/A	N/A	N/A	9.4 ± 0.3
PDT- TMPTMP- DVTU-20	N/A	N/A	N/A	11.7 ± 0.4
DVTU Monomer	96.5 ± 3.1	46.7 ± 0.3	N/A	N/A

Table 7: DMA and gel fraction data for HDT-TMPTMP-DVTUs reported as mean \pm one standard deviation.

TMPTMP ($t_{\text{mol}}\%$)	Glassy Modulus (MPa)	Rubbery Modulus (MPa)	Young's Modulus at T_g (MPa)	T_g via $\tan\delta$ ($^{\circ}\text{C}$)	Peak $\tan\delta$	FWHM ($^{\circ}\text{C}$)	Gel Fraction (%)
0	2089 \pm 76	N/A	535.01 \pm 20.23	19.05 \pm 0.72	0.22 \pm 0.01	27.52 \pm 0.53	N/A
2.5	2129 \pm 107	N/A	451.48 \pm 62.70	20.53 \pm 1.69	0.27 \pm 0.03	25.34 \pm 0.30	N/A
5	2157 \pm 189	0.20 \pm 0.02	447.85 \pm 20.19	19.15 \pm 0.19	0.29 \pm 0.03	24.61 \pm 1.06	40.42 \pm 4.33
7.5	2160 \pm 83	0.73 \pm 0.04	423.99 \pm 38.29	21.66 \pm 1.27	0.29 \pm 0.01	23.44 \pm 0.96	75.00 \pm 4.39
10	2212 \pm 54	0.91 \pm 0.06	369.48 \pm 17.89	23.28 \pm 0.77	0.36 \pm 0.02	21.10 \pm 0.15	74.60 \pm 1.44
12.5	2230 \pm 92	1.73 \pm 0.13	326.88 \pm 28.47	24.08 \pm 0.77	0.38 \pm 0.02	21.22 \pm 0.54	83.19 \pm 4.71
15	2031 \pm 34	2.45 \pm 0.07	208.41 \pm 23.06	19.12 \pm 1.70	0.52 \pm 0.02	20.04 \pm 0.52	74.99 \pm 4.02
17.5	1406 \pm 581	2.98 \pm 0.11	146.41 \pm 65.42	15.74 \pm 1.55	0.90 \pm 0.12	13.45 \pm 1.85	73.55 \pm 9.27
20	1136 \pm 121	2.43 \pm 0.12	131.14 \pm 19.36	14.07 \pm 1.54	0.95 \pm 0.09	13.07 \pm 1.18	89.25 \pm 2.09
50	1696 \pm 186	4.41 \pm 0.08	32.80 \pm 3.17	24.71 \pm 1.71	1.78 \pm 0.07	10.74 \pm 0.27	94.69 \pm 1.27
100	1712 \pm 311	6.38 \pm 0.12	42.18 \pm 2.59	34.79 \pm 0.50	1.58 \pm 0.01	10.88 \pm 0.29	95.57 \pm 0.61

Table 8: Toughness and mechanical properties as a function of crosslink density in HDT-TMPTMP-DVTUs and PDT-TMPTMP-DVTUs at 22°C.

TMPTMP (t _{mol} %)	Yield Stress (MPa)	Yield Strain (mm/mm)	UTS (MPa)	Strain at UTS (mm/mm)	Failure Stress (MPa)	Failure Strain (mm/mm)	Toughness (MJ/m ³)
0.0	8.34 ± 0.93	0.08 ± 0.02	8.34 ± 0.93	0.08 ± 0.02	7.75 ± 0.89	0.10 ± 0.03	0.91 ± 0.46
2.5	6.58 ± 0.23	0.10 ± 0.01	10.63 ± 1.19	3.37 ± 0.56	9.92 ± 1.15	3.42 ± 0.56	24.99 ± 5.67
5.0	6.32 ± 0.19	0.11 ± 0.01	11.95 ± 0.51	3.73 ± 0.25	11.63 ± 0.53	3.77 ± 0.25	29.01 ± 3.34
7.5	7.23 ± 0.17	0.13 ± 0.02	15.50 ± 0.72	3.57 ± 0.23	15.45 ± 0.72	3.62 ± 0.26	35.45 ± 3.67
10.0	5.74 ± 2.74	0.15 ± 0.08	14.32 ± 2.66	3.23 ± 0.59	14.20 ± 2.77	3.25 ± 0.61	28.72 ± 4.81
12.5	1.01 ± 0.10	0.03 ± 0.00	12.47 ± 0.46	4.09 ± 0.06	12.47 ± 0.46	4.09 ± 0.06	22.14 ± 0.92
15.0	0.61 ± 0.02	0.04 ± 0.01	13.52 ± 1.82	4.21 ± 0.06	13.52 ± 1.82	4.21 ± 0.06	18.94 ± 1.74
17.5	0.45 ± 0.06	0.05 ± 0.00	13.81 ± 2.12	4.12 ± 0.24	13.81 ± 2.12	4.12 ± 0.24	17.65 ± 2.19
20.0	0.46 ± 0.04	0.05 ± 0.01	7.41 ± 0.82	4.32 ± 0.34	7.37 ± 0.81	4.32 ± 0.34	13.27 ± 2.20
50.0	0.35 ± 0.03	0.07 ± 0.00	1.91 ± 0.35	0.82 ± 0.17	1.91 ± 0.35	0.82 ± 0.17	0.95 ± 0.35
100.0	0.64 ± 0.03	0.04 ± 0.01	9.71 ± 1.27	1.25 ± 0.04	9.71 ± 1.27	1.25 ± 0.04	5.09 ± .063
7.5, Video strain	7.35 ± 0.15	0.16 ± 0.01	15.33 ± 1.31	4.05 ± 0.19	15.31 ± 1.31	4.06 ± 0.20	35.97 ± 3.96
PDT-DVTU	0.80 ± 0.02	0.08 ± 0.01	0.80 ± 0.02	0.08 ± 0.01	0.72 ± 0.04	0.13 ± 0.03	0.27 ± 0.06
PDT-TMPTMP-DVTU-7.5	0.15 ± 0.07	0.51 ± 0.06	0.28 ± 0.14	7.22 ± 0.25	0.27 ± 0.14	7.28 ± 0.27	1.06 ± 0.56
PDT-TMPTMP-DVTU-20	0.12 ± 0.02	0.06 ± 0.01	1.60 ± 0.26	2.82 ± 0.11	1.59 ± 0.25	2.82 ± 0.11	2.33 ± 0.36

Table 9: Conversion of thiol and alkene functional groups in HDT-TMPTMP-DVTU-7.5 reveals no significant differences between all photoinitiator concentrations.

PI (wt%)	Thiol conversion (%)	Alkene conversion (%)
0.1	93.6 ± 0.9	98.0 ± 0.6
1.0	93.9 ± 0.6	98.5 ± 0.4
3.0	92.6 ± 2.2	97.2 ± 1.6

Table 10: Glass Transition and Crystalline Melting Data for HTD7 annealed at -20 °C through three weeks.

-20°C Isothermal (Hours)	T _g (°C)	T _g Breadth (°C)	Endotherm 1 (°C)	Endotherm 2 (°C)	Enthalpy of Fusion (J g ⁻¹)
0	-2.28 ± 0.07	6.25 ± 0.43	33.79 ± 1.32	67.51 ± 1.22	2.77 ± 1.03
24	-2.59 ± 0.73	5.40 ± 0.70	33.65 ± 1.94	69.75 ± 1.20	2.17 ± 1.81
48	-2.88 ± 0.53	6.64 ± 0.45	34.90 ± 1.53	68.00 ± 1.45	2.48 ± 0.47
72	-3.75 ± 0.09	6.55 ± 0.38	35.72 ± 0.89	69.53 ± 2.33	1.56 ± 1.03
120	-2.40 ± 0.34	6.43 ± 0.25	34.39 ± 1.46	70.50 ± 2.18	1.45 ± 0.35
168	-3.68 ± 0.11	6.78 ± 0.25	35.09 ± 1.14	70.42 ± 1.05	2.79 ± 0.50
240	-2.67 ± 0.20	6.26 ± 0.19	31.68 ± 0.56	69.73 ± 0.99	1.59 ± 0.33
336	-3.49 ± 0.87	5.85 ± 0.37	35.79 ± 1.39	69.03 ± 1.79	1.36 ± 1.15
504	-3.65 ± 0.43	5.95 ± 0.52	34.02 ± 1.05	68.54 ± 0.81	2.23 ± 0.75

Table 11: Glass Transition and Crystalline Melting Data for HTD7 annealed at 22 °C through three weeks.

22°C Isothermal (Hours)	T _g (°C)	T _g Breadth (°C)	Endotherm 1 (°C)	Endotherm 2 (°C)	Enthalpy of Fusion (J g ⁻¹)
24	-4.00 ± 0.24	6.04 ± 0.41	39.37 ± 0.15	65.75 ± 0.85	11.92 ± 1.21
48	-3.01 ± 0.39	7.24 ± 1.26	39.87 ± 0.18	63.85 ± 1.04	15.26 ± 1.51
72	0.24 ± 0.31	9.48 ± 0.29	41.22 ± 0.15	65.00 ± 0.88	21.30 ± 0.13
120	-0.26 ± 0.44	10.12 ± 1.04	41.53 ± 0.38	63.92 ± 1.58	20.90 ± 1.28
168	0.683 ± 0.34	9.50 ± 0.88	41.78 ± 0.32	61.98 ± 1.35	19.94 ± 1.28
240	0.24 ± 0.49	8.82 ± 0.48	42.35 ± 0.33	62.40 ± 0.71	20.76 ± 0.40
336	1.45 ± 0.67	10.67 ± 0.44	43.55 ± 0.82	63.56 ± 1.56	21.15 ± 1.17
504	0.99 ± 0.18	10.03 ± 0.31	43.55 ± 0.25	63.56 ± 0.71	21.16 ± 2.09

Table 12: Glass Transition and Crystalline Melting Data for HTD7 annealed at 30 °C through three weeks.

30°C Isothermal (Hours)	T _g (°C)	T _g Breadth (°C)	Endotherm 1 (°C)	Endotherm 2 (°C)	Enthalpy of Fusion (J g ⁻¹)
24	-0.87 ± .38	4.90 ± 0.15	47.96 ± 0.14	63.91 ± 0.51	11.44 ± 2.01
48	0.14 ± 0.37	5.08 ± 0.64	47.90 ± 0.66	63.52 ± 0.89	16.76 ± 0.94
72	1.01 ± 0.75	4.81 ± 1.06	49.24 ± 0.02	62.88 ± 0.21	18.58 ± 0.7
120	1.61 ± 0.32	6.53 ± 1.06	50.27 ± 0.44	62.57 ± 1.41	19.23 ± 1.56
168	1.58 ± 0.29	6.22 ± 0.77	51.12 ± 0.27	62.35 ± 0.11	20.06 ± 0.46
240	1.60 ± 0.27	6.41 ± 0.21	50.73 ± 0.39	63.09 ± 0.21	20.02 ± 0.44
336	0.93 ± 0.41	7.90 ± 0.27	51.01 ± 0.20	63.30 ± 0.82	20.79 ± 0.86
504	1.93 ± 0.57	8.33 ± 0.60	52.74 ± 0.16	64.08 ± 0.63	19.98 ± 0.79

Table 13: Glass Transition and Crystalline Melting Data for HTD7 annealed at 40 °C through three weeks.

40°C Isothermal (Hours)	T _g (°C)	T _g Breadth (°C)	Endotherm 1 (°C)	Endotherm 2 (°C)	Enthalpy of Fusion (J g ⁻¹)
24	-0.41 ± 0.10	4.54 ± 0.28	55.22 ± 0.45	66.81 ± 0.70	8.89 ± 1.48
48	0.14 ± 0.24	4.96 ± 0.55	56.17 ± 0.63	66.83 ± 1.23	10.23 ± 4.81
72	0.38 ± 0.48	5.31 ± 0.82	57.05 ± 1.06	66.42 ± 0.97	15.73 ± 2.40
120	0.81 ± 0.30	5.21 ± 0.36	59.23 ± 0.52	66.04 ± 1.39	16.41 ± 2.29
168	1.36 ± 0.55	6.60 ± 0.43	60.71 ± 0.45	69.30 ± 0.44	19.69 ± 2.38
240	1.21 ± 0.32	9.04 ± 1.20	59.14 ± 0.09	68.43 ± 0.61	21.69 ± 0.77
336	2.10 ± 0.65	8.91 ± 0.23	60.86 ± 0.73	68.90 ± 0.79	20.29 ± 0.58
504	0.77 ± 0.03	8.73 ± 0.57	61.05 ± 0.03	69.00 ± 0.21	22.16 ± 0.17

Table 14: Glass Transition and Crystalline Melting Data for HTD7 annealed at 50 °C through three weeks.

50°C Isothermal (Hours)	T _g (°C)	T _g Breadth (°C)	Endotherm 1 (°C)	Endotherm 2 (°C)	Enthalpy of Fusion (J g ⁻¹)
24	-0.47 ± 0.13	4.56 ± 0.43	62.39 ± 0.36	69.01 ± 1.39	11.38 ± 4.14
48	-0.38 ± 0.10	4.37 ± 0.35	63.10 ± 0.09	69.92 ± 0.26	12.16 ± 0.05
72	0.73 ± 0.12	5.75 ± 0.62	65.15 ± 0.13	70.32 ± 0.48	17.44 ± 1.21
120	0.76 ± 0.09	4.40 ± 0.05	67.21 ± 1.49	72.31 ± 0.21	17.29 ± 0.12
168	0.52 ± 0.20	5.18 ± 0.44	68.09 ± 0.72	73.36 ± 0.73	19.25 ± 1.29
240	0.22 ± 0.09	7.49 ± 0.47	66.30 ± 1.46	71.98 ± 0.05	20.66 ± 0.82
336	1.06 ± 0.25	7.80 ± 0.26	66.87 ± 0.66	73.36 ± 0.18	20.54 ± 0.25
504	0.64 ± 0.13	7.52 ± 0.42	64.91 ± 1.07	72.03 ± 0.34	21.34 ± 0.82

Table 15: Glass Transition and Crystalline Melting Data for HTD7 annealed at 60 °C through three weeks.

60°C Isothermal (Hours)	T _g (°C)	T _g Breadth (°C)	Endotherm 1 (°C)	Endotherm 2 (°C)	Enthalpy of Fusion (J g ⁻¹)
24	-0.44 ± 0.36	4.56 ± 0.41	73.07 ± 0.29	80.72 ± 0.21	11.25 ± 2.63
48	-0.69 ± 0.11	4.49 ± 0.07	72.04 ± 0.67	79.44 ± 0.59	11.47 ± 1.81
72	-0.39 ± 0.20	4.44 ± 0.18	72.98 ± 0.71	79.58 ± 0.35	9.14 ± 2.83
120	0.04 ± 0.45	4.76 ± 0.52	71.97 ± 0.30	77.97 ± 0.48	12.13 ± 3.11
168	-0.18 ± 0.48	4.40 ± 0.56	72.09 ± 0.61	78.27 ± 0.26	15.38 ± 2.39
240	-0.62 ± 0.21	4.70 ± 0.26	74.64 ± 3.75	79.79 ± 0.41	10.93 ± 3.40
336	0.29 ± 0.53	5.87 ± 0.07	76.55 ± 3.82	80.60 ± 0.63	13.96 ± 2.66
504	0.79 ± 0.36	6.34 ± 0.36	73.33 ± 0.44	78.70 ± 0.50	18.54 ± 0.74

Table 16: Room Temperature Tensile Data for HTD7 annealed at -20 °C through three weeks.

-20°C Isothermal (Hours)	Yield Stress (MPa)	Yield Strain (mm mm ⁻¹)	Failure Stress (MPa)	Failure Strain (mm mm ⁻¹)	Ultimate Stress (MPa)	Ultimate Strain (mm mm ⁻¹)	Toughness (MJ m ⁻³)
0	0.27 ± 0.06	0.22	11.70 ± 3.76	4.78 ± 0.32	11.73 ± 3.76	4.77 ± 0.32	9.60 ± 3.28
24	0.29 ± 0.02	0.22	14.94 ± 2.81	5.03 ± 0.30	14.94 ± 2.81	5.03 ± 0.30	12.74 ± 2.96
48	0.23 ± 0.03	0.22	11.54 ± 4.26	4.69 ± 0.31	11.61 ± 4.21	4.66 ± 0.30	9.73 ± 3.82
72	0.27 ± 0.08	0.22	11.87 ± 1.35	5.01 ± 0.52	12.48 ± 1.29	5.00 ± 0.52	11.26 ± 2.01
120	0.29 ± 0.07	0.22	14.84 ± 2.57	4.80 ± 0.43	14.98 ± 2.78	4.80 ± 0.44	12.13 ± 1.16
168	0.30 ± 0.10	0.22	10.67 ± 2.95	4.94 ± 0.41	10.67 ± 2.94	4.94 ± 0.40	9.57 ± 2.11
240	0.36 ± 0.08	0.22	14.98 ± 2.93	4.61 ± 0.29	15.07 ± 3.05	4.61 ± 0.30	11.79 ± 2.10
336	0.26 ± 0.05	0.22	11.92 ± 0.54	4.82 ± 0.19	12.28 ± 0.42	4.83 ± 0.21	10.19 ± 0.90
504	0.29 ± 0.03	0.22	9.03 ± 1.50	5.11 ± 0.31	9.15 ± 1.63	5.10 ± 0.30	8.24 ± 1.41

Table 17: Room Temperature Tensile Data for HTD7 annealed at 22 °C through three weeks.

22°C Isothermal (Hours)	Yield Stress (MPa)	Yield Strain (mm mm ⁻¹)	Failure Stress (MPa)	Failure Strain (mm mm ⁻¹)	Ultimate Stress (MPa)	Ultimate Strain (mm mm ⁻¹)	Toughness (MJ m ⁻³)
24	1.47 ± 0.22	0.22	13.89 ± 2.69	4.18 ± 0.27	14.10 ± 2.53	4.16 ± 0.30	17.29 ± 3.01
48	2.22 ± 0.43	0.22	18.60 ± 1.90	3.95 ± 0.13	18.60 ± 1.90	3.95 ± 0.13	23.64 ± 2.97
72	5.28 ± 0.83	0.22 ± 0.03	21.21 ± 1.26	4.23 ± 0.14	21.21 ± 1.26	4.23 ± 0.14	39.61 ± 4.94
120	5.83 ± 0.24	0.23 ± 0.03	22.14 ± 3.40	4.01 ± 0.22	22.14 ± 3.40	4.01 ± 0.22	37.91 ± 4.53
168	6.02 ± 1.11	0.22 ± 0.01	22.18 ± 1.38	3.92 ± 0.15	22.18 ± 1.38	3.92 ± 0.15	37.00 ± 4.83
240	6.10 ± 0.96	0.21 ± 0.01	24.55 ± 2.47	3.81 ± 0.39	24.55 ± 2.47	3.81 ± 0.39	39.33 ± 7.16
336	8.04 ± 1.22	0.19 ± 0.01	21.90 ± 5.07	3.44 ± 0.33	22.00 ± 4.94	3.42 ± 0.33	37.44 ± 9.26
504	7.32 ± 0.30	0.19 ± 0.03	20.53 ± 2.03	3.67 ± 0.18	20.61 ± 2.02	3.67 ± 0.17	35.22 ± 2.79

Table 18: Room Temperature Tensile Data for HTD7 annealed at 30 °C through three weeks.

30°C Isothermal (Hours)	Yield Stress (MPa)	Yield Strain (mm mm ⁻¹)	Failure Stress (MPa)	Failure Strain (mm mm ⁻¹)	Ultimate Stress (MPa)	Ultimate Strain (mm mm ⁻¹)	Toughness (MJ m ⁻³)
24	2.34 ± 0.21	0.27	17.13 ± 2.21	3.62 ± 0.14	17.13 ± 2.21	3.62 ± 0.14	20.10 ± 3.35
48	3.71 ± 0.46	0.28 ± 0.02	20.23 ± 2.12	3.61 ± 0.13	20.24 ± 2.12	3.61 ± 0.13	27.45 ± 3.59
72	5.34 ± 0.26	0.26 ± 0.04	24.52 ± 0.34	3.68 ± 0.08	24.54 ± 0.34	3.68 ± 0.08	37.53 ± 1.91
120	5.75 ± 0.06	0.28 ± 0.02	23.55 ± 0.80	3.60 ± 0.02	23.55 ± 0.80	3.60 ± 0.02	36.07 ± 0.36
168	5.85 ± 0.51	0.26 ± 0.03	22.58 ± 2.82	3.52 ± 0.11	22.58 ± 2.82	3.52 ± 0.11	34.07 ± 2.32
240	7.49 ± 0.21	0.26 ± 0.03	25.79 ± 2.02	3.91 ± 0.04	25.79 ± 2.02	3.91 ± 0.04	44.26 ± 2.51
336	7.09 ± 0.34	0.24 ± 0.01	23.33 ± 1.46	3.55 ± 0.13	23.33 ± 1.46	3.55 ± 0.13	37.78 ± 3.07
504	8.12 ± 0.33	0.25 ± 0.02	25.01 ± 5.14	3.63 ± 0.36	25.03 ± 5.10	3.62 ± 0.37	42.03 ± 8.40

Table 19: Room Temperature Tensile Data for HTD7 annealed at 40 °C through three weeks.

40°C Isothermal (Hours)	Yield Stress (MPa)	Yield Strain (mm mm ⁻¹)	Failure Stress (MPa)	Failure Strain (mm mm ⁻¹)	Ultimate Stress (MPa)	Ultimate Strain (mm mm ⁻¹)	Toughness (MJ m ⁻³)
24	3.66 ± 0.96	0.33	22.86 ± 1.21	3.88 ± 0.05	22.86 ± 1.21	3.88 ± 0.05	31.11 ± 4.60
48	4.47 ± 0.62	0.35	24.76 ± 1.72	3.76 ± 0.20	24.77 ± 1.72	3.76 ± 0.20	35.93 ± 5.90
72	5.62 ± 0.35	0.36	23.58 ± 2.55	3.65 ± 0.14	23.61 ± 2.52	3.65 ± 0.15	37.48 ± 4.51
120	6.84 ± 0.29	0.36 ± 0.05	24.07 ± 1.87	3.91 ± 0.17	24.07 ± 1.87	3.91 ± 0.17	46.04 ± 4.75
168	7.53 ± 0.16	0.31 ± 0.03	21.23 ± 1.47	3.69 ± 0.10	21.22 ± 1.48	3.69 ± 0.1	41.33 ± 2.12
240	7.82 ± 0.46	0.26 ± 0.03	20.23 ± 2.18	3.71 ± 0.31	20.23 ± 2.18	3.70 ± 0.31	41.32 ± 4.38
336	7.64 ± 0.95	0.31 ± 0.04	18.19 ± 4.24	3.58 ± 0.31	18.19 ± 4.24	3.58 ± 0.30	37.19 ± 9.17
504	9.65 ± 1.32	0.28 ± 0.02	22.24 ± 4.18	3.72 ± 0.47	22.28 ± 4.15	3.77 ± 0.43	48.73 ± 9.87

Table 20: Room Temperature Tensile Data for HTD7 annealed at 50 °C through three weeks.

50°C Isothermal (Hours)	Yield Stress (MPa)	Yield Strain (mm mm ⁻¹)	Failure Stress (MPa)	Failure Strain (mm mm ⁻¹)	Ultimate Stress (MPa)	Ultimate Strain (mm mm ⁻¹)	Toughness (MJ m ⁻³)
24	3.18 ± 0.84	0.41	18.09 ± 1.25	3.64 ± 0.15	18.09 ± 1.25	3.64 ± 0.15	24.92 ± 3.59
48	4.58 ± 0.45	0.41	18.92 ± 3.86	3.36 ± 0.20	18.93 ± 3.85	3.36 ± 0.20	27.57 ± 4.38
72	5.82 ± 0.67	0.41	22.08 ± 0.89	3.54 ± 0.07	22.08 ± 0.89	3.54 ± 0.07	33.76 ± 5.02
120	5.99 ± 0.47	0.41	23.70 ± 2.95	3.72 ± 0.19	24.72 ± 2.65	3.69 ± 0.16	42.60 ± 6.58
168	6.71 ± 0.51	0.41	22.06 ± 3.39	3.77 ± 0.18	22.06 ± 3.39	3.77 ± 0.18	42.16 ± 5.40
240	7.85 ± 0.47	0.36 ± 0.04	19.54 ± 1.89	3.72 ± 0.19	19.54 ± 1.89	3.72 ± 0.19	42.08 ± 5.30
336	7.39 ± 1.03	0.38 ± 0.06	16.26 ± 2.60	3.55 ± 0.43	16.33 ± 2.55	3.53 ± 0.46	35.52 ± 6.46
504	8.23 ± 0.87	0.32 ± 0.03	17.98 ± 2.55	3.78 ± 0.14	18.08 ± 2.62	3.76 ± 0.14	41.12 ± 5.62

Table 21: Room Temperature Tensile Data for HTD7 annealed at 60 °C through three weeks.

60°C Isothermal (Hours)	Yield Stress (MPa)	Yield Strain (mm mm⁻¹)	Failure Stress (MPa)	Failure Strain (mm mm⁻¹)	Ultimate Stress (MPa)	Ultimate Strain (mm mm⁻¹)	Toughness (MJ m⁻³)
24	1.53 ± 0.74	0.48	14.73 ± 1.80	3.98 ± 0.16	14.73 ± 1.80	3.98 ± 0.16	16.19 ± 3.31
48	1.68 ± 0.19	0.48	15.46 ± 2.59	3.89 ± 0.11	15.46 ± 2.59	3.89 ± 0.11	17.24 ± 2.66
72	1.83 ± 0.41	0.48	16.33 ± 3.89	3.75 ± 0.14	16.33 ± 3.89	3.75 ± 0.14	17.61 ± 5.18
120	2.87 ± 0.73	0.48	17.97 ± 0.72	3.57 ± 0.10	17.97 ± 0.72	3.57 ± 0.10	21.89 ± 2.28
168	4.22 ± 0.71	0.48	19.44 ± 1.66	3.59 ± 0.13	19.44 ± 1.66	3.59 ± 0.13	29.53 ± 3.49
240	5.04 ± 0.56	0.48	18.98 ± 2.54	3.51 ± 0.13	18.98 ± 2.54	3.51 ± 0.13	31.74 ± 2.84
336	4.74 ± 0.72	0.48	19.50 ± 1.63	3.31 ± 0.09	19.50 ± 1.63	3.31 ± 0.09	29.27 ± 1.77
504	6.98 ± 0.28	0.48	23.49 ± 1.49	3.43 ± 0.09	23.49 ± 1.49	3.43 ± 0.09	40.52 ± 2.34

Appendix D: Supplemental Thermal Data for HTD7 Annealed at Various Temperatures

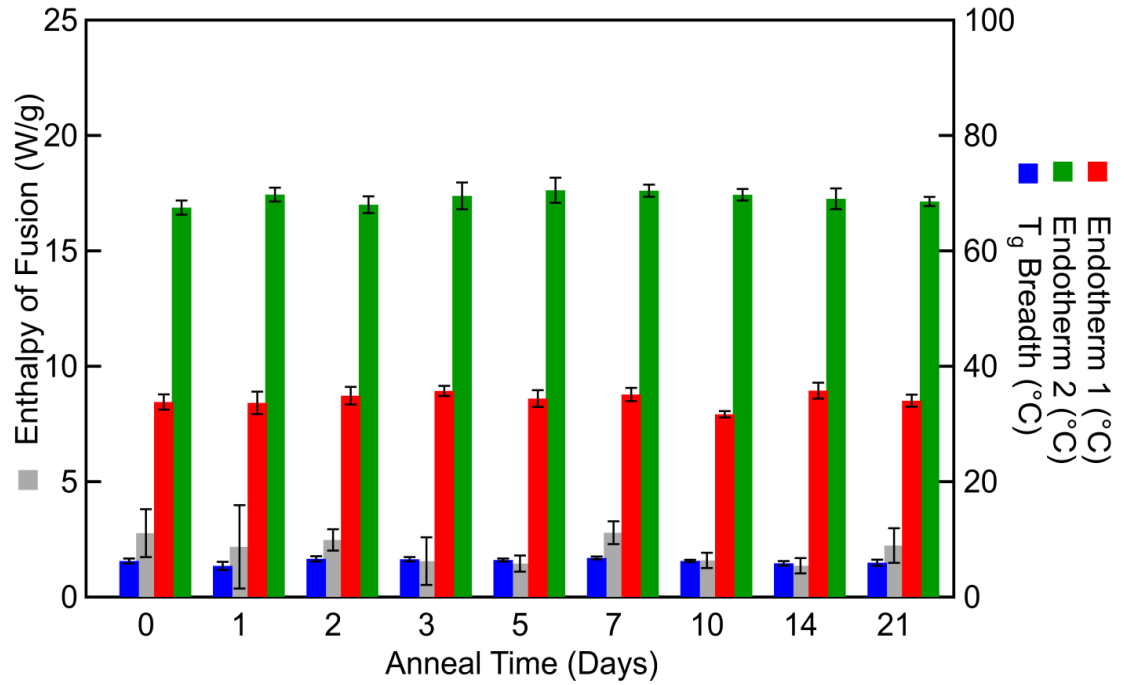


Figure 48: Thermal data over time during -20°C exposure.

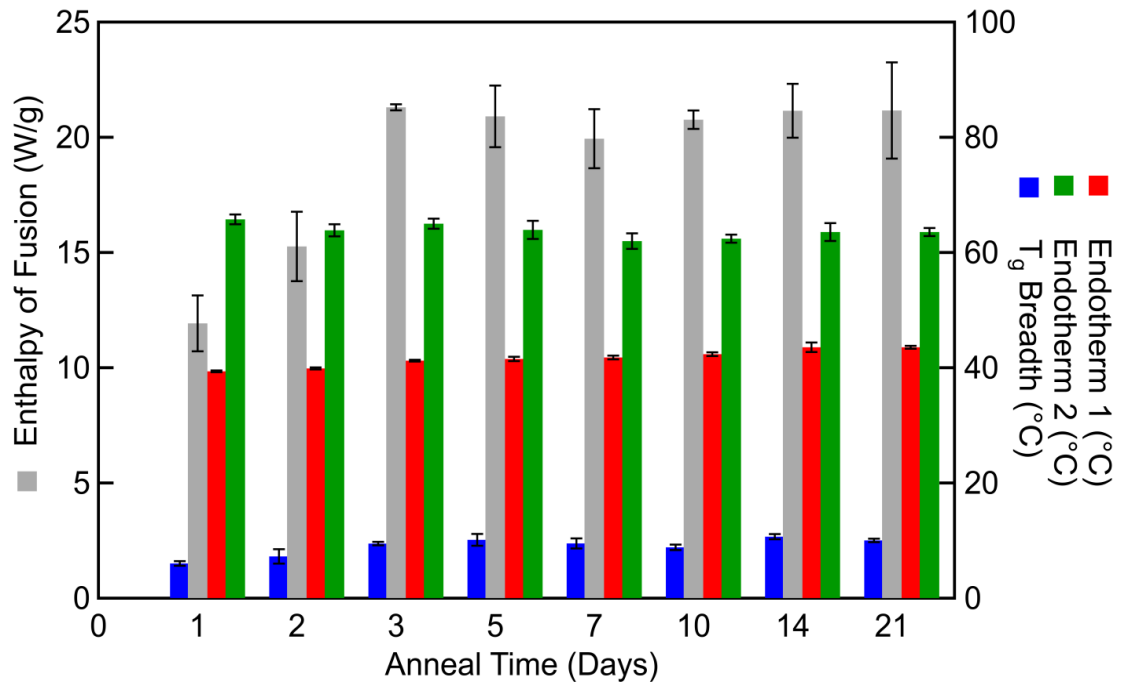


Figure 49: Thermal data over time during 22 °C anneal.

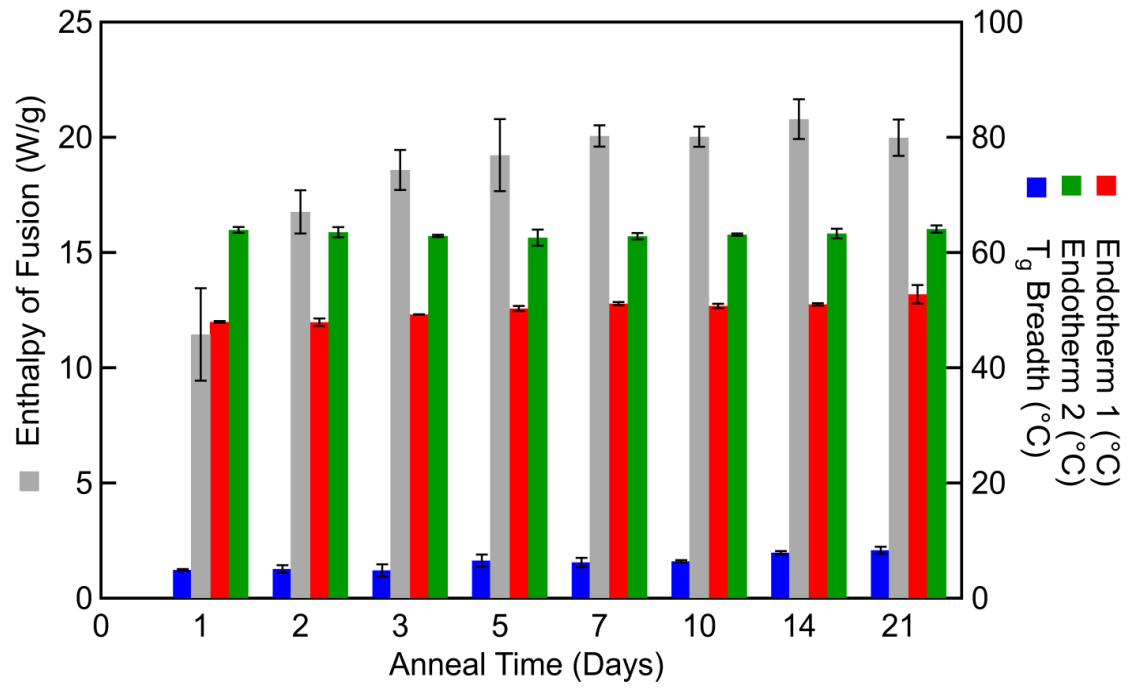


Figure 50: Thermal data over time during 30°C anneal.

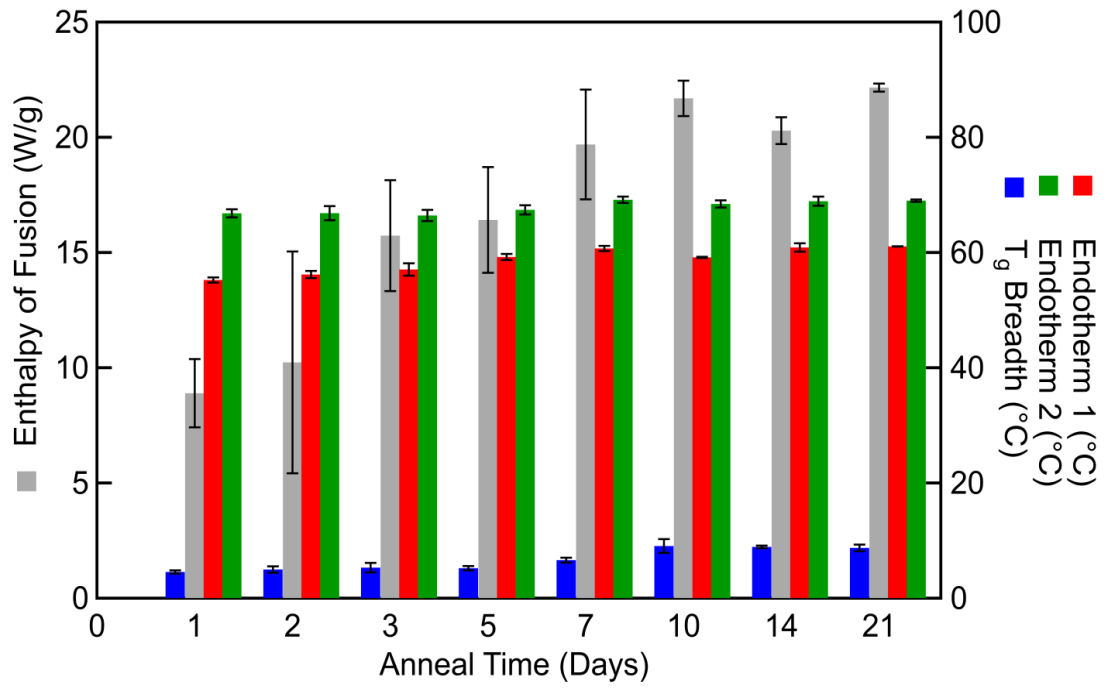


Figure 51: Thermal data over time during 40°C anneal.

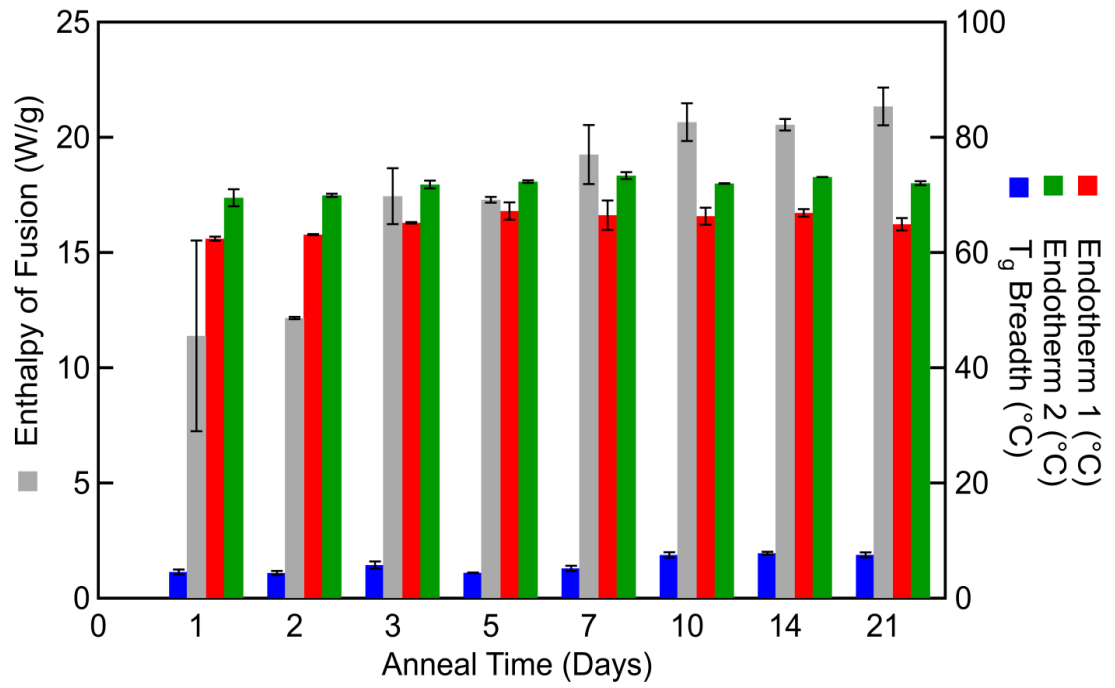


Figure 52: Thermal data over time during 50°C anneal.

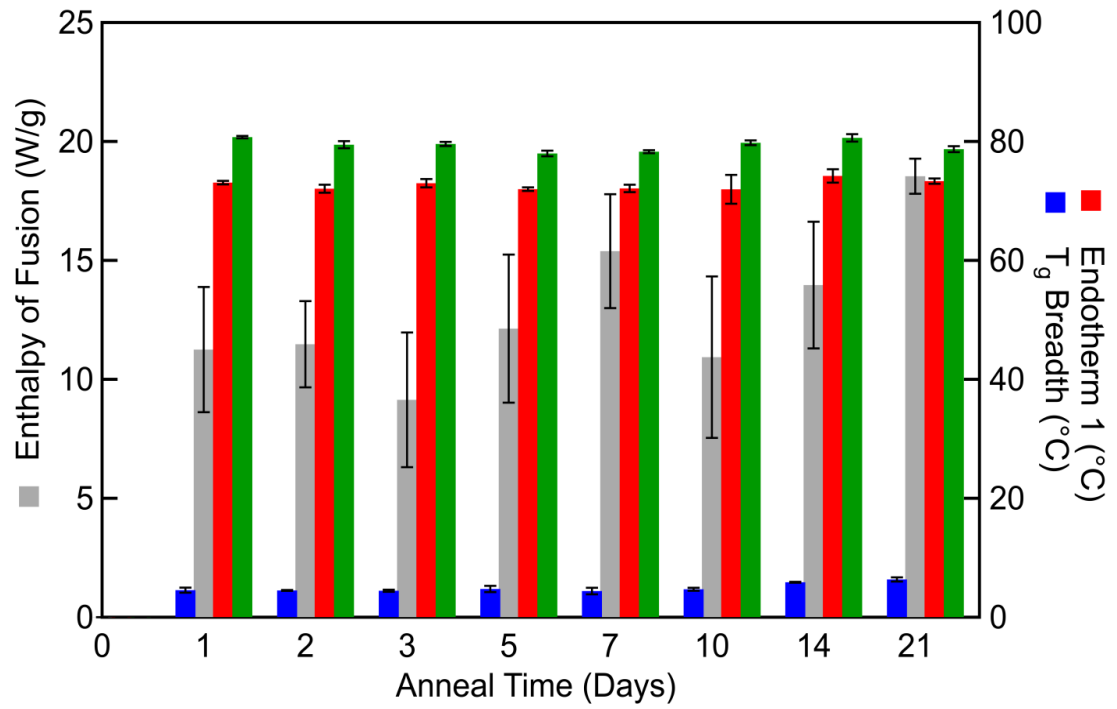


Figure 53: Thermal data over time during 60°C anneal.

References

1. Miller, A.T., et al., *Compressive cyclic ratcheting and fatigue of synthetic, soft biomedical polymers in solution*. Journal of the Mechanical Behavior of Biomedical Materials, 2016. **54**: p. 268-282.
2. Shoulders, M.D. and R.T. Raines, *COLLAGEN STRUCTURE AND STABILITY*. Annual review of biochemistry, 2009. **78**: p. 929-958.
3. Suslov, D. and J.-P. Verbelen, *Cellulose orientation determines mechanical anisotropy in onion epidermis cell walls*. Journal of Experimental Botany, 2006. **57**(10): p. 2183-2192.
4. Chen, Q.-Z., et al., *Characterisation of a soft elastomer poly(glycerol sebacate) designed to match the mechanical properties of myocardial tissue*. Biomaterials, 2008. **29**(1): p. 47-57.
5. Naficy, S., et al., *Progress Toward Robust Polymer Hydrogels*. Australian Journal of Chemistry, 2011. **64**(8): p. 1007-1025.
6. Simha, N.K., C.S. Carlson, and J.L. Lewis, *Evaluation of fracture toughness of cartilage by micropenetration*. Journal of Materials Science: Materials in Medicine, 2004. **15**(5): p. 631-639.
7. Gong, J.P., et al., *Double-Network Hydrogels with Extremely High Mechanical Strength*. Advanced Materials, 2003. **15**(14): p. 1155-1158.
8. Yu, Q.M., et al., *Direct Observation of Damage Zone around Crack Tips in Double-Network Gels*. Macromolecules, 2009. **42**(12): p. 3852-3855.
9. Gestos, A., et al., *Crosslinking neat ultrathin films and nanofibres of pH-responsive poly(acrylic acid) by UV radiation*. Soft Matter, 2010. **6**(5): p. 1045-1052.
10. Zhao, X., *Multi-scale multi-mechanism design of tough hydrogels: building dissipation*

into stretchy networks. *Soft Matter*, 2014. **10**(5): p. 672-687.

11. Lin, S., et al., *Design of stiff, tough and stretchy hydrogel composites via nanoscale hybrid crosslinking and macroscale fiber reinforcement*. *Soft Matter*, 2014. **10**(38): p. 7519-7527.
12. Naficy, S., et al., *Mechanical properties of interpenetrating polymer network hydrogels based on hybrid ionically and covalently crosslinked networks*. *Journal of Applied Polymer Science*, 2013. **130**(4): p. 2504-2513.
13. Tanaka, Y., et al., *Determination of Fracture Energy of High Strength Double Network Hydrogels*. *The Journal of Physical Chemistry B*, 2005. **109**(23): p. 11559-11562.
14. Nakajima, T., et al., *True Chemical Structure of Double Network Hydrogels*. *Macromolecules*, 2009. **42**(6): p. 2184-2189.
15. Sun, J.-Y., et al., *Highly stretchable and tough hydrogels*. *Nature*, 2012. **489**(7414): p. 133-136.
16. Bakarich, S.E., et al., *Extrusion printing of ionic-covalent entanglement hydrogels with high toughness*. *Journal of Materials Chemistry B*, 2013. **1**(38): p. 4939-4946.
17. Bajaj, P., et al., *3D Biofabrication Strategies for Tissue Engineering and Regenerative Medicine*. *Annual review of biomedical engineering*, 2014. **16**: p. 247-276.
18. Rivlin, R.S. and A.G. Thomas, *Rupture of rubber. I. Characteristic energy for tearing*. *Journal of Polymer Science*, 1953. **10**(3): p. 291-318.
19. Hong, W., Z. Liu, and Z. Suo, *Inhomogeneous swelling of a gel in equilibrium with a solvent and mechanical load*. *International Journal of Solids and Structures*, 2009. **46**(17): p. 3282-3289.
20. Zhao, X., *A theory for large deformation and damage of interpenetrating polymer networks*. *Journal of the Mechanics and Physics of Solids*, 2012. **60**(2): p. 319-332.

21. Wang, X. and W. Hong, *Delayed fracture in gels*. *Soft Matter*, 2012. **8**(31): p. 8171-8178.
22. Hong, W. and X. Wang, *A phase-field model for systems with coupled large deformation and mass transport*. *Journal of the Mechanics and Physics of Solids*, 2013. **61**(6): p. 1281-1294.
23. Kharasch, M.S., A.T. Read, and F.R. Mayo, *Correspondence*. *Journal of the Society of Chemical Industry*, 1938. **57**(32): p. 752-754.
24. Kolb, H.C., M.G. Finn, and K.B. Sharpless, *Click Chemistry: Diverse Chemical Function from a Few Good Reactions*. *Angewandte Chemie International Edition*, 2001. **40**(11): p. 2004-2021.
25. Hoyle, C.E. and C.N. Bowman, *Thiol–Ene Click Chemistry*. *Angewandte Chemie International Edition*, 2010. **49**(9): p. 1540-1573.
26. Jacobine, A.F., et al., *Photocrosslinked norbornene–thiol copolymers: Synthesis, mechanical properties, and cure studies*. *Journal of Applied Polymer Science*, 1992. **45**(3): p. 471-485.
27. Gall, K., et al., *Thermomechanics of the shape memory effect in polymers for biomedical applications*. *Journal of Biomedical Materials Research Part A*, 2005. **73A**(3): p. 339-348.
28. Nair, D.P., et al., *Photopolymerized Thiol-Ene Systems as Shape Memory Polymers*. *Polymer*, 2010. **51**(19): p. 4383-4389.
29. Smith, K.E., et al., *The effect of the glass transition temperature on the toughness of photopolymerizable (meth)acrylate networks under physiological conditions*. *Polymer*, 2009. **50**(21): p. 5112-5123.
30. Simon, D., et al., *A comparison of polymer substrates for photolithographic processing of flexible bioelectronics*. *Biomedical Microdevices*, 2013. **15**(6): p. 925-939.

31. Ware, T., et al., *Fabrication of Responsive, Softening Neural Interfaces*. *Advanced Functional Materials*, 2012. **22**(16): p. 3470-3479.
32. Ware, T., et al., *Thiol-ene/acrylate substrates for softening intracortical electrodes*. *Journal of Biomedical Materials Research Part B: Applied Biomaterials*, 2014. **102**(1): p. 1-11.
33. Posner, T., *Beiträge zur Kenntniss der ungesättigten Verbindungen. II. Ueber die Addition von Mercaptanen an ungesättigte Kohlenwasserstoffe*. *Berichte der deutschen chemischen Gesellschaft*, 1905. **38**(1): p. 646-657.
34. Hoyle, C.E., T.Y. Lee, and T. Roper, *Thiol-enes: Chemistry of the past with promise for the future*. *Journal of Polymer Science Part A: Polymer Chemistry*, 2004. **42**(21): p. 5301-5338.
35. Lowe, A.B., *Thiol-ene "click" reactions and recent applications in polymer and materials synthesis*. *Polymer Chemistry*, 2010. **1**(1): p. 17-36.
36. Read, J., *CCXIX.-The condensation of pentaerythritol with aldehydes*. *Journal of the Chemical Society, Transactions*, 1912. **101**(0): p. 2090-2094.
37. Treuting, R.G., *AN ACHROMATIC DOUBLET OF SILICON AND GERMANIUM*. *Journal of the Optical Society of America*, 1951. **41**(7): p. 454-456.
38. L, K.E. and T.W. M, *Method of preparing condensation products of pentaerythritol and glyoxal*. 1953, Google Patents.
39. B, C.D., *Linear polycyclospiroacetals and method for preparing them*. 1959, Google Patents.
40. Kim, K.-S., et al., *Synthesis and properties of aromatic polyamides and polyesters containing spiroacetal and silphenylene units*. *Polymer Bulletin*, 1995. **35**(1): p. 57-63.
41. Lingier, S., et al., *Renewable thermoplastic polyurethanes containing rigid spiroacetal*

- moieties*. European Polymer Journal, 2015. **70**: p. 232-239.
42. Zalar, F.V., *A New Spiroacetal Polymer*. Macromolecules, 1972. **5**(5): p. 539-541.
 43. Nita, L.E., et al., *Patterning poly(maleic anhydride-co-3,9-divinyl-2,4,8,10-tetraoxaspiro (5.5) undecane) copolymer bioconjugates for controlled release of drugs*. International journal of pharmaceutics, 2015. **493**(1-2): p. 328-340.
 44. Nita, L.E., et al., *Evaluation of the controlled release ability from the poly(2-hydroxyethyl methacrylate-co-3,9-divinyl-2,4,8,10-tetraoxaspiro[5.5]-undecane) polymer network synthesized in the presence of β -cyclodextrin*. Journal of Materials Science: Materials in Medicine, 2012. **23**(5): p. 1211-1223.
 45. Chiriac, A.P., M.T. Nistor, and L.E. Nita, *An Investigation on Multi-Layered Hydrogels Based on Poly(N, N-Dimethylacrylamide-co-3,9-Divinyl-2,4,8,10-tetraoxaspiro (5.5) undecane)*. Revue Roumaine de Chimie, 2014. **59**(11-12).
 46. Chiriac, A.P., et al., *Upon synthesis of a polymeric matrix with pH and temperature responsiveness and antioxidant bioactivity based on poly(maleic anhydride-co-3,9-divinyl-2,4,8,10-tetraoxaspiro [5.5] undecane) derivatives*. Materials Science and Engineering: C, 2015. **50**: p. 348-357.
 47. Sun, T.L., et al., *Physical hydrogels composed of polyampholytes demonstrate high toughness and viscoelasticity*. Nat Mater, 2013. **12**(10): p. 932-937.
 48. Yin, H., et al., *Double network hydrogels from polyelectrolytes: high mechanical strength and excellent anti-biofouling properties*. Journal of Materials Chemistry B, 2013. **1**(30): p. 3685-3693.
 49. Haque, M.A., T. Kurokawa, and J.P. Gong, *Super tough double network hydrogels and their application as biomaterials*. Polymer, 2012. **53**(9): p. 1805-1822.
 50. Taylor, D., et al., *The fracture toughness of soft tissues*. Journal of the Mechanical Behavior of Biomedical Materials, 2012. **6**: p. 139-147.

51. Diekman, B.O., et al., *Cartilage tissue engineering using differentiated and purified induced pluripotent stem cells*. Proceedings of the National Academy of Sciences, 2012. **109**(47): p. 19172-19177.
52. Hassan, C.M. and N.A. Peppas, *Structure and Morphology of Freeze/Thawed PVA Hydrogels*. Macromolecules, 2000. **33**(7): p. 2472-2479.
53. Liao, I.C., et al., *Composite Three-Dimensional Woven Scaffolds with Interpenetrating Network Hydrogels to Create Functional Synthetic Articular Cartilage*. Advanced Functional Materials, 2013. **23**(47): p. 5833-5839.
54. Yang, J., et al., *Simple approach to reinforce hydrogels with cellulose nanocrystals*. Nanoscale, 2014. **6**(11): p. 5934-5943.
55. Yang, J., et al., *Cellulose Nanocrystals Mechanical Reinforcement in Composite Hydrogels with Multiple Cross-Links: Correlations between Dissipation Properties and Deformation Mechanisms*. Macromolecules, 2014. **47**(12): p. 4077-4086.
56. Li, J., Z. Suo, and J.J. Vlassak, *Stiff, strong, and tough hydrogels with good chemical stability*. Journal of Materials Chemistry B, 2014. **2**(39): p. 6708-6713.
57. Lin, S., Y. Zhou, and X. Zhao, *Designing extremely resilient and tough hydrogels via delayed dissipation*. Extreme Mechanics Letters, 2014. **1**: p. 70-75.
58. Fedorovich, N.E., et al., *Hydrogels as Extracellular Matrices for Skeletal Tissue Engineering: State-of-the-Art and Novel Application in Organ Printing*. Tissue Engineering, 2007. **13**(8).
59. Kolesky, D.B., et al., *3D Bioprinting of Vascularized, Heterogeneous Cell-Laden Tissue Constructs*. Advanced Materials, 2014. **26**(19): p. 3124-3130.
60. Miller, J.S., et al., *Rapid casting of patterned vascular networks for perfusable engineered three-dimensional tissues*. Nat Mater, 2012. **11**(9): p. 768-774.

61. Barry, R.A., et al., *Direct-Write Assembly of 3D Hydrogel Scaffolds for Guided Cell Growth*. *Advanced Materials*, 2009. **21**(23): p. 2407-2410.
62. Hansen, C.J., et al., *High-Throughput Printing via Microvascular Multinozzle Arrays*. *Advanced Materials*, 2013. **25**(1): p. 96-102.
63. Duan, B., et al., *3D Bioprinting of heterogeneous aortic valve conduits with alginate/gelatin hydrogels*. *Journal of Biomedical Materials Research Part A*, 2013. **101A**(5): p. 1255-1264.
64. Hockaday, L.A., et al., *Rapid 3D printing of anatomically accurate and mechanically heterogeneous aortic valve hydrogel scaffolds*. *Biofabrication*, 2012. **4**(3): p. 035005-035005.
65. Bruck, H.A., et al., *Digital image correlation using Newton-Raphson method of partial differential correction*. *Experimental Mechanics*, 1989. **29**(3): p. 261-267.
66. Fan, C., et al., *A tough double network hydrogel for cartilage tissue engineering*. *Journal of Materials Chemistry B*, 2013. **1**(34): p. 4251-4258.
67. Rouillard, A.D., et al., *Methods for Photocrosslinking Alginate Hydrogel Scaffolds with High Cell Viability*. *Tissue Engineering Part C: Methods*, 2010. **17**(2): p. 173-179.
68. Khalil, S., J. Nam, and W. Sun, *Multi-nozzle deposition for construction of 3D biopolymer tissue scaffolds*. *Rapid Prototyping Journal*, 2005. **11**(1): p. 9-17.
69. Chang, R., J. Nam, and W. Sun, *Effects of Dispensing Pressure and Nozzle Diameter on Cell Survival from Solid Freeform Fabrication-Based Direct Cell Writing*. *Tissue Engineering Part A*, 2008. **14**(1): p. 41-48.
70. Chang, C.-W., et al., *PEG/clay nanocomposite hydrogel: a mechanically robust tissue engineering scaffold*. *Soft Matter*, 2010. **6**(20): p. 5157-5164.
71. Thomas, P.C., B.H. Cipriano, and S.R. Raghavan, *Nanoparticle-crosslinked hydrogels*

- as a class of efficient materials for separation and ion exchange. *Soft Matter*, 2011. **7**(18): p. 8192-8197.
72. Wang, J., et al., *A Strong Bio-Inspired Layered PNIPAM–Clay Nanocomposite Hydrogel*. *Angewandte Chemie International Edition*, 2012. **51**(19): p. 4676-4680.
 73. Lee, K.Y. and D.J. Mooney, *Alginate: properties and biomedical applications*. *Progress in polymer science*, 2012. **37**(1): p. 106-126.
 74. Larsson, L. and S. Ohman, *Serum ionized calcium and corrected total calcium in borderline hyperparathyroidism*. *Clinical Chemistry*, 1978. **24**(11): p. 1962-1965.
 75. Studer, K., et al., *Overcoming oxygen inhibition in UV-curing of acrylate coatings by carbon dioxide inerting, Part I*. *Progress in Organic Coatings*, 2003. **48**(1): p. 92-100.
 76. O'Brien, A.K., N.B. Cramer, and C.N. Bowman, *Oxygen inhibition in thiol–acrylate photopolymerizations*. *Journal of Polymer Science Part A: Polymer Chemistry*, 2006. **44**(6): p. 2007-2014.
 77. Nemir, S., H.N. Hayenga, and J.L. West, *PEGDA hydrogels with patterned elasticity: Novel tools for the study of cell response to substrate rigidity*. *Biotechnology and Bioengineering*, 2010. **105**(3): p. 636-644.
 78. Peters, W.H. and W.F. Ranson, *Digital Imaging Techniques in Experimental Stress Analysis*. *Optical Engineering*, 1982. **21**.
 79. Posner, T., *Beiträge zur Kenntniss der ungesättigten Verbindungen. II. Ueber die Addition von Mercaptanen an ungesättigte Kohlenwasserstoffe*. *Eur. J. Inorg. Chem.*, 1905. **38**(1): p. 646-657.
 80. Kolb, H.C., M.G. Finn, and B. Sharpless, *Click Chemistry: Diverse Chemical Function from a Few Good Reactions*. *Angew. Chem. Int. Ed.*, 2001. **40**(11): p. 2004-2021.
 81. Hoyle, C.E. and C.N. Bowman, *Thiol-Ene Click Chemistry*. *Angew. Chem. Int. Ed.*,

2010. **49**(9): p. 1540-1573.

82. Hoyle, C.E., T.Y. Lee, and T. Roper, *Thiol-Enes: Chemistry of the Past with Promise for the Future*. J. Polym. Sci. A Polym. Chem., 2004. **42**: p. 5301-5338.
83. Safranski, D.L. and K. Gall, *Effect of chemical structure and crosslinking density on the thermo-mechanical properties and toughness of (meth)acrylate shape memory polymer networks*. Polymer, 2008. **49**(20): p. 4446-4455.
84. Boulden, J.E., et al., *Thiol-ene-methacrylate composites as dental restorative materials*. Dental Materials, 2011. **27**: p. 267-272.
85. Carioscia, J.A., et al., *Thiol-ene oligomers as dental restorative materials*. Dental Materials, 2005. **21**: p. 1137-1143.
86. Nair, D.P., et al., *Photopolymerized thiol-ene systems as shape memory polymers*. Polymer, 2010. **51**: p. 4383-4389.
87. Ware, T., et al., *Three-Dimensional Flexible Electronics Enabled by Shape Memory Polymer Substrates for Responsive Neural Interfaces*. Macromol. Mater. Eng., 2012. **297**: p. 1193-1202.
88. Ware, T.H., et al., *Programmable Liquid Crystal Elastomers Prepared by Thiol-Ene Photopolymerization*. ACS Macro Letters, 2015. **4**(9): p. 942-946.
89. Kasprzak, S.E., et al., *Photopatterning of Thiol-ene-Acrylate Copolymers*. J. Microelectromech. Syst., 2013. **22**(2): p. 339-349.
90. Hung, L.-H., R. Lin, and A.P. Lee, *Rapid microfabrication of solvent-resistant biocompatible microfluidic devices*. Lab on a Chip, 2008. **8**(6): p. 983-987.
91. Cabral, J.T., et al., *Frontal Photopolymerization for Microfluidic Applications*. Langmuir, 2004. **20**(23): p. 10020-10029.

92. Cygan, Z.T., et al., *Microfluidic Platform for the Generation of Organic-Phase Microreactors*. *Langmuir*, 2005. **21**(8): p. 3629-3634.
93. Zhang, Q., et al., *New photo-induced thiol-ene crosslinked films based on linear methacrylate copolymer polythiols*. *Journal of Polymer Science Part A: Polymer Chemistry*, 2013. **51**(13): p. 2860-2868.
94. White, T.J., et al., *Polymerization Kinetics and Monomer Functionality Effects in Thiol–Ene Polymer Dispersed Liquid Crystals*. *Macromolecules*, 2007. **40**(4): p. 1112-1120.
95. White, T.J., et al., *Holographic polymer dispersed liquid crystals (HPDLCs) containing triallyl isocyanurate monomer*. *Polymer*, 2007. **48**(20): p. 5979-5987.
96. Yang, H., et al., *Micron-Sized Main-Chain Liquid Crystalline Elastomer Actuators with Ultralarge Amplitude Contractions*. *Journal of the American Chemical Society*, 2009. **131**(41): p. 15000-15004.
97. Senyurt, A.F., et al., *Ternary Thiol–Ene/Acrylate Photopolymers: Effect of Acrylate Structure on Mechanical Properties*. *Macromolecules*, 2007. **40**(14): p. 4901-4909.
98. Li, Q., et al., *Thiourethane-based thiol-ene high T_g networks: Preparation, thermal, mechanical, and physical properties*. *Journal of Polymer Science Part A: Polymer Chemistry*, 2007. **45**(22): p. 5103-5111.
99. Kultys, A. and A. Puszka, *Transparent poly(thiourethane-urethane)s based on dithiol chain extender*. *Journal of Thermal Analysis and Calorimetry*, 2014. **117**(3): p. 1427-1439.
100. Kultys, A., M. Rogulska, and S. Pikus, *The synthesis and characterization of new thermoplastic poly(thiourethane-urethane)s*. *Journal of Polymer Science Part A: Polymer Chemistry*, 2008. **46**(5): p. 1770-1782.
101. Shin, J., et al., *Segmented Polythiourethane Elastomers through Sequential Thiol–Ene and Thiol–Isocyanate Reactions*. *Macromolecules*, 2009. **42**(9): p. 3294-3301.

102. Carioscia, J.A., et al., *Thiol–norbornene materials: Approaches to develop high Tg thiol–ene polymers*. *Journal of Polymer Science Part A: Polymer Chemistry*, 2007. **45**(23): p. 5686-5696.
103. McNair, O.D., et al., *Sequential Thiol Click Reactions: Formation of Ternary Thiourethane/Thiol-Ene Networks with Enhanced Thermal and Mechanical Properties*. *ACS Appl. Mater. Interfaces*, 2014. **6**: p. 6088-6097.
104. Shin, J., et al., *Thiol-Isocyanate-Ene Ternary Networks by Sequential and Simultaneous Thiol Click Reactions*. *Chem. Mater.*, 2010. **22**: p. 2616-2625.
105. Rogulska, M., A. Kultys, and E. Olszewska, *New thermoplastic poly(thiourethane-urethane) elastomers based on hexane-1,6-diyl diisocyanate (HDI)*. *Journal of Thermal Analysis and Calorimetry*, 2013. **114**(2): p. 903-916.
106. Donovan, B.R., J.E. Ballenas, and D.L. Patton, *Thiol–Trifluorovinyl Ether (TFVE) Photopolymerization: An On-Demand Synthetic Route to Semifluorinated Polymer Networks*. *Macromolecules*, 2016. **49**(20): p. 7667-7675.
107. Smith, L.K. and I.R. Baxendale, *Total Syntheses of natural products containing spirocarbocycles*. *Org. Biomol. Chem.*, 2015. **13**: p. 9907-9933.
108. Lingier, S., et al., *Renewable thermoplastic polyurethanes containing rigid spiroacetal moieties*. *Eur. Polym. J.*, 2015. **70**: p. 232-239.
109. Diaconu, A., et al., *Design and synthesis of a new polymer network containing pendant spiroacetal moieties*. *Des. Monomers Polym.*, 2015. **18**(8): p. 780-788.
110. Chiriac, A.P., et al., *Upon synthesis of a polymertic matrix with pH and temperature responsiveness and antioxidant bioactivity based on poly(maleic anhydride-co-3,9-divinyl-2,4,8,10-tetraoxaspiro [5.5] undecane) derivatives*. *Materials Science and Engineering C*, 2015. **50**: p. 348-357.
111. Chiriac, A.P., M.T. Nistor, and L.E. Nita, *An investigation on multi-layered hydrogels based on poly(N, N-dimethacrylamide-co-3,9-divinyl-2,4,8,10-*

- tetraoxaspiro(5.5)undecane*. Rev. Roum. Chim., 2014. **59**(11-12): p. 1059-1068.
112. Nita, L.E., et al., *Evaluation of the controlled release ability from the poly (2-hydroxyethyl methacrylate-co-3,9-divinyl-2,4,8,10-tetraoxaspiro[5.5]-undecane) polymer network synthesized in the presence of β -cyclodextrin*. J. Mater. Sci: Mater. Med., 2012. **23**: p. 1211-1223.
113. Nita, L.E., A.P. Chiriac, and M.T. Nistor, *Upon the emulsion polymerization of 2-hydroxyethyl methacrylate with 3,9-divinyl-2,4,8,10-tetraoxaspiro[5.5]-undecane*. Colloids and Surfaces A: Physicochem. Eng. Aspects, 2011. **381**: p. 111-117.
114. Zalar, F.V., *A New Spiroacetal Polymer*. Macromolecules, 1972. **5**: p. 539-541.
115. Furniss, B.S., et al., *Vogel's Textbook of Practical Organic Chemistry*. 5th ed. 1989, London: Longman.
116. Ligon-Auer, S.C., et al., *Toughening of photo-curable polymer networks: a review*. Polymer Chemistry, 2016. **7**(2): p. 257-286.
117. McNair, O.D., et al., *Highly Tunable Thiol-Ene Networks via Dual Thiol Addition*. Macromolecules, 2013. **46**(14): p. 5614-5621.
118. Cramer, N.B. and C.N. Bowman, *Kinetics of thiol-ene and thiol-acrylate photopolymerizations with real-time fourier transform infrared*. Journal of Polymer Science Part A: Polymer Chemistry, 2001. **39**(19): p. 3311-3319.
119. Eceiza, A., et al., *Thermoplastic polyurethane elastomers based on polycarbonate diols with different soft segment molecular weight and chemical structure: Mechanical and thermal properties*. Polymer Engineering & Science, 2008. **48**(2): p. 297-306.
120. Rybníkář, F., *Secondary crystallization of polymers*. Journal of Polymer Science, 1960. **44**(144): p. 517-522.
121. Shan, G.-F., et al., *Multiple melting behaviour of annealed crystalline polymers*.

- Polymer Testing, 2010. **29**(2): p. 273-280.
122. Shi, S., et al., *Realizing the simultaneously improved toughness and strength of ultrathin LLDPE parts through annealing*. Polymer, 2013. **54**(25): p. 6843-6852.
 123. Yu, X., N. Wang, and S. Lv, *Crystal and multiple melting behaviors of PCL lamellae in ultrathin films*. Journal of Crystal Growth, 2016. **438**: p. 11-18.
 124. Stark, W. and M. Jaunich, *Investigation of Ethylene/Vinyl Acetate Copolymer (EVA) by thermal analysis DSC and DMA*. Polymer Testing, 2011. **30**(2): p. 236-242.
 125. Bas, C., P. Battesti, and N.D. Al  berola, *Crystallization and melting behaviors of poly(aryletheretherketone) (PEEK) on origin of double melting peaks*. Journal of Applied Polymer Science, 1994. **53**(13): p. 1745-1757.
 126. Verma, R., H. Marand, and B. Hsiao, *Morphological Changes during Secondary Crystallization and Subsequent Melting in Poly(ether ether ketone) as Studied by Real Time Small Angle X-ray Scattering*. Macromolecules, 1996. **29**(24): p. 7767-7775.
 127. Verma, R.K., et al., *SAXS studies of lamellar level morphological changes during crystallization and melting in PEEK*. Polymer, 1996. **37**(24): p. 5357-5365.
 128. Xue, Y., Q. Zhao, and C. Luan, *The Thermodynamic Relations between the Melting Point and the Size of Crystals*. Journal of Colloid and Interface Science, 2001. **243**(2): p. 388-390.
 129. Young, R.J. and P.A. Lovell, *Introduction to Polymers*. 3rd ed. 2011, Boca Raton, FL: CRC Press.
 130. Fried, J.R., *Polymer Science & Technology*. 2nd ed. 2003, Upper Saddle River, NJ: Prentice Hall Professional Technical Reference.
 131. Hiemenz, P.C. and T.P. Lodge, *Polymer Chemistry*. 2nd ed. 2007, Boca Raton, FL: CRC Press.

132. Kong, Y. and J.N. Hay, *The measurement of the crystallinity of polymers by DSC*. *Polymer*, 2002. **43**(14): p. 3873-3878.
133. Evans, N.T., et al., *Impact of surface porosity and topography on the mechanical behavior of high strength biomedical polymers*. *Journal of the Mechanical Behavior of Biomedical Materials*, 2016. **59**: p. 459-473.
134. Barker, I.A., et al., *A microstereolithography resin based on thiol-ene chemistry: towards biocompatible 3D extracellular constructs for tissue engineering*. *Biomaterials Science*, 2014. **2**(4): p. 472-475.
135. Oesterreicher, A., et al., *Tough and degradable photopolymers derived from alkyne monomers for 3D printing of biomedical materials*. *Polymer Chemistry*, 2016. **7**(32): p. 5169-5180.
136. Leonards, H., et al. *Advantages and drawbacks of Thiol-ene based resins for 3D-printing*. 2015.
137. McNair, O.D., et al., *Impact Properties of Thiol-Ene Networks*. *ACS Applied Materials & Interfaces*, 2013. **5**(21): p. 11004-11013.
138. Esfandiari, P., et al., *Efficient stabilization of thiol-ene formulations in radical photopolymerization*. *Journal of Polymer Science Part A: Polymer Chemistry*, 2013. **51**(20): p. 4261-4266.
139. Ligon, S., et al. *Advanced Applications of Thiol-Ene Formulations*. in *2014 UV & EB Technical Conference Proceedings*. 2014. Rosemont, Illinois: RadTech 2014 International North America.
140. Edler, M., et al., *Enhancing the stability of UV-curable thiol/vinyl carbonate resins*. *Journal of Applied Polymer Science*, 2017. **134**(24).
141. Hull, C.W., *Apparatus for production of three-dimensional objects by stereolithography*, U.S.P.a.T. Office, Editor. 1986, Uvp, Inc.: United States.

142. Murphy, S.V. and A. Atala, *3D bioprinting of tissues and organs*. Nat Biotech, 2014. **32**(8): p. 773-785.
143. Zhu, W., et al., *3D printing of functional biomaterials for tissue engineering*. Current Opinion in Biotechnology, 2016. **40**: p. 103-112.
144. Hong, S., et al., *3D Printing of Highly Stretchable and Tough Hydrogels into Complex, Cellularized Structures*. Advanced Materials, 2015. **27**(27): p. 4035-4040.
145. Berman, B., *3-D printing: The new industrial revolution*. Business Horizons, 2012. **55**(2): p. 155-162.
146. Starosolski, Z.A., et al., *Application of 3-D printing (rapid prototyping) for creating physical models of pediatric orthopedic disorders*. Pediatric Radiology, 2014. **44**(2): p. 216-221.
147. Dawood, A., et al., *3D printing in dentistry*. Br Dent J, 2015. **219**(11): p. 521-529.
148. Ventola, C.L., *Medical Applications for 3D Printing: Current and Projected Uses*. Pharmacy and Therapeutics, 2014. **39**(10): p. 704-711.
149. Rengier, F., et al., *3D printing based on imaging data: review of medical applications*. International Journal of Computer Assisted Radiology and Surgery, 2010. **5**(4): p. 335-341.
150. Petrick, I.J. and T.W. Simpson, *3D Printing Disrupts Manufacturing: How Economies of One Create New Rules of Competition*. Research-Technology Management, 2013. **56**(6): p. 12-16.
151. Leigh, S.J., et al., *A Simple, Low-Cost Conductive Composite Material for 3D Printing of Electronic Sensors*. PLOS ONE, 2012. **7**(11): p. e49365.
152. Macdonald, E., et al., *3D Printing for the Rapid Prototyping of Structural Electronics*. IEEE Access, 2014. **2**: p. 234-242.

153. Tumbleston, J.R., et al., *Continuous liquid interface production of 3D objects*. *Science*, 2015. **347**(6228): p. 1349-1352.
154. Miller, A.T., et al., *Fatigue of injection molded and 3D printed polycarbonate urethane in solution*. *Polymer*, 2017. **108**: p. 121-134.
155. Lee, H.S. and S.L. Hsu, *An analysis of phase separation kinetics of model polyurethanes*. *Macromolecules*, 1989. **22**(3): p. 1100-1105.
156. Li, Q.-T., et al., *Photothermal Conversion Triggered Precisely Targeted Healing of Epoxy Resin Based on Thermoreversible Diels–Alder Network and Amino-Functionalized Carbon Nanotubes*. *ACS Applied Materials & Interfaces*, 2017. **9**(24): p. 20797-20807.
157. Karger-Kocsis, J., *Self-healing properties of epoxy resins with poly(ϵ -caprolactone) healing agent*. *Polymer Bulletin*, 2016. **73**(11): p. 3081-3093.
158. Szebényi, G., et al., *3D Printing-Assisted Interphase Engineering of Polymer Composites: Concept and Feasibility*. *Express Polymer Letters*, 2017. **11**(7): p. 6.
159. Lewis, C.L., Y. Meng, and M. Anthamatten, *Well-Defined Shape-Memory Networks with High Elastic Energy Capacity*. *Macromolecules*, 2015. **48**(14): p. 4918-4926.
160. Sycks, D.G., et al., *Tough Semicrystalline Thiol–Ene Photopolymers Incorporating Spiroacetal Alkenes*. *Macromolecules*, 2017. **50**(11): p. 4281-4291.
161. Zelikin, A.N. and D. Putnam, *Poly(carbonate–acetal)s from the Dimer Form of Dihydroxyacetone*. *Macromolecules*, 2005. **38**(13): p. 5532-5537.
162. Akbulut, G., H.B. Sonmez, and F. Wudl, *Synthesis, characterization and properties of novel polyspiroacetals*. *Journal of Polymer Research*, 2013. **20**(3): p. 97.
163. Cohen, S.M. and E. Lavin, *Polyspiroacetal resins. Part I. Initial preparation and characterization*. *Journal of Applied Polymer Science*, 1962. **6**(23): p. 503-507.

164. Cohen, S.M., et al., *Polyspiroacetal resins. Part II. Structure and properties of polyspiroacetals from pentaerythritol-glutaraldehyde and from (pentaerythritol–dipentaerythritol)-glutaraldehyde*. Journal of Applied Polymer Science, 1962. **6**(23): p. 508-517.
165. Xu, Q., et al., *In Vitro and In Vivo Anticancer Activity of (+)-Spongistatin 1*. Anticancer research, 2011. **31**(9): p. 2773-2779.
166. Pettit, G.R., et al., *Isolation and Structure of Spongistatin 1*. J. Org. Chem., 1993. **58**: p. 3.
167. Pitt, B., et al., *The Effect of Spironolactone on Morbidity and Mortality in Patients with Severe Heart Failure*. New England Journal of Medicine, 1999. **341**(10): p. 709-717.
168. Develoux, M., *Griséofulvine*. Ann Dermatol Venereol, 2001. **128**(12): p. 9.
169. Kobayashi, M., et al., *Altohyrtin A, a Potent Anti-Tumor Macrolide from the Okinawan Marine Sponge Hyrtios altum*. Tetrahedron Letters, 1993. **34**(17): p. 4.
170. Zheng, Y., C.M. Tice, and S.B. Singh, *The use of spirocyclic scaffolds in drug discovery*. Bioorganic & Medicinal Chemistry Letters, 2014. **24**(16): p. 3673-3682.
171. Klemm, E., et al., *Free-Radical stabilizers for the thiol/ene-systems*. Die Angewandte Makromolekulare Chemie, 1993. **212**(1): p. 121-127.
172. Kühne, G., J.S. Diesen, and E. Klemm, *New results of the self-initiation mechanism of SH/En addition polymerization*. Die Angewandte Makromolekulare Chemie, 1996. **242**(1): p. 139-145.
173. Fife, T.H. and L.K. Jao, *Substituent Effects in Acetal Hydrolysis*. The Journal of Organic Chemistry, 1965. **30**(5): p. 1492-1495.
174. Gillies, E.R., A.P. Goodwin, and J.M.J. Fréchet, *Acetals as pH-Sensitive Linkages for Drug Delivery*. Bioconjugate Chemistry, 2004. **15**(6): p. 1254-1263.

175. Melchels, F.P.W., J. Feijen, and D.W. Grijpma, *A review on stereolithography and its applications in biomedical engineering*. *Biomaterials*, 2010. **31**(24): p. 6121-6130.
176. Cramer, N.B., et al., *Thiol–Ene Photopolymerization Mechanism and Rate Limiting Step Changes for Various Vinyl Functional Group Chemistries*. *Macromolecules*, 2003. **36**(21): p. 7964-7969.
177. Odian, G., *Principles of Polymerization, Fourth Edition*. 2004, Hoboken, New Jersey: John Wiley and Sons, Inc.
178. Lovestead, T.M., K.A. Berchtold, and C.N. Bowman, *Modeling the Effects of Chain Length on the Termination Kinetics in Multivinyl Photopolymerizations*. *Macromol. Theory Simul.*, 2002. **11**(7): p. 10.
179. Dworak, C., et al., *Photoinitiating monomers based on di- and triacryloylated hydroxylamine derivatives*. *Journal of Polymer Science Part A: Polymer Chemistry*, 2009. **47**(2): p. 392-403.
180. Cramer, N.B., J.P. Scott, and C.N. Bowman, *Photopolymerizations of Thiol–Ene Polymers without Photoinitiators*. *Macromolecules*, 2002. **35**(14): p. 5361-5365.
181. Lee, T.Y., et al., *The kinetics of vinyl acrylate photopolymerization*. *Polymer*, 2003. **44**(10): p. 2859-2865.
182. Cebe, P. and S. Chung, *Melting behavior of high performance composite matrix polymers: Poly(phenylene sulfide)*. *Polymer Composites*, 1990. **11**(5): p. 265-273.
183. Bell, J.P. and J.H. Dumbleton, *Relation between melting behavior and physical structure in polymers*. *Journal of Polymer Science Part A-2: Polymer Physics*, 1969. **7**(6): p. 1033-1057.
184. Bell, J.P. and T. Murayama, *Relations between dynamic mechanical properties and melting behavior of nylon 66 and poly(ethylene terephthalate)*. *Journal of Polymer Science Part A-2: Polymer Physics*, 1969. **7**(6): p. 1059-1073.

185. Rim, P.B. and J.P. Runt, *Melting behavior of crystalline/compatible polymer blends: poly(ϵ -caprolactone)/poly(styrene-co-acrylonitrile)*. *Macromolecules*, 1983. **16**(5): p. 762-768.
186. Qiu, G., et al., *Dual melting endotherms in the thermal analysis of poly(ethylene terephthalate)*. *Journal of Applied Polymer Science*, 1998. **69**(4): p. 729-742.
187. Rubinstein, M. and R.H. Colby, *Polymer Physics*. 2003, New York: Oxford University Press.
188. Ikehara, T. and T. Nishi, *Primary and secondary crystallization processes of poly(ϵ -caprolactone)/styrene oligomer blends investigated by pulsed NMR*. *Polymer*, 2000. **41**(21): p. 7855-7864.
189. Way, J.L., J.R. Atkinson, and J. Nutting, *The effect of spherulite size on the fracture morphology of polypropylene*. *Journal of Materials Science*, 1974. **9**(2): p. 293-299.
190. Pukánszky, B., I. Mudra, and P. Staniek, *Relation of crystalline structure and mechanical properties of nucleated polypropylene*. *Journal of Vinyl and Additive Technology*, 1997. **3**(1): p. 53-57.
191. Crist, B., C.J. Fisher, and P.R. Howard, *Mechanical properties of model polyethylenes: tensile elastic modulus and yield stress*. *Macromolecules*, 1989. **22**(4): p. 1709-1718.
192. Avrami, M., *Kinetics of Phase Change. I General Theory*. *The Journal of Chemical Physics*, 1939. **7**(12): p. 1103-1112.
193. Avrami, M., *Kinetics of Phase Change. II Transformation-Time Relations for Random Distribution of Nuclei*. *The Journal of Chemical Physics*, 1940. **8**(2): p. 212-224.
194. Avrami, M., *Granulation, Phase Change, and Microstructure Kinetics of Phase Change. III*. *The Journal of Chemical Physics*, 1941. **9**(2): p. 177-184.
195. Andjelić, S. and R.C. Scogna, *Polymer crystallization rate challenges: The art of*

chemistry and processing. Journal of Applied Polymer Science, 2015. **132**(38): p. n/a-n/a.

196. Baldenegro-Perez, L., et al., *Molecular Weight and Crystallization Temperature Effects on Poly(ethylene terephthalate) (PET) Homopolymers, an Isothermal Crystallization Analysis*. Polymers, 2014. **6**(2): p. 583.
197. Mark, J.E., *Physical Properties of Polymers*. 3rd ed. 2004, Cambridge: Cambridge University Press.
198. Spruiell, J.E. and C.J. Janke, *A Review of the Measurement and Development of Crystallinity and its Relation to Properties in Neat Poly(phenylene sulfide) and its Fiber Reinforced Composites*. 2004, Oak Ridge National Laboratory: Oak Ridge, TN.

Biography

Dalton Sycks was born on April 14th, 1991 in Edina, Minnesota to George and Susan Sycks. Before attending Duke, he received a Bachelor of Science in Mathematics and a Bachelor of Science in Materials Science and Engineering from the University of Arizona in May of 2013. He has published and (co-)authored several articles and book chapters, and has received honors and awards for his work; a list of publications and awards is presented below. Works of primary authorship are noted in bold.

Publications

1. **Printing Stretchable and Tough Hydrogels into Complex Three-Dimensional Structures with Cells.** *Advanced Materials*.
2. **Tough Semicrystalline Thiol-ene Photopolymers Incorporating Spiroacetal Alkenes.** *Macromolecules*.
3. **A Tough, Stable Spiroacetal Thiol-ene Resin for 3D Printing.** *Journal of Applied Polymer Science*. Under Review.
4. Fatigue of Injection Molded and 3D Printed Polycarbonate Urethane in Solution.
5. Shape-Memory Polymer Device Design, Chapter 3: Material Selection.

Awards

1. National Science Foundation Graduate Research Fellowship
2. Best Poster Award Finalist: MRS Spring Conference 2014